

ABSTRACT

Title of dissertation: MAGNETOHYDRODYNAMIC
 EQUILIBRIUM AND STABILITY OF
 CENTRIFUGALLY CONFINED PLASMAS

Yi-Min Huang, Doctor of Philosophy, 2004

Dissertation directed by: Professor Adil B. Hassam
 Department of Physics

Centrifugal confinement is an alternative approach to magnetic fusion, employing a magnetic field with an open field line configuration. In this scheme, a plasma with magnetic mirror geometry is made to rotate azimuthally at supersonic speeds. The resulting centrifugal forces, given the field line curvature, prevent the plasma from escaping along the field lines. This dissertation addresses the equilibrium and stability of this configuration within the framework of magnetohydrodynamics (MHD). Well confined equilibrium with desirable profiles is demonstrated by numerical simulation. As far as stability is concerned, four types of magnetohydrodynamic modes determine the overall stability of centrifugally confined plasmas: flute interchanges and the Kelvin–Helmholtz instability, in a low β system, and the magnetorotational instability (MRI) and the Parker instability, in a high β system. One of the underpinnings of the centrifugal confinement is that flute interchanges could be stabilized by the strong velocity shear accompanying the rotation. Numerical simulations show strong evidence of stabilization, provided that the shear flow is not unstable to Kelvin–Helmholtz (KH) modes. The KH modes are ideally stable if the generalized Rayleigh’s Inflexion criterion is satisfied. Particle sources are shown to be important to both equilibrium and stability. In the absence of particle sources, density profiles relax under resistive diffusion to pile up to the outboard side of the

confining vessel. Tailoring the density profiles by appropriately placing the particle sources could be used to achieve control over MHD stability, for both interchanges and KH modes. Analytic analysis of interchanges based on an extension of MHD which applicable for low density plasmas with $V_A \sim c$ is presented. The interchange growth rates are reduced by a factor of $\sqrt{1 + V_A^2/c^2}$ compared to the usual MHD prediction. The physical mechanisms of both the MRI and the Parker instability are examined and an explanation of why the MRI mechanism is insufficient to destabilize the system while the Parker instability could occur is given. Numerical simulations of the nonlinear behavior of the Parker instability are presented. It is shown that clumping from the Parker instability could reinforce centrifugal confinement.

MAGNETOHYDRODYNAMIC EQUILIBRIUM AND
STABILITY OF
CENTRIFUGALLY CONFINED PLASMAS

by

Yi-Min Huang

Dissertation submitted to the Faculty of the Graduate School of the
University of Maryland, College Park in partial fulfillment
of the requirements for the degree of
Doctor of Philosophy
2004

Advisory Committee:

Professor Adil B. Hassam, Chair/Advisor
Professor James Drake
Dr. Parvez N. Guzdar
Professor Richard Ellis
Professor Douglas P. Hamilton

© Copyright by

Yi-Min Huang

2004

Dedication

To my parents,

Chao-Hong Huang

and

Fu-Mei Chen

TABLE OF CONTENTS

List of Figures	vii
List of Tables	xiii
1 Overview	1
1.1 Introduction	1
1.2 Outline of the Dissertation	5
1.3 Flute Interchanges and the Kelvin–Helmholtz Instability	6
1.4 Magnetorotational and Parker Instability	10
2 Velocity Shear Stabilization of Centrifugally Confined Plasma	16
2.1 Introduction	16
2.2 Numerical Model	18
2.3 Conclusion	25
3 Resistive Magnetohydrodynamic Equilibrium and Stability of a Rotating Plasma with Particle Sources	29
3.1 Introduction and Motivation	29
3.2 Slowly Diffusing Steady State of Rotating Plasma	31

3.3	Numerical Model	35
3.4	Velocity Shear Stabilization	37
3.4.1	Cases with No Velocity Shear	38
3.4.2	Cases with Velocity Shear	40
3.4.3	The “Weakest” Point	46
3.5	Kelvin–Helmholtz Instability	49
3.6	Other Issues	52
3.6.1	Hysteresis	52
3.6.2	Asymmetric Source	57
3.6.3	Generalized Ohm’s Law and Thermoelectric Effect	57
3.7	Summary and Conclusion	58

4 Interchanges in Low Density Plasmas — with Applications to Line-Tied Slab and Centrifugally Confined Plasma

	Plasma	60
4.1	Introduction	60
4.2	Basic Equations	61
4.3	Flute Interchanges in a Line-Tied Slab	62
4.3.1	Reduced Equations	62
4.3.2	Linear Stability	65
4.4	Centrifugally Confined Plasmas	66
4.4.1	Reduced Equations	68
4.4.2	Linearized Equations	71
4.4.3	Linear Stability – Normal Mode Analysis	73
4.4.4	Linear Stability – Initial-Value Analysis	78
4.5	Summary and Discussion	81

5 Magnetorotational and Parker Instabilities in Magne-

tized Plasma Dean Flow as Applied to Centrifugally	
Confined Plasmas	83
5.1 Introduction	83
5.2 The Dean Flow Model	85
5.3 Linear Stability Analysis	87
5.3.1 Derivation of the Eigenvalue Equation	87
5.3.2 Cold Plasma Limit, $C_S \rightarrow 0$	89
5.3.3 Incompressible Limit, $C_S \rightarrow \infty$	91
5.3.4 Stability over the Parameter Range	94
5.4 Initial-Value Simulation	96
5.5 Implications for Centrifugally Confined Plasmas	101
5.6 Summary and Discussion	104
6 Nonlinear Development of the Parker Instability	106
7 Summary and Outlook	111
A Electric Current Driven Cylindrical Hartmann Flow	114
A.1 Governing Equations	114
A.2 Numerical Solutions	118
A.3 Remark on Secondary Flow	124
B Linearization of Eqs. (4.50)–(4.53)	125
C Local Stability Criterion of Magnetorotational Instability	129
D Local Parker Instability Growth Rate	131

D.1 A Simple Derivation of the Parker Instability Growth Rate in the
Cold Plasma Limit 131

D.2 Local Parker Instability Growth Rate — the General Case 134

Bibliography **136**

LIST OF FIGURES

1.1	The idea of centrifugal confinement. From the MHD point of view, the combination of the centrifugal force \mathbf{F}_c and the magnetic force $\mathbf{J} \times \mathbf{B}$ has to be balanced by the pressure gradient. Since the $\mathbf{J} \times \mathbf{B}$ is perpendicular to the field, the net force has a nonzero parallel component from the centrifugal force. This parallel force contains the plasma along the field.	2
1.2	Flute interchanges in a simple mirror. (a) The density profile of a 2D steady state. The steady state is maintained by particle sources (at the center) and sinks (near the walls). Isothermality and an simple equation of state $p = 2nT$ are assumed. In the absence of rotations, the pressure is constant along a field line since there is no centrifugal confinement. (b) The time evolution of density at the mid-plane, after adding in an initial 3D random noise. The flute interchanges grow as a result.	3
1.3	The “two mass points connected by a spring” model of the MRI. The magnetic field threaded through the disk acts as a spring which couples different fluid elements (represented by the two mass points m_i and m_o) together. If the equilibrium angular frequency is outwardly decreasing, then the spring transports angular momentum from the inner mass point m_i to the outer one m_o , causing the MRI.	13

1.4	The mechanism of the Parker instability. (a) The $\mathbf{J} \times \mathbf{B}$ force supported the plasma against the gravity \mathbf{g} . (b) When the magnetic field is perturbed slightly, the horizontal component of the magnetic force compresses the plasma toward the center.	14
2.1	The 2D laminar profiles: (a) temperature and (b) pressure, with magnetic field lines overlaid. A cut of the temperature at midplane is shown in (c). Likewise, (d) is a pressure cut.	21
2.2	More 2D laminar profiles: (a) density and (b) angular velocity, with magnetic field lines overlaid. A cut of the density at midplane is shown in (c). Likewise, (d) is an angular velocity cut.	22
2.3	The time evolution of the pressure on the $r - \phi$ midplane of the test without velocity shear.	26
2.4	Stabilization from restoring velocity shear.	27
3.1	The time sequence of the density for the case with an aspect ratio $R=4$ in six gray-scale frames (velocity shear artificially suppressed). .	39
3.2	The time evolution of $W(t) \equiv \langle 1 - \rho/\rho_0 \rangle$ for $R = 2, 4, 6, 8,$ and 10 . $\eta = \mu = 0.002$. The velocity shear is artificially suppressed, while a “centrifugal force” is added. As the initial perturbation grew, $W(t)$ saturated to about 0.4 for all cases.	40
3.3	The time evolution of $W(t)$ for $R = 2, 4, 6, 8,$ and 10 . $\eta = \mu = 0.002$ As the initial perturbation grew, $W(t)$ saturated to different level for different R . Large aspect ratio systems appear more stable.	42

3.4	The saturated density profile (averaged over ϕ) after the onset of the interchange instability. The top left panel is the laminar density, shown for reference. The remaining five panels correspond to increasing R , with the laminar density overlaid (dashed). At $R = 2$, the density profile is heavily flattened at the middle (where the flow shear is weakest); however, at $R = 10$, the laminar profile is almost completely retained. $\eta = \mu = 0.002$ in these simulations.	43
3.5	The time evolution of the averaged radial kinetic energy. Notice the oscillatory behavior. The difference at the “starting point” is due to the small laminar $u_r(\sim \eta)$, which is different for different cases. . . .	44
3.6	The time sequence of the density for the case $R=4$. Flute interchanges occurred but were localized at the middle ($t=10,14$). The interchanges flattened the density and started to decay ($t=24$), leading to a quiescent period ($t=44$). As the particle source tried to rebuild the density profile, the system went unstable again ($t=60$). . .	45
3.7	The saturated density profile (averaged along ϕ) after the interchanges. Top: various η with fixed μ . Bottom: various μ with fixed η . The dependence on dissipation is evident. As dissipation gets smaller, velocity shear stabilization becomes less efficient. $R = 4$ in all these simulations.	47
3.8	The time evolution of the averaged radial kinetic energy. Top: various η with fixed μ . Bottom: various μ with fixed η	48
3.9	The laminar density profile of the two cases, one with a stabilizing stratification at the weakest point (solid line), the other with a destabilizing stratification (dotted line). Unstable modes developed in the latter, resulting in a flattop of the density profile (dash-dot line). The inset shows the laminar angular frequency of the flow for reference. . .	50

3.10	The time sequence for the case $C = 0.5, D = 0.5$. The characteristic Kelvin cat's eyes showed up as a result of the Kelvin–Helmholtz instability. After the system released the free energy, it settled down to a new, quiescent state.	53
3.11	The time sequence for the case $C = 0.5, D = -0.5$. Because of the destabilizing stratification at the weakest point, the interchanges set in at first ($t=10$). Later on, the Kelvin–Helmholtz type of instability started to grow ($t=30$). After the free energy released, the system settled down to a new state, with some residual wobbles at the center.	54
3.12	The time evolution of $\langle \rho u_r^2/2 \rangle$. The case $C = 0.5, D = -0.5$ has a destabilizing stratification at the weakest point. After the free energy was released, some residual wobbles remained around the weakest point. Those wobbles correspond to the oscillatory $\langle \rho u_r^2/2 \rangle$. The case $C = 0.5, D = 0.5$, on the other hand, enjoyed a long period of stable stage after releasing its free energy, until a sudden growth of unstable modes at $t \sim 170$	55
3.13	The ϕ averaged density, Rayleigh's criterion, and radial kinetic energy profile, for the case $C = 0.5, D = 0.5$, at four representative times. Notice that as the Rayleigh's criterion approached zero at $t = 175$, unstable modes started to grow. Also notice the global nature of the saturated axial flow, at $t = 250$. This global flow could cause a much more enhanced cross-field transport than localized wobbles could do.	56
4.1	A sketch of a centrifugally confined plasma.	67
5.1	A Dean flow model for the straight section of a centrifugally confined plasma. A plasma within an annular box with inner radius R , width a and elongation L is threaded by a straight magnetic field in \hat{z}	86

5.2	Normalized growth rates of the most unstable modes for the case $M_S = 4$, $R/a = 1/3$. The growth rate is normalized to the inverse of the sound time scale, C_S/a	94
5.3	Marginal stability curves for $M_S = 3, 4, 6, 8, 10$, with $R/a = 1/3$. The region above the curve is unstable.	95
5.4	Time evolution of $\langle \ln A \rangle$ for various wavenumbers of model 1a.	99
5.5	Time evolution of $\langle \ln A \rangle$ for various wavenumbers of model 1c. The growth of the mode $k_z a = 9.67$ is due to nonlinear coupling.	100
5.6	A comparison of the linear growth rate obtained by simulation and by linear analysis.	101
5.7	Marginal stability curves for $M_S = 4, 6, 8, 10$, with $R/a = 1$	103
6.1	The Parker instability in a Dean flow. The density profile is shown in gray scale, with magnetic fields overlaid. Notice that the two axes are not to scale. Also notice that different color codes are used in different time slices. Times are shown on the Alfvénic time scale.	108
6.2	The Parker instability in a highly elongated, slightly curved mirror field. Only half of the system is shown. As the rotation exceeded the critical speed, a plasma clump suddenly formed, first off-center ($t=210$), then shifted toward the center and finally settled down there ($t=300$). Times are shown in the Alfvénic time scale.	110
A.1	Sketch of an electric current driven cylindrical Hartmann flow.	115
A.2	Sketch of the "simplified" electric current driven cylindrical Hartmann flow.	116
A.3	The solution for $H_a = 1$. Panel (a) shows contours of rB_ϕ , which are also current paths. Panel (b) shows contours of u_ϕ . The contours (from the outside to the inside) correspond to 0.1, 0.2, ..., 0.9 of the peak value of u_ϕ , which is 0.11.	120

A.4 The solution for $H_a = 10$. Panel (a) shows contours of rB_ϕ , which are also current paths. Panel (b) shows contours of u_ϕ . The contours (from the outside to the inside) correspond to 0.1, 0.2, ..., 0.9 of the peak value of u_ϕ , which is 0.67. 121

A.5 The solution for $H_a = 50$. Panel (a) shows contours of rB_ϕ , which are also current paths. Panel (b) shows contours of u_ϕ . The contours (from the outside to the inside) correspond to 0.1, 0.2, ..., 0.9 of the peak value of u_ϕ , which is 1.12. 122

A.6 The solution for $H_a = 100$. Panel (a) shows contours of rB_ϕ , which are also current paths. Panel (b) shows contours of u_ϕ . The contours (from the outside to the inside) correspond to 0.1, 0.2, ..., 0.9 of the peak value of u_ϕ , which is 1.26. 123

LIST OF TABLES

5.1	A comparison between the normal mode shooting code results and the initial-value simulation results.	98
-----	--	----

Chapter 1

Overview

1.1 Introduction

The basic idea of centrifugal confinement is to use centrifugal forces from rapid plasma rotation to augment conventional magnetic confinement (see Ref. [48, 31, 23] and references therein). In Fig. 1.1 we depict the basic concept. In this scheme, a magnetic mirror type plasma is made to rotate azimuthally at supersonic speeds; thus, centrifugal forces along magnetic field lines confine the plasma to the center section. Since centrifugal confinement is essentially a competition between the inertial force and the pressure gradient, a supersonic rotation is needed for a good confinement.

One of the key issues for the success of this scheme is the magnetohydrodynamic (MHD) stability of the rapidly rotating configuration. This is a rather complicated issue because of the various ingredients involved. We discuss these in turn below. In a low β (i.e. $p/B^2 \ll 1$ and $\rho u_T^2/B^2 \ll 1$, where p is the pressure, ρ the density, u_T the toroidal speed, and B the magnetic field) system, the strong magnetic field stabilizes perturbations along the field, rendering the system two dimensional (2D). In that case:

(a) The predominant MHD instability is the flute interchange mode. It is well-known that a simple, non-rotating magnetic mirror is unstable to flute interchanges driven by the pressure gradient and the unfavorable magnetic curvature (see, for

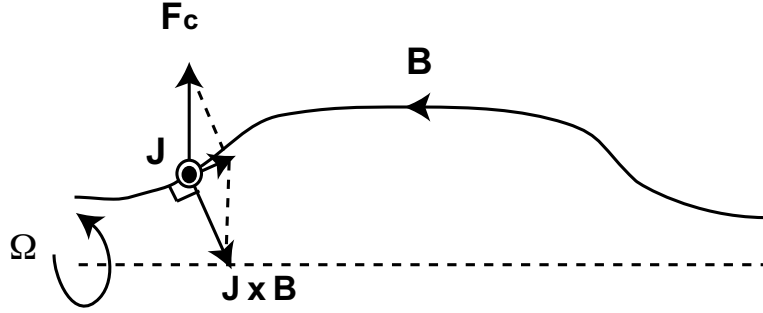


Figure 1.1: The idea of centrifugal confinement. From the MHD point of view, the combination of the centrifugal force \mathbf{F}_c and the magnetic force $\mathbf{J} \times \mathbf{B}$ has to be balanced by the pressure gradient. Since the $\mathbf{J} \times \mathbf{B}$ is perpendicular to the field, the net force has a nonzero parallel component from the centrifugal force. This parallel force contains the plasma along the field.

example, Ref. [24]; see also Fig. 1.2 for a simulation demonstrating interchanges in a simple mirror). In a centrifugally confined plasma, the situation seems worse since the centrifugal force is also a potential driving force of interchanges. However, it has become increasingly clear in recent years that the concomitant velocity shear of the rotation can suppress not only microinstability but possibly also interchange-like modes [8, 30, 62]. The stability of the system, therefore, depends on the competition between these stabilizing and destabilizing effects.

(b) The velocity shear, albeit being the stabilizing effect for interchanges, could also itself drive an instability. This is known as the Kelvin–Helmholtz (KH) instability [19, 22]. From ordinary fluid theory, the stability criterion is profile dependent. Furthermore, non-ideal effect such as viscosity could trigger the KH instability even if the profile is ideally stable.

In a high β system (which is highly desirable for an efficient fusion reactor), perturbations along the magnetic field also need to be considered. In this case, two other possible instabilities are:

(c) The magnetorotational instability (MRI) has to be considered. Although

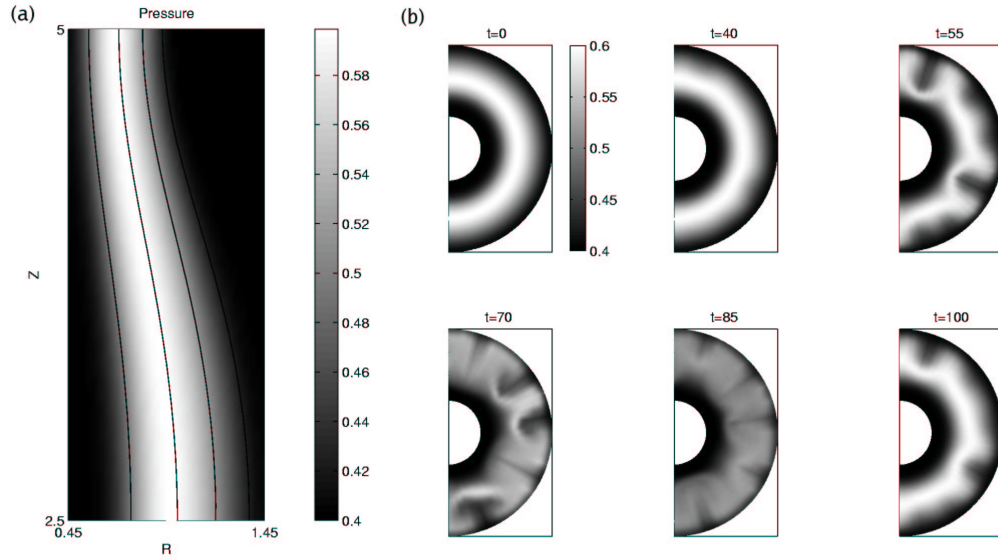


Figure 1.2: Flute interchanges in a simple mirror. (a) The density profile of a 2D steady state. The steady state is maintained by particle sources (at the center) and sinks (near the walls). Isothermality and an simple equation of state $p = 2nT$ are assumed. In the absence of rotations, the pressure is constant along a field line since there is no centrifugal confinement. (b) The time evolution of density at the mid-plane, after adding in an initial 3D random noise. The flute interchanges grow as a result.

the MRI had been discovered decades ago [65, 18], it was not until the recent rediscovery by Balbus and Hawley [2, 35] that workers recognized its role in the angular momentum transport process in accretion disks [4]. The occurrence of the MRI requires a combination of two conditions (among others), namely, a somewhat weak magnetic field and outwardly decreasing differential rotation. Since both the magnetic field and differential rotation are present in the centrifugal confinement scheme, it is interesting to see whether or not the MRI could occur. Given that the MRI has never been observed experimentally, this is of basic interest, although it might be deleterious in a fusion reactor.

(d) The Parker instability is also a concern. It was first pointed out by Parker that a magnetized plasma partially supported against gravity by the magnetic field could spontaneously break into clumps [54]. Parker suggested this as an explanation for the non-uniformity of the interstellar medium inside a galaxy. In the centrifugal confinement scheme, the centrifugal force plays the role of gravity, and the Parker instability could occur.

As discussed, the stability of the system depends on many factors, including the details of profiles and the geometrical shape of the system. However, some dimensionless parameters are found to be very useful in discussing the general characteristics. In particular, two Mach numbers, the sonic Mach number M_S , defined as the ratio of the toroidal flow speed u_T to the sound speed C_S , and the Alfvén Mach number M_A , defined as the ratio of u_T to the Alfvén speed V_A , measure the relative strength between the thermal energy, the kinetic energy, and the magnetic energy. Two geometric parameters, the aspect ratio R/a , and the elongation L/a , give a rough idea of the shape of the system, where R is the major radius, a the radial width, and L the axial length of the system¹.

Several analytic calculations and numerical simulations have been done during the past few years to assess the MHD stability of the system. Given the complexity

¹See Fig. 4.1 for a better idea of the definitions of a , R , and L .

of the full system, our general approach is therefore not to address the problem as a whole, but to separate the problem into pieces. Each piece contains some essential ingredients of the full system.

1.2 Outline of the Dissertation

To give the readers a big picture before going into the detail, the rest of this Chapter is a self-contained overview of the dissertation. This may be regarded as a “tourist’s guide” to the main part of the dissertation, Chapters 2 – 6. Sec. 1.3 is a review of flute interchanges, velocity shear stabilization, and the KH instability. Those are the topics we study extensively in Chapters 2 – 4. Relevant key results from previous work [32, 33, 21] are also summarized here to complete the picture. Sec. 1.4 reviews the MRI and the Parker instability, which are the topics of Chapters 5 and 6. Finally, the current understanding, open questions, and possible future directions are summarized and discussed in Chapter 7.

Four supplemental Appendices are added after the main text of the dissertation. Appendix A discusses a cylindrical Hartmann flow driven by externally imposed electric current. The motivation of this study is as follows. For all the simulations reported in this dissertation, the plasma flow is driven by an applied force for simplicity. Although an external force could be applied, for example, by neutral beam injection, this is not the way the Maryland Centrifugal Experiment (MCX) is implemented. In MCX, the plasma flow is created by imposing a voltage across the plasma — by connecting the inner and outer walls of the vessel to a capacitor bank. Because of the plasma viscosity, a leakage current through the plasma will be present. The leakage current, in return, drives the flow against viscous slowing down by exerting an $I \times B$ force on the plasma. A steady state can be achieved only if there exists an external current to charge up the capacitor bank against the leakage current. This way of spinning up the plasma by imposing external currents can be implemented in simulation through imposing boundary conditions on the magnetic

field, which we explain in Appendix A with the Hartmann flow example. The Hartmann flow is of considerable interest by itself. Two thin so-called Hartmann layers form at the top and the bottom of the flow because of the imposed no-slip boundary condition². Whether the Hartmann layers exist or not in a centrifugally confined plasma is not clear at the moment. Certainly that is an important issue and worth a close examination. Appendix B gives the detail of a linearization calculation in Chapter 4. Appendices C and D give local dispersion relations and stability criteria of the MRI and the Parker instability.

1.3 Flute Interchanges and the Kelvin–Helmholtz Instability

Velocity shear stabilization of interchanges is one of the main underpinnings of the centrifugal confinement scheme. This has been cross-checked in several studies. We summarize the key results as follows.

(a) As mentioned in the Introduction, there are two driving forces of the flute interchange: the centrifugal force acting on the density gradient, and the magnetic curvature effect acting on the pressure gradient. These two effects were studied analytically with a Dean flow model [32], in which a straight axial field was assumed for simplicity. The key feature that distinguishes Dean flow from Couette flow is that the former has an equilibrium flow which is no-slip at the fixed boundaries, while the latter has an equilibrium flow which is comoving with the rotating walls at boundaries [22]. To model the effect of the magnetic curvature, a radially outward “effective” gravity acting on the pressure was added to the system. Both the KH instability and the interchange instability were considered. The system was shown

²On the contrary, we assume free-slip boundary conditions throughout the main text of the dissertation. Simulations of spinning up plasma by imposing external currents have been tried — only with free-slip boundary conditions. Resolving the Hartmann layers in numerical studies would need very high resolution.

to be ideally KH stable if the generalized Rayleigh's Inflexion Theorem is satisfied, namely,

$$\frac{d}{dr} \left(\frac{\rho}{r} \frac{d}{dr} (r^2 \Omega) \right) \neq 0 \Rightarrow \text{marginal stable}, \quad (1.1)$$

where r is the radius and Ω is the angular frequency. On the other hand, the interchange growth rate in the absence of the velocity shear is:

$$\gamma_g = (-r\Omega^2 \rho'/\rho - gp'/p)^{1/2}, \quad (1.2)$$

where primes denote d/dr , and g is the "effective" gravity. The stability criterion for velocity shear stabilization of interchanges is given as

$$r^2 \Omega^2 > \gamma_g^2 \ln(R_\mu), \quad (1.3)$$

where R_μ is a Reynolds number based on the interchange growth time and the viscous and resistive time scales. If we denote R_c the radius of curvature of the magnetic field line, L_ρ the density scale size and L_p the pressure scale size, then $g \sim C_S^2/R_c$, $r\Omega' \sim R\Omega/a$, $\rho'/\rho \sim 1/L_\rho$, $p'/p \sim 1/L_p$. The schematic stability criterion is then

$$\frac{R}{a} > \left(\frac{a}{L_\rho} + \frac{1}{M_S^2} \frac{R}{R_c} \frac{a}{L_p} \right) \ln(R_\mu). \quad (1.4)$$

For a centrifugally confined fusion plasma, the pressure peaks at the center. That means the pressure stratification is inevitably destabilizing somewhere, and $L_p \sim a$. The density profile, on the other hand, could be either stabilizing or destabilizing. If only the pressure gradient is destabilizing, then a high sonic Mach number flow with $M_S^2 > (a/R_c) \ln(R_\mu)$ would be sufficient to stabilize the interchanges. However, if the density gradient is also destabilizing, then a large aspect ratio system with $R/a \gg 1$ might be needed. Condition (1.3) also indicates that the dissipation plays an essential, albeit weak, role.

(b) The fact that the effective gravity $g \sim C_S^2/R_c$ suggests that an elongated system may help the stability, since $R_c \sim L$. The stabilizing effect of elongation was studied analytically for the Z pinch [33], and was subsequently borne out by

numerical simulations [21]. The simulation showed a recovery to the laminar state in more than 95% of the volume at $M_S = 4 - 5$; a small, insignificant residual wobble remained at the center of the discharge. At commensurate Mach numbers, systems which are more elongated appear to be more stable. Although the stabilizing effect of elongation has not been checked in a centrifugal confinement system, its validity seems reasonable since the physical mechanism is essentially the same.

(c) Velocity shear stabilization of a centrifugally confined plasma was demonstrated in a simulation we reported in Chapter 2 [36]. The simulation was first run in 2D to obtain a laminar state. This 2D state was then seeded with three dimensional (3D) random noise to test its stability. The system remained stable in 3D. To identify velocity shear as the stabilizing mechanism, we reran the simulation in an artificial test in which the velocity shear was turned off, while artificial centrifugal forces, Coriolis forces, and viscous heating calculated from the laminar flow were retained in the equations to maintain the same 2D equilibrium. The artificial system became unstable to interchanges. However, when the velocity shear was restored, the convection cells of the interchanges were quickly torn apart and the system reverted to laminar again. The stabilization in this simulation was nearly complete, as no apparent residual wobble was observed.

(d) In Chapter 3 [38] we study the resistive MHD equilibrium and stability of a rotating plasma with particle sources. This study was motivated by an observation about the simulation reported in Chapter 2: The 2D laminar state used to study the 3D stability is in fact *not* a steady state; it is still slowly evolving on resistive time scales. We ask the following question: What is the final equilibrium state if we let the time go to infinity? Will it be a well-confined steady state? We find that in the absence of particle sources, as in the simulation of Chapter 2, the resistivity will eventually relax the magnetic field to nearly a vacuum field, and the plasma density will pile up against the outer wall. Therefore, particle sources would be needed to balance the resistive diffusion and attain a magnetically confined steady state. For

a non-rotating plasma, the resistive diffusion is driven by the pressure gradient, and the diffusion coefficient scales as $\eta\beta$, where η is the resistivity and $\beta \equiv 2p/B^2$ as usual [24, 47]. In a centrifugally confined plasma, not only the pressure gradient but also the centrifugal force drive the diffusion. One can show that the diffusion is roughly enhanced by a factor of $\sim (1 + M_S^2(a/r))$. From this point of view, a rotating plasma seems disadvantageous. There is, however, a corresponding advantage of a rotating plasma that now the density profile plays a significant role in stability. (On the contrary, the density profile is completely irrelevant to the stability of a static equilibrium [7].) Since the density profile depends on particle sources, the latter could be utilize to optimize the stability. More precisely, the slowly diffusing equilibrium we just mentioned is realizable only when the system is laminar. If the system is not laminar, the resulting turbulence will quickly flatten the profile before it can be built up. However, one can imagine that if the particle source is placed at the right place, a complete or almost complete laminar state could be possible. We performed a series of simulations for various density profiles with a 2D Dean flow model similar to the one mentioned in (a), except that isothermality was assumed for simplicity, and that the effective gravity was not included. The condition (1.3) was qualitatively checked. We also found that a completely laminar state could be achieved if (i) the density stratification is stabilizing at the “weakest” point where the flow shear vanishes ($\Omega' = 0$), and (ii) the KH criterion (1.1) is satisfied. If (i) is violated, localized interchanges emerge around the weakest point and the density profile there is flattened. On the other hand, if (ii) is violated, the characteristic Kelvin cat’s eye of the KH instability can form. In either case, the instability does not flatten the whole profile; rather, it brings the profile close to marginal stability, with some residual wobbles or convection cells. Residual wobbles or convection cells imply enhanced particle and heat loss in a real system; therefore these should be avoided. This would require judicious placement of the particle source.

(e) Chapter 4 is a generalization of the Dean flow analysis of Ref. [32] (which

we summarized above in (a)). As mentioned, the effect of magnetic curvature is modeled by an effective gravity acting on the pressure gradient in the Dean flow study. In this study we include a curved magnetic field explicitly. Another new ingredient in this study is to take into account the effect of low density plasma near the mirror throat (due to centrifugal confinement). In the usual MHD equations, it is assumed that the momentum of the electromagnetic (EM) field is negligible compared with the momentum of the plasma. Since (plasma momentum):(EM field momentum) $\sim 1 : V_A^2/c^2$, where c is the speed of light, this approximation is no longer appropriate as the plasma density becomes sufficiently low, such that $V_A \sim c$. To have a set of fluid equations which is valid even when $V_A \sim c$, we incorporate the full momentum equation into the MHD equations. The interchange instability is then studied within this framework. We find that the EM field itself acts as an effective mass. As a result, the inertia is increased by a factor of $(1 + V_A^2/c^2)$, while the interchange growth rate is reduced by a factor of $\sqrt{1 + V_A^2/c^2}$, as compared to the prediction of the usual MHD. Both Rayleigh’s inflexion criterion (1.1) and the velocity shear criterion (1.3) are generalized in this setting.

1.4 Magnetorotational and Parker Instability

An interesting question that often arises is “can a centrifugally confined plasma exhibit the MRI?” Workers are interested in the MRI because of its growing importance in understanding the angular momentum transport process in accretion disks. In addition, although the MRI has been studied in many simulations, attempts to observe it in laboratory experiments have just started. Recently, there have been several ongoing projects aimed at an experimental realization of the MRI [40, 53]; it would therefore be interesting to see whether a centrifugal confinement device could be used for this purpose, since the basic ingredients are present. From the perspective of the centrifuge as a viable fusion device, it is also important to ascertain if the MRI sets a limit to the operating parameter range. We address these

issues in Chapter 5 with a model of high β Dean flow resembling the one mentioned in Sec. 1.3(a), except that now we allow variations along the field [37]. A few assumptions are made to simplify the system without sacrificing the essential physics. Most importantly, we assume the plasma to be magnetically confined instead of wall confined, consistent with supersonic flow (i.e. $\rho r \Omega^2 \gg \nabla p$). The balance between centrifugal forces and the magnetic pressure requires:

$$\rho r \Omega^2 \lesssim B^2/a. \quad (1.5)$$

In the process of studying this system, it was established that the MRI effect is not the only possible destabilizing mechanism. There is another destabilizing mechanism, analogous to the magnetic buoyancy effect of the Parker instability, that couples to the MRI mechanism. To appreciate this, first let us briefly review the two mechanisms.

The most physically intuitive way to understand the MRI is probably the analogous “two orbiting mass points connected by a spring” model proposed by Balbus and Hawley (Fig. 1.3) [3, 4]. In this model, the spring is analogous to the restoring force of the magnetic field. In a system with outwardly decreasing angular frequency, the spring continuously transfers angular momentum from the leading inner mass point m_i to the lagging outer mass point m_o . Upon losing angular momentum, m_i can no longer stay in its original orbit and has to drop down to an even lower orbit. Likewise, m_o will escape to a higher orbit as a result of gaining angular momentum. This runaway process causes the instability. Conversely, if the angular frequency is outwardly increasing, one can easily see that the system should be stable. From this picture, it is also clear that the spring (or the magnetic field) has to be weak to have the MRI: if the spring is too strong, the two mass points will simply oscillate back and forth, and no further separation will be possible. When Balbus and Hawley rediscovered the MRI, local analysis was used to derive the dispersion relation and the stability criterion. This is appropriate for accretion disks since the disk size is much larger than the length scale of local disturbances. For

laboratory experiments, where the characteristic perturbation sizes are comparable to the system size, global eigenmode analysis is more appropriate. Yet it has been shown that even in such case, local analysis gives fairly good agreement with global analysis [40, 25]. For an ideal MHD incompressible fluid with an axial magnetic field, the local stability criterion is (see Appendix C):

$$k^2 V_A^2 > \frac{d\Omega^2}{d\ln(r)} \Rightarrow \text{stable}, \quad (1.6)$$

where k is the total wave number and V_A the Alfvén speed. The left hand side of Eqn. (1.6) is analogous to the natural frequency of the spring system.

The physical mechanism of the Parker instability can be understood as follows. Consider a plasma supported against gravity by a magnetic field, as depicted in Fig. 1.4(a), where the magnetic force $\mathbf{J} \times \mathbf{B}$ balances the gravitational force acting on the plasma. Suppose a small perturbation bends the magnetic field slightly, as shown in Fig. 1.4(b); the $\mathbf{J} \times \mathbf{B}$ force now has a horizontal component. This horizontal force compresses the plasma toward the valley, causing a density concentration. The gravitational force then further pulls down the density clump, together with the magnetic field due to the frozen-in condition; this completes the cycle. Meanwhile, as the plasma rolls downhill into the valley, the top region becomes lighter, therefore more buoyant. This is why this mechanism is sometimes called magnetic buoyancy. It is easy to see that the Parker instability is essentially a competition between the stabilizing magnetic and sonic restoring force and the destabilizing gravitational force. The stability criterion from local analysis can be shown to be [37]:

$$k^2 V_A^2 C_S^2 > g^2 \Rightarrow \text{stable}, \quad (1.7)$$

where g is the gravitational acceleration.

It is not hard to see why the two foregoing mechanisms are coupled in a centrifugally confined plasma, since both the centrifugal force (that replaces the gravity) and the flow shear (although in general not everywhere outwardly decreasing) are present. In the Dean flow model we mentioned, unstable modes were found both

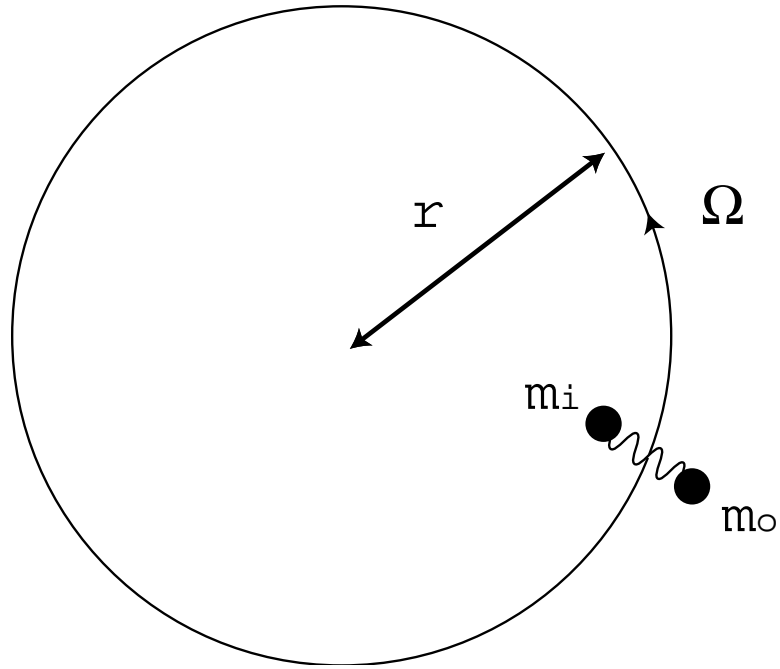


Figure 1.3: The “two mass points connected by a spring” model of the MRI. The magnetic field threaded through the disk acts as a spring which couples different fluid elements (represented by the two mass points m_i and m_o) together. If the equilibrium angular frequency is outwardly decreasing, then the spring transports angular momentum from the inner mass point m_i to the outer one m_o , causing the MRI.

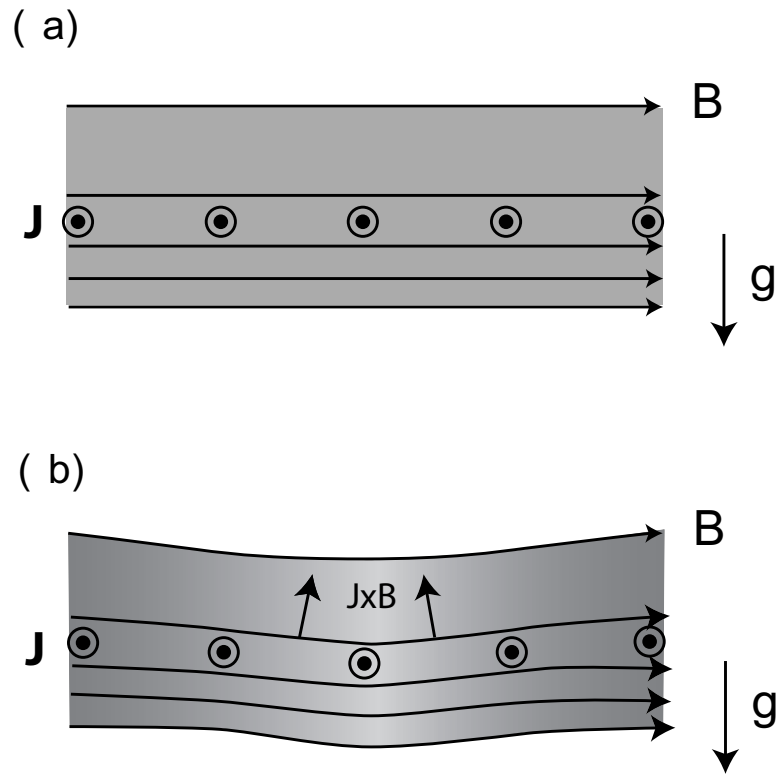


Figure 1.4: The mechanism of the Parker instability. (a) The $\mathbf{J} \times \mathbf{B}$ force supported the plasma against the gravity \mathbf{g} . (b) When the magnetic field is perturbed slightly, the horizontal component of the magnetic force compresses the plasma toward the center.

by a shooting code of the linearized eigenmode equation and by direct numerical simulation of the full MHD equations. The linear growth rate calculated from the two methods agrees. The question now arises: is the unstable mode MRI-like or Parker-like? Or does it show the characteristics of both? The linear theory can provide only very limited information. One way to think about this is to look at the incompressible limit of the system, which precludes the Parker instability. We found no unstable mode in this limit. Roughly speaking, this could be understood from the local criterion as follows. Schematically we can scale $d/dr \sim 1/a$, and notice that the total wave number $k \gtrsim \pi/a$ because the longest wavelength is limited by the system size. Therefore, from (1.6), to have the MRI we need

$$\pi^2 \frac{r}{a} < M_A^2, \quad (1.8)$$

where $M_A \equiv r^2 \Omega^2 / V_A^2$ is the Alfvén Mach number. However, from the assumption (1.5) we have

$$M_A^2 \lesssim \frac{r}{a}, \quad (1.9)$$

which means that the condition (1.8) can not be satisfied. In other words, the MRI mechanism is not able to destabilize the system because, in essence, a strong magnetic field is required to have a magnetically confined plasma. On the other hand, if we replace the gravity g in (1.7) by the centrifugal force $r\Omega^2$, we obtain the schematic criterion for the Parker instability:

$$\frac{r^2}{a^2} \pi^2 > M_S^2 M_A^2 \Rightarrow \text{stable}. \quad (1.10)$$

This agrees with the eigenmode results qualitatively. Therefore, it seems reasonable that the unstable mode is likely to be Parker-like instead of MRI-like. This was supported by nonlinear simulations as reported in Chapter 6, where the characteristic clumping behavior of the Parker instability was observed. We emphasize that our study does *not* preclude the possibility of studying the MRI in laboratory plasmas. To do MRI experiments with plasmas, however, one would have to relax the constraint (1.5); that means that the plasma has to be wall confined.

Chapter 2

Velocity Shear Stabilization of Centrifugally Confined Plasma

2.1 Introduction

In essence, nearly all magnetic schemes to confine plasmas for thermonuclear fusion are based on the idea that energetic charged particles gyrate tightly about a magnetic field line which is then configured to close on itself inside the system [24]. This requirement on closure of field lines (at least six confinement schemes are based on this idea) implies significant constraints in coil design. It would be desirable to relax this constraint, say by allowing “open” field configurations (wherein the field lines are not confined but the particles are). One well-known open configuration is the magnetic mirror [24]. This scheme relies on the mirror forces to reflect particles at the mirror throats and so contain plasma. But mirror reflection can contain plasma only up to a collision time, beyond which particles scatter into a “loss-cone” and are lost on the open field line. Another issue for mirrors is the MHD stability of the mirror: the magnetic configuration is inherently unstable to “flute” interchanges of field lines. Basically, a field line loaded with hot particles can interchange with one of cold particles thus releasing net potential pressure energy, akin to the Rayleigh–Taylor gravitational energy release in ordinary fluids. While it is possible to suppress this interchange in advanced mirror schemes, the latter come with greater magnetic coil complexity and, in any case, do not necessarily resolve

the loss-cone issue mentioned.

The centrifugally confined plasma scheme [48, 23] is an open field line configuration which holds the promise of overcoming these drawbacks. In the centrifuge scheme, a magnetic mirror type plasma is made to rotate azimuthally at supersonic speeds, in accordance with frozen-in $\mathbf{E} \times \mathbf{B}$ motion. The resulting centrifugal forces, given the field line curvature, prevent escape of ions along the open lines — the mirror forces become irrelevant and the loss-cone is erased. The MHD flute stability issue, however, is intricate and constitutes the subject of this Chapter. A quick assessment of flute stability goes as follows: at first glance, it would seem that the outward centrifugal force adds to the unfavorable gravitational acceleration and makes the interchanges even more potent. There is, however, a new ingredient — shear in the angular frequency of rotation (a sheared flow is inevitable for plasma situations): it has become increasingly clear over the last decade that flow shear can stabilize interchanges (among other plasma instabilities), basically by introducing a shearing frequency that tears apart convection cells before they can release energy [8, 30, 27]. Thus, the overall flute stability is a result of these competing effects. To make matters more complicated, gradients in the flow shear might introduce Kelvin–Helmholtz instabilities: the quick assessment is that the latter would likely, at worst, be slowly growing on account of the Rayleigh Inflexion Theorem [19]. Evidently, the issue of whether rotation shear would iron out the interchange needs resolution.

In this Chapter, we show by numerical simulation that a centrifugally confined plasma in a mirror type configuration is stable to the flutes, at Mach numbers of rotation of about 4. If this conclusion holds for a fusion-grade plasma (expected to be in the same dimensionless parameter range as our simulation), it allows consideration of a fusion device with a very simple coil configuration (among other advantages) [23].

2.2 Numerical Model

We solve numerically the 3D MHD and transport equations[11] in cylindrical (r, ϕ, z) coordinates. The governing equations are

$$\frac{\partial n}{\partial t} + \nabla \cdot (n\mathbf{u}) = 0, \quad (2.1)$$

$$\frac{\partial(nM\mathbf{u})}{\partial t} + \nabla \cdot (nM\mathbf{u}\mathbf{u}) = -\nabla(2nT + \frac{B^2}{8\pi}) + \frac{\mathbf{B}}{4\pi} \cdot \nabla\mathbf{B} + \nabla \cdot (nM\mu\nabla\mathbf{u}) + \mathbf{F}, \quad (2.2)$$

$$\begin{aligned} \frac{\partial T}{\partial t} + \nabla \cdot (T\mathbf{u}) &= \frac{1}{3}T\nabla \cdot \mathbf{u} + \frac{1}{n}\nabla \cdot (n\kappa_{\perp}\nabla T) \\ &+ \frac{1}{n}\hat{b} \cdot \nabla(n\kappa_{\parallel}\hat{b} \cdot \nabla T) + \frac{2}{3}M\mu r^2 \left| \nabla \left(\frac{u_{\phi}}{r} \right) \right|^2, \end{aligned} \quad (2.3)$$

$$\frac{\partial \mathbf{B}}{\partial t} = \nabla \times (\mathbf{u} \times \mathbf{B}) + \eta \frac{c^2}{4\pi} \nabla^2 \mathbf{B}. \quad (2.4)$$

Standard notation is used. The viscosity is assumed isotropic, the thermal conductivity is anisotropic with conduction along the field dominating that cross-field. Viscous heating is included, as this is the means by which centrifugal schemes could be heated [23]: for simplicity, we keep only the most significant term in the viscous heating (since the plasma is rotating supersonically in the ϕ direction, we expect $u_{\phi} \gg u_z, u_r$).

We use normalized units as follows: lengths are normalized to the simulation radial dimension a , the magnetic field B is normalized to a reference field B_0 , electron number density n is normalized to a reference density n_0 . Thus, speeds are normalized to the reference Alfvén speed $V_{A0} \equiv (B_0^2/4\pi n_0 M)^{1/2}$, and time is normalized to the Alfvénic time scale a/V_{A0} . It follows that energies and temperature are normalized to MV_{A0}^2 , the viscosity μ , and the thermal conductivities κ_{\perp} and κ_{\parallel} are each normalized to aV_{A0} , and resistivity η is normalized to $4\pi aV_{A0}/c^2$. The normalized equations are:

$$\frac{\partial n}{\partial t} + \nabla \cdot (n\mathbf{u}) = 0, \quad (2.5)$$

$$\frac{\partial(n\mathbf{u})}{\partial t} + \nabla \cdot (n\mathbf{u}\mathbf{u}) = -\nabla(2nT + \frac{B^2}{2}) + \mathbf{B} \cdot \nabla\mathbf{B} + \nabla \cdot (n\mu\nabla\mathbf{u}) + \mathbf{F}, \quad (2.6)$$

$$\frac{\partial T}{\partial t} + \nabla \cdot (T \mathbf{u}) = \frac{1}{3} T \nabla \cdot \mathbf{u} + \frac{1}{n} \nabla \cdot (n \kappa_{\perp} \nabla T) + \frac{1}{n} \hat{b} \cdot \nabla (n \kappa_{\parallel} \hat{b} \cdot \nabla T) + \frac{2}{3} \mu r^2 \left| \nabla \left(\frac{u_{\phi}}{r} \right) \right|^2, \quad (2.7)$$

$$\frac{\partial \mathbf{B}}{\partial t} = \nabla \times (\mathbf{u} \times \mathbf{B}) + \eta \nabla^2 \mathbf{B}. \quad (2.8)$$

Our simulation box is within two concentric cylindrical walls. The width of the box is 1, the inner cylinder is at radius 0.45, and the elongation in the z -direction is 5. For efficient centrifugal confinement, it is desired to have the ratio of the outermost to the innermost radius of a field line to be at least 3 [23]. The inner radius of 0.45 was picked for this reason and for numerical ease. The external magnetic field is, dominantly, a uniform field in the z direction plus the field of two additional “mirror” coils of radius 1.75 placed at the top and the bottom of the box. The latter coils produce the throats of the mirror. Since we impose periodic boundary conditions in the z direction, in practice we also place additional coils in periodic fashion along z , separated by a distance of 5 units. The latter coils are subdominant to the main field described earlier — for the simulation, we terminated the series at 20 extra coils above and below the box. The number of grid points in the simulations reported below was $60 \times 40 \times 100$.

As mentioned, periodic boundary conditions are imposed in z , as well as in the ϕ direction. The boundaries in r are assumed to be perfectly conducting hard walls: since field lines cut these walls in general, we assume zero flow at and into the walls, we let the perturbed normal magnetic field, \tilde{B}_r , be zero, and we assume that the perturbed transverse magnetic field satisfy $\partial_r \tilde{B}_z = 0$, $\partial_r (r \tilde{B}_{\phi}) = 0$, consistent with zero current at the walls. The growth rate of the interchange instability is much larger than resistive penetration rates through a conducting vessel wall; thus, the conducting wall boundary conditions used (“line-tying” and no flux penetration for the magnetic field) are reasonable¹. In addition, in a real system, a low temperature plasma with attendant high density of neutral atoms close to the walls provides a

¹For current-driven kink modes, it is well-known [24] that close fitting conducting shells reduce the growth rate; interchange mode growth rates are independent of the wall radius since these modes are well localized.

strong drag on plasma flow — thus the no-slip boundary conditions on the flow are reasonable also from this standpoint.

The temperature T at the radial walls as well as at the z-boundaries is kept at “room temperature” T_0 . This is achieved by putting in a heat sink term of the form $-(T - T_0)A \exp(-\alpha(\Delta x)^2)$ on the boundary, where A is a large constant, $\alpha \simeq 1/(\text{grid size})^2$ and Δx is the distance to the wall. This simulates radiation close to the walls, which would be expected and would keep the temperature low there.

The numerical algorithm is described in detail in Guzdar et al [28]. We began the simulation with uniform density and temperature at room temperature ($n = 1$ and $T = T_0$). The initial magnetic field was all due to the external coils. There was no rotation in the initial state. Further, we did not “seed” any noise in the toroidal direction initially, i.e., we first used the 3D code to attain a 2D azimuthally symmetric laminar state. For this run, we took the viscosity μ , the perpendicular thermal conductivity κ_{\perp} , and the resistivity η all to be 0.002. The parallel thermal conductivity κ_{\parallel} was set to be $200\kappa_{\perp}$. The room temperature T_0 was set to be 0.002. With this initial condition, we now applied a force, $F_{\phi} = 8\mu$, in the ϕ direction to model the $I \times B$ forces on the plasma (other methods of “start-up” were tried, e.g., imposed radial currents at the top and the bottom also spun up the plasma; see Appendix A for an explanation about how this could be done). Because of the applied force, the plasma started rotating in the ϕ direction. With building speed, the centrifugal force was then seen to push the plasma towards the midplane. The temperature rose due to viscous heating, especially in the flanks, with heat conducting toward the midplane. After about 300 time units from the onset of the driving force, the system came to an approximate steady state.

Fig. 2.1 shows the temperature and the pressure profiles of this 2D laminar state. The pressure is localized to a peak in the center. All the temperature rise results from viscous heating. Temperature contours tend to match magnetic field lines because of the much higher thermal conductivity along the field line. Fig. 2.2

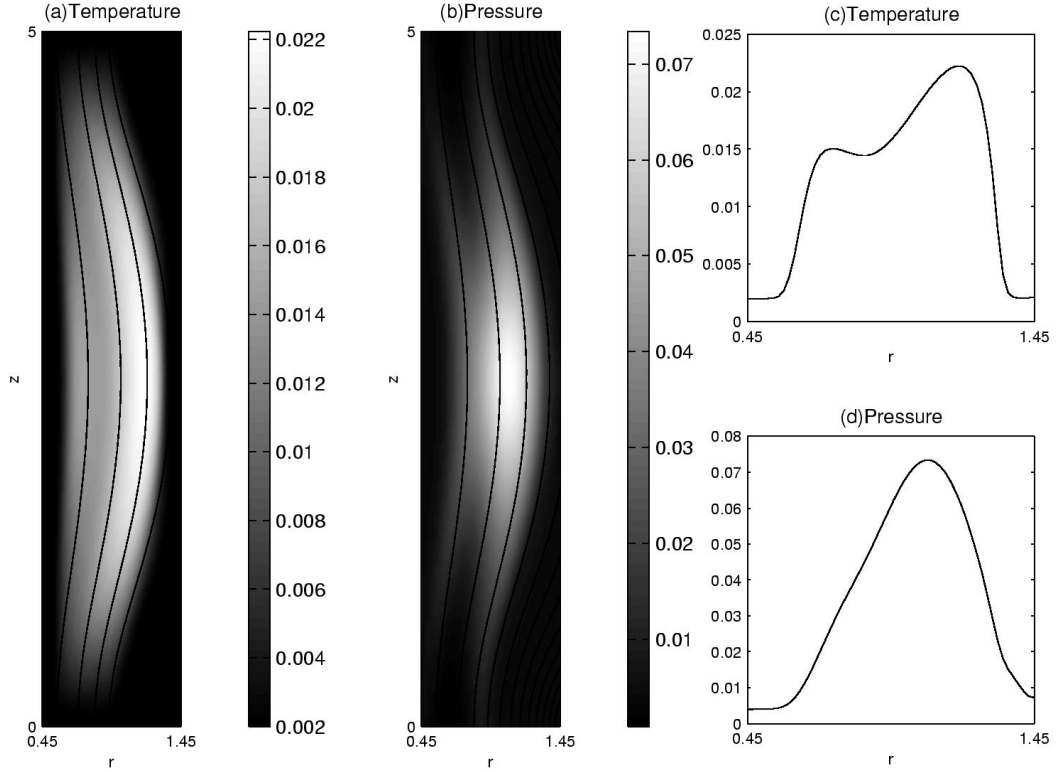


Figure 2.1: The 2D laminar profiles: (a) temperature and (b) pressure, with magnetic field lines overlaid. A cut of the temperature at midplane is shown in (c). Likewise, (d) is a pressure cut.

shows the density and angular velocity profiles. The angular velocity of rotation, Ω , self-consistently ended up being a flux function, as predicted by theory [23]. The shear flow is clearly evident given the no-slip boundary conditions. The central Mach number is a key parameter. We define the Mach number M_S by $M_S^2 = u_\phi^2/T$. For this run, we achieved a maximum Mach number of $M_S = 4$ at the center. The pressure drop $p_{max}/p_{min} = 86$, and the Alfvén Mach number was $M_A = 0.3$. This laminar state shows that centrifugally confined plasmas can provide reasonable profiles for a fusion device.

This steady state was now seeded with random noise, in all coordinates, of the size 10^{-4} in density and all flow variables. The fastest growing instability was

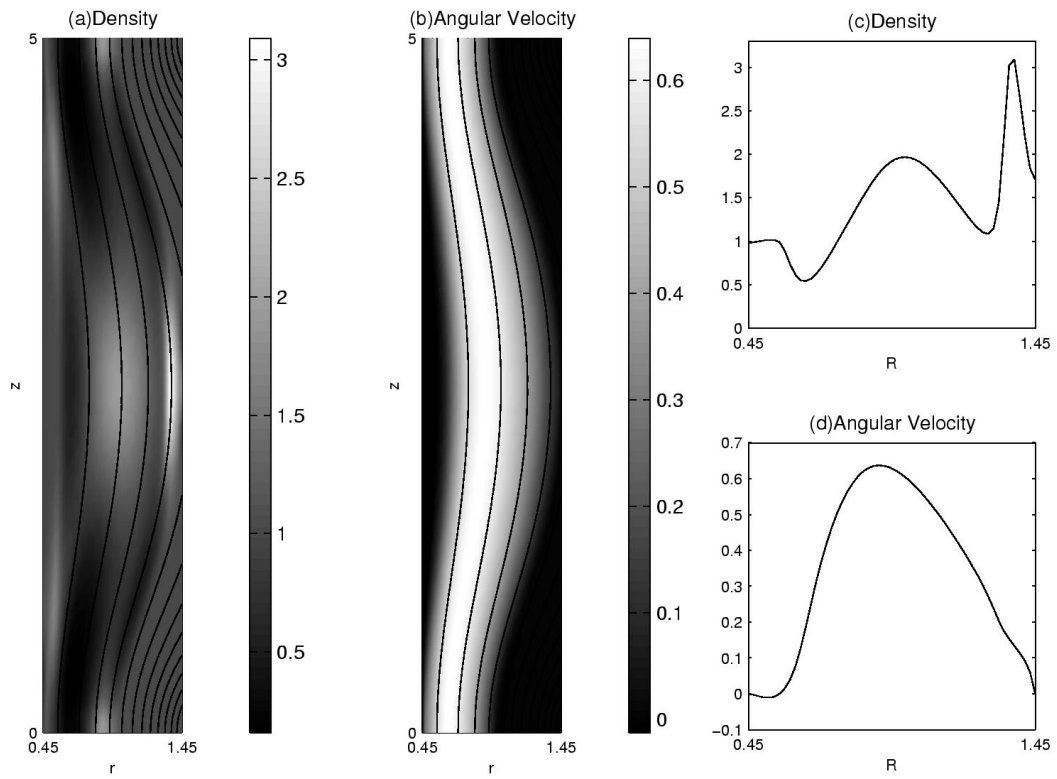


Figure 2.2: More 2D laminar profiles: (a) density and (b) angular velocity, with magnetic field lines overlaid. A cut of the density at midplane is shown in (c). Likewise, (d) is an angular velocity cut.

expected to have a toroidal wavelength of the order of $\pi/6$. Thus, for numerical ease, we reduced the box size in ϕ and imposed periodic boundary conditions over the range $\phi = [0, \pi/3]$ (this was remedied in other runs wherein we confirmed that longer wavelengths were not an issue by increasing the box size). This 3D random noise test was allowed to run for more than 60 time units, much longer than the expected growth times (of the order of tens of time units). There was no sign of the characteristic interchange instability and breakup of the laminar state: the random noise was initially seen to smooth out, some mild undulation in ϕ was then seen, at wavelengths of the order of $\pi/3$ radians, and this undulation then settled down to a small wobble with amplitude less than 1%. A wobble had been observed in a Z -pinch simulation done earlier [21] and so was expected in our simulation, but the size of the wobble was found to be considerably smaller than expected. For all practical purposes, this simulation indicated that the laminar state was maintained. As mentioned above, we experimented with longer box sizes in ϕ ($\pi/2$, π , and 2π) as well as differing resolution. We also started the simulation from scratch (no rotation), but including random noise. No evidence was found in any case that would equivocate the conclusion that the system is stable.

Because we saw no breakup of the system, it was important to find a counterexample where the code did produce a characteristic interchange breakup. To be sure, Cartesian versions of this code have shown large scale, nonlinear, turbulent behavior [21]. In addition, our stable result is consistent with theoretical analysis which suggests stabilization at Mach numbers somewhat larger than unity [30]. Nonetheless, we looked for an unstable situation to test in the present case. One possibility was to rerun the simulation with no shear in the angular frequency, i.e., configure the system such that Ω' were zero and the entire plasma were rigidly rotating. Then, there would be instability (since one can then transform to a frame in which the centrifugal force would go as R and there would no velocity shear). This test, unfortunately, cannot be implemented for the centrifuge system without

changing too many things that would then make the comparison meaningless: if we set up an equilibrium with $\Omega' = 0$, there would be no viscous heating (see Eq. (2.7)); thus, the temperature would be a constant and the density profile would adjust to compensate. As a result, we would be comparing two different situations. In order to carry out a test that would maintain the density and temperature profiles but minimize the velocity shear, we settled on an “artificial” test. We took the final output frame of the 3D seeded code above and “froze” the centrifugal and Coriolis accelerations as well as the viscous heating as follows: In the momentum equation, Eq. (2.2), we “froze” the terms corresponding to the Coriolis and centrifugal accelerations, set the applied force \mathbf{F} to zero, and reset all the remaining flow terms to zero as the initial condition. The new momentum equation then looked like

$$\begin{aligned} \frac{\partial(n\mathbf{u})}{\partial t} + \nabla \cdot (n\mathbf{u}\mathbf{u}) = & -\nabla(2nT + \frac{B^2}{2}) + \mathbf{B} \cdot \nabla\mathbf{B} \\ & + \nabla \cdot (n\mu\nabla\mathbf{u}) - 2n\Omega_0 \times \mathbf{u} - n\Omega_0 \times (\Omega_0 \times \mathbf{r}). \end{aligned} \quad (2.9)$$

Here, Ω_0 is the rotation frequency function frozen from the previous run. Note that the variable \mathbf{u} , while set to zero initially, is free to evolve. Concomitantly, the density n in front of the centrifugal term is free to evolve. Thus, we are starting from a situation where there are destabilizing accelerations but no flow shear — and no possibility of flow shear build up since the applied force \mathbf{F} is zero. Note also that in the initial state, the above equation keeps the system in equilibrium and no equilibrium pressure profile adjustments will occur at restart. Likewise, we also froze the heating terms in the temperature equation. In particular, in Eq. (2.6), we froze the viscous heating term to keep it at $(2/3)\mu r^2 |\nabla\Omega_0|^2$. This form of the heat equation ensures that there will be no temperature adjustments on the transport time scale.

We now restarted with random noise as before. The discharge went unstable. Fig. 2.3 shows the pressure on the $r - \phi$ cut through the midplane at $t = 0, 70, 83, 89, 95,$ and 101 . The characteristic “mushrooms” associated with an interchange are clearly visible and the entire discharge is effectively destroyed. Continuation of

the run at this stage would produce turbulence. We now restored velocity shear: we reintroduced the force \mathbf{F} , at the same level as before, and restarted from the last frame of Fig. 2.3, except that u_ϕ was set to $r\Omega_0$ as an initial condition. The Coriolis and the centrifugal terms were now turned off. The discharge now recovered. The pressure profiles on the $r - \phi$ midplane cut at $t = 0, 3.5, 7, 10.5, 17.5,$ and 63 are shown in Fig. 2.4. The discharge was stabilized and the laminar state was almost completely recovered at $t = 63$.

2.3 Conclusion

In conclusion, our numerical experiment demonstrates the existence of a stable, centrifugally confined plasma within a magnetic configuration that is relatively simple. It is incontrovertible that a simple magnetic mirror is grossly flute unstable, and would be even more so under rigid rotor azimuthal rotation. We have shown that strong velocity shear renders the system laminar. Analytic calculations in progress support this numerical finding. This is a very attractive idea for a fusion device. Supersonic rotation is required but this is precisely what is also required for the containment of the plasma by centrifugal forces [23]. The system we consider is of small Larmor radius and, accordingly, the simulation is based on ideal MHD. Drift instabilities, by definition for this system, have lower growth rates and shorter wavelengths and are not included in this description. The lower growth rate, however, means our large velocity shear would be strongly stabilizing; the shorter wavelengths would imply that these instabilities would not disrupt the discharge but, at worst, cause turbulent transport. All frequencies considered are below the ion-cyclotron frequency, at least for long wavelengths. Thus, kinetic cyclotron effects, again, would not be grossly disruptive. Clearly, however, both drift and kinetic effects would have to be included in a more encompassing study.

An experiment currently under construction should be able to test this result [23]. The experimental plan allows for extra coils to produce an azimuthal field to

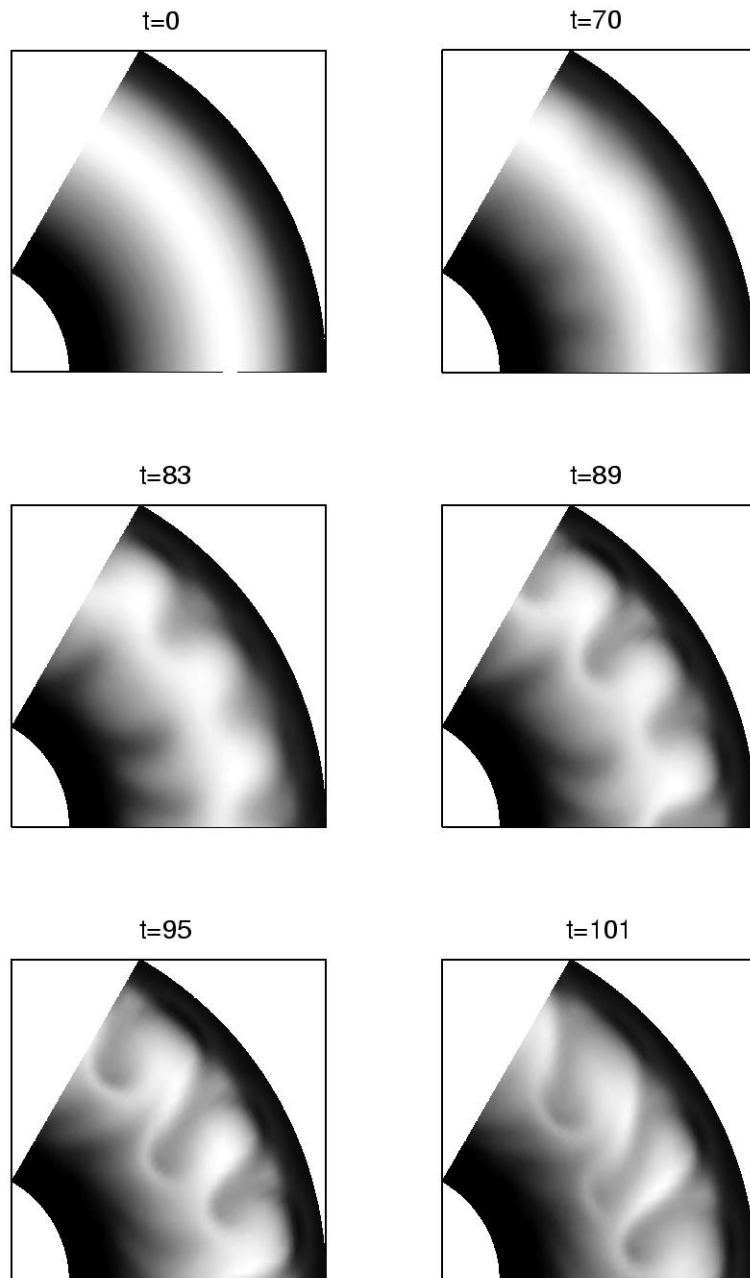


Figure 2.3: The time evolution of the pressure on the $r - \phi$ midplane of the test without velocity shear.

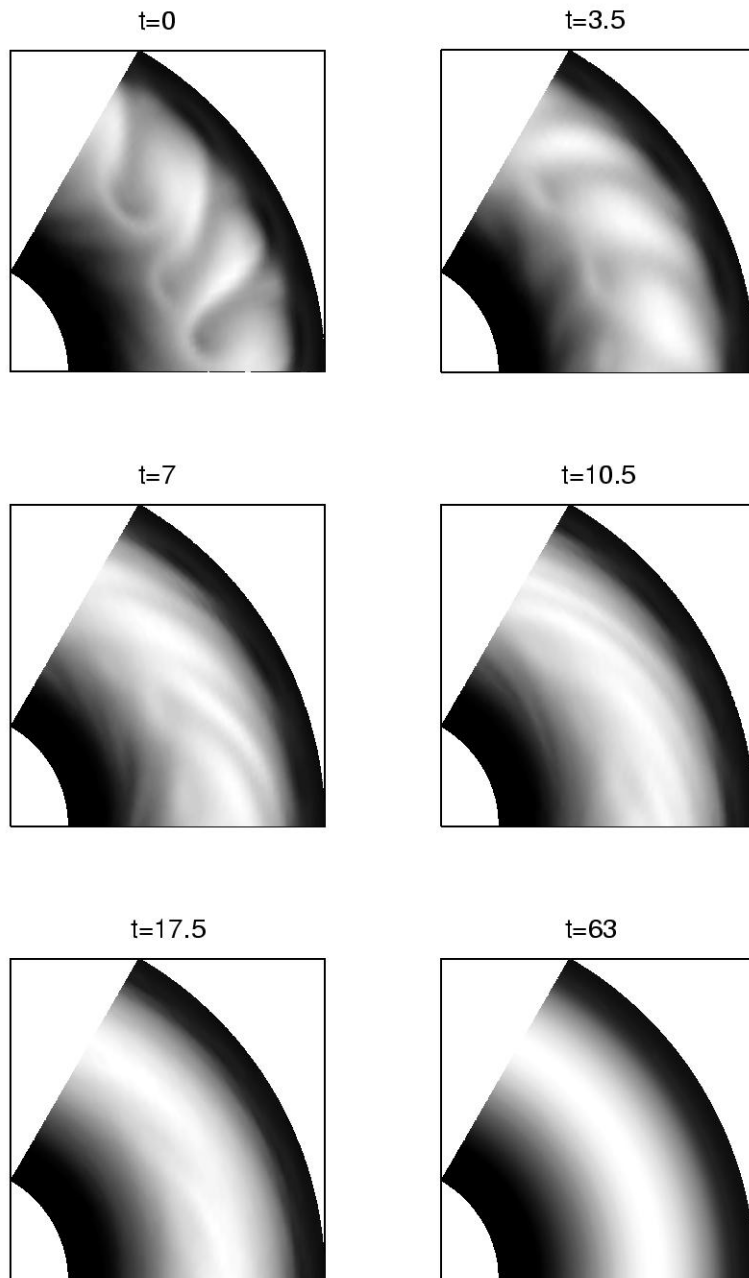


Figure 2.4: Stabilization from restoring velocity shear.

assist velocity shear stabilization of interchange instability, if needed. The present simulation, albeit at Reynolds numbers smaller than expected in the experiment, suggests the azimuthal field may not be needed.

Chapter 3

Resistive Magnetohydrodynamic Equilibrium and Stability of a Rotating Plasma with Particle Sources

3.1 Introduction and Motivation

This Chapter is motivated by two observations from the 3D simulation of Chapter 2 [36]. First, the two-dimensional (2D) steady state in that study was in fact, not steady; it was still slowly evolving on transport time scales. Since the ultimate goal of the centrifugally confined fusion plasma is to operate in a steady state [31], a closer examination is needed. If the axial magnetic field is straight, one can easily show that in the absence of particle sources or an auxiliary electric current drive, resistivity (which was explicitly included in Ref. [36]) will eventually bring the toroidal current down to zero (this can be shown as follows: the toroidal electric field $E_\phi = 0$ in a steady state. If the flow is toroidal $\mathbf{u} = u_\phi \hat{\phi}$ and the magnetic field is axial $\mathbf{B} = B_z \hat{z}$, then the Ohm's law (3.3) implies that the toroidal current $J_\phi = 0$); hence in a steady state the centrifugal force can only be balanced by the pressure gradient and the confinement is essentially lost, as the density has to pile up toward the outside of the system to provide the necessary pressure gradient. In a centrifugally confined plasma, however, the magnetic field is a curved mirror field. The effect of the magnetic curvature on resistive relaxation is not all obvious. In an axisymmetric rotating plasma with a curved poloidal magnetic field, one can demonstrate the existence of poloidal convection cells as follows. Suppose there is no poloidal

convection, then the toroidal current $J_\phi = 0$ from the Ohm's law (3.3); therefore the centrifugal force is balanced by the pressure gradient alone, i.e. $\rho r \Omega^2 \hat{r} = \nabla p$. However, the curl of this equation yields $\partial_z(\rho r \Omega^2) = 0$ which, in general, is not true when the magnetic field is curved; therefore there is a contradiction. The poloidal convection, together with the poloidal magnetic field, drives a toroidal current via the electromotive force (e.m.f) $\mathbf{u} \times \mathbf{B}$, where \mathbf{u} is the plasma flow and \mathbf{B} is the magnetic field. The operative question then is: Is this toroidal current sufficient to maintain a well confined plasma in the absence of particle sources? In Sec. 3.2 we address this question by studying the slowly diffusing plasma, in the spirit of the classic work of Kruskal and Kulsrud [47]. We show that in spite of the nonvanishing toroidal e.m.f. the conclusion is essentially the same; i.e., in the absence of particle sources, the resistivity relaxes the magnetic field to nearly a potential field and the density piles up toward the outside of the system as a result. Therefore, to have a confined steady state one has to introduce particle sources (and sinks) into the system. The governing equations for the slowly diffusing plasma then determine the density profile for a given particle source.

The second observation from the study of Chapter 2 [36] is that the system in that case was very stable. There was no sign of the type of wobbles observed in a previous Z pinch simulation [21]. The superior stability should nevertheless not be regarded as a general result, and we will try to give an explanation in this Chapter. Based on theoretical understandings [30, 32, 6], there are at least two factors that could be relevant to the overall stability of the system: First, the stability may weakly depend on dissipation such as the viscosity and the resistivity, etc.[30] Second, the density, the pressure, and the flow profiles, as well as the interplay between them might be important for the stability. For example, the generalized Rayleigh's criterion depends on both the density and the flow profiles [32]. Another example is that found by Benilov et al. [6] and in Ref. [21] that unstable modes could be localized about an extremum of the velocity profile. Therefore, in this work

we numerically study the stability for different profiles and dissipation coefficients. Through these simulations, we wish to establish a “rule of thumb” for stability. Our simulations are done with a 2D, isothermal Dean flow model. Although this model is less realistic compared to the one in Ref. [36], we made this choice for the following reasons: First, 2D simulations are much less expensive, thus allowing an extensive study. Second, the sources required to maintain a given density profile can be calculated rather easily, allowing precise control over the density profile. We find that profiles play an important role in the stability. This finding suggests that we might utilize particle sources to optimize the stability.

This Chapter is organized as follows. In Sec. 3.2, we establish that particle sources are necessary to achieve a confined steady state without density piling-up, and that the density profile can be controlled by particle sources. In Sec. 3.3 we describe the numerical model of the 2D Dean flow. We then perform a series of stability simulations for different profiles and dissipation coefficients; the results of those simulations are presented in subsequent sections 3.4 and 3.5. In Sec. 3.4 we study the aspect ratio and the Reynolds number dependence of velocity shear stabilization, which, qualitatively, confirms the theoretical prediction of Ref. [32]. We also discuss the interplay between the density profile and the flow profile in this section. The KH instability is discussed in Sec. 3.5. Several other issues, namely, hysteresis, asymmetric particle sources, the generalized Ohm’s law and the thermoelectric effect are addressed in Sec. 3.6. We conclude in Sec. 3.7.

3.2 Slowly Diffusing Steady State of Rotating Plasma

The governing equations for the resistive MHD steady state of a rotating plasma are [47]:

$$\nabla \cdot (\rho \mathbf{u}) = S, \tag{3.1}$$

$$\rho \mathbf{u} \cdot \nabla \mathbf{u} = -\nabla p - \frac{\nabla B^2}{2} + \mathbf{B} \cdot \nabla \mathbf{B}, \tag{3.2}$$

$$\mathbf{E} = -\nabla\Phi = -\mathbf{u} \times \mathbf{B} + \eta\mathbf{J}, \quad (3.3)$$

$$\mathbf{J} = \nabla \times \mathbf{B}. \quad (3.4)$$

Standard notation is used. ρ is the plasma density, S the particle source, E the electric field, Φ the electrostatic potential, \mathbf{u} the plasma flow, p the pressure, \mathbf{B} the magnetic field, η the resistivity, and \mathbf{J} the electric current. For simplicity, we take Ohm's law (3.3) in its simplest form. In the rest of the study, we denote (r, ϕ, z) as the standard cylindrical coordinate system and $(\hat{r}, \hat{\phi}, \hat{z})$ the corresponding coordinate unit vectors.

For simplicity, we only consider axisymmetric systems, and we assume a purely poloidal magnetic field. Hence, the magnetic field can be expressed in terms of the flux function ψ :

$$\mathbf{B} = \nabla\phi \times \nabla\psi. \quad (3.5)$$

We can then express the electric current as:

$$\mathbf{J} = \nabla \times (\nabla\phi \times \nabla\psi) = r^2 \nabla \cdot \left(\frac{\nabla\psi}{r^2} \right) \nabla\phi. \quad (3.6)$$

Taking Eq. (3.3) along three independent directions \mathbf{B} , $\nabla\psi$, and $\hat{\phi}$, we have

$$\mathbf{B} \cdot \nabla\Phi = 0, \quad (3.7)$$

$$-\nabla\psi \cdot \nabla\Phi = |\nabla\psi|^2 \mathbf{u} \cdot \nabla\phi, \quad (3.8)$$

$$\mathbf{u} \cdot \nabla\psi = \eta r^2 \nabla \cdot \left(\frac{\nabla\psi}{r^2} \right). \quad (3.9)$$

From Eq. (3.7), Φ is a flux function $\Phi(\psi)$. If we define the angular velocity $\Omega = u_\phi/r$, Eq. (3.8) gives $\Omega = -d\Phi/d\psi$, which means each field line rotates as a rigid rotor. The physical meaning of Eq. (3.9) is that the toroidal electric current is driven by the e.m.f. from the poloidal flow together with the poloidal magnetic field. From Eq. (3.9) we can see that poloidal flow scales as η , which we assume to be small. Hence we assume the ordering $\mathbf{u}_\perp \ll u_\phi$, where the “ \perp ” denotes the poloidal component. Under this assumption, the momentum Eq. (3.2) is approximately

$$-\rho r \Omega^2 \hat{r} = -\nabla p - \nabla \cdot \left(\frac{\nabla\psi}{r^2} \right) \nabla\psi. \quad (3.10)$$

Taking Eq. (3.10) along two independent directions \hat{b} and $\nabla\psi$, where \hat{b} is the unit vector along \mathbf{B} , we obtain:

$$\rho r \Omega^2 \hat{r} \cdot \hat{b} = \hat{b} \cdot \nabla p, \quad (3.11)$$

$$(\rho r \Omega^2 \hat{r} - \nabla p) \cdot \nabla \psi = \nabla \cdot \left(\frac{\nabla \psi}{r^2} \right) |\nabla \psi|^2. \quad (3.12)$$

Now we assume that the plasma is enclosed by surfaces (e.g., the walls of the chamber) on which $\mathbf{u} = 0$. Integrating Eq. (3.1) over the volume where $\psi \leq c$, with any constant c , we get:

$$\int_{\psi \leq c} S d\tau = \int_{\psi=c} \frac{\rho \mathbf{u} \cdot \nabla \psi}{|\nabla \psi|} d\sigma, \quad (3.13)$$

where $d\tau$ is the volume element and $d\sigma$ the surface area element. Using (3.9) and (3.12) into (3.13), we get

$$\int_{\psi \leq c} \frac{S}{\eta} d\tau = \int_{\psi=c} \frac{\rho r^2 (\rho r \Omega^2 \hat{r} - \nabla p) \cdot \nabla \psi}{|\nabla \psi|^3} d\sigma. \quad (3.14)$$

If there is no particle source, the left hand side (LHS) of (3.14) is zero. The right hand side (RHS) then implies that the centrifugal force is essentially balanced by the pressure gradient alone, although in some average sense on each flux surface. Therefore, we conclude that even when the magnetic field is curved, particle sources are still necessary to have a resistive MHD equilibrium without density piling-up. For a solution of Eq. (3.10), we can use Eq. (3.14) to calculate the particle source needed to maintain that equilibrium. We may estimate the amount of the particle source needed to maintain a steady state from Eq. (3.14). If there is no rotation, $\Omega = 0$, then $S \sim \eta \beta \rho / a^2$, where $\beta \equiv 2p/B^2$ as usual, and a is the radial size of the system. When the system is rotating supersonically, however, the centrifugal force term in Eq. (3.14) dominates the pressure gradient term. In that case, we have $S \sim (1 + M_S^2 a/r) \eta \beta \rho / a^2$, where M_S is the sonic Mach number; i.e., the cross-field particle loss is enhanced approximately by a factor of $(1 + M_S^2 a/r)$ because of the centrifugal force.

If we assume an equation of state $p = \rho T$ with $T = T(\psi)$, the system can be

further simplified. Under these assumptions, Eq. (3.11) can be simplified as

$$\hat{b} \cdot \nabla \left(\ln(\rho) - \frac{r^2 \Omega^2}{2T} \right) = 0. \quad (3.15)$$

Therefore, we can express ρ as

$$\rho = f(\psi) \exp(r^2 \Omega^2 / 2T). \quad (3.16)$$

Substituting (3.16) into (3.12) and (3.14), after some algebra, we get

$$- \left(T \frac{df}{d\psi} + \left(r^2 \Omega \frac{d\Omega}{d\psi} + \left(1 - \frac{r^2 \Omega^2}{2T} \right) \frac{dT}{d\psi} \right) f \right) \exp \left(\frac{r^2 \Omega^2}{2T} \right) = \nabla \cdot \left(\frac{\nabla \psi}{r^2} \right), \quad (3.17)$$

and

$$q(\psi) f \frac{df}{d\psi} + g(\psi) f^2 = h(\psi), \quad (3.18)$$

where $q(\psi)$, $g(\psi)$, and $h(\psi)$ are flux functions defined on each flux surface $\psi = c$ as

$$q(c) = \int_{\psi=c} \frac{T r^2 \exp(r^2 \Omega^2 / T)}{|\nabla \psi|} d\sigma, \quad (3.19)$$

$$g(c) = \int_{\psi=c} r^2 \exp(r^2 \Omega^2 / T) \left(r^2 \Omega \frac{d\Omega}{d\psi} + \left(1 - \frac{r^2 \Omega^2}{2T} \right) \frac{dT}{d\psi} \right) \frac{d\sigma}{|\nabla \psi|}, \quad (3.20)$$

and

$$h(c) = - \int_{\psi \leq c} \frac{S}{\eta} d\tau. \quad (3.21)$$

The solution of Eq. (3.18) can be formally written as

$$f^2 = \frac{1}{k} \left(\int \frac{2kh}{q} d\psi + const \right), \quad (3.22)$$

where k is a flux function defined as

$$k(\psi) \equiv \exp \left(\int^{\psi} \frac{2g}{q} d\psi \right), \quad (3.23)$$

and the constant of integration is determined by the total mass.

Our system of equations now consists of a Grad–Shafranov-like equation (3.17) and an auxiliary condition (3.18). The general procedure to solve this system for given $T(\psi)$, $\Omega(\psi)$, and S is as follows. First we have to solve ψ and $f(\psi)$ by solving

(3.17) and (3.18) simultaneously. Then we can use (3.16) and (3.9) to determine ρ and the poloidal flow perpendicular to the field line. Finally, to complete the pattern of convection cells, we can use (3.1) to determine the poloidal flow along the field line. This solution represents a slowly diffusing equilibrium of a rotating plasma with poloidal convection cells. In the low- β (i.e., $p/B^2 \ll 1$, $\rho r^2 \Omega^2 / B^2 \ll 1$) limit, we can approximate ψ by the vacuum flux function provided by the external field. Therefore we do not have to solve the coupled equations (3.17) and (3.18) simultaneously, and the solution can be largely simplified.

3.3 Numerical Model

In the previous section we set up the governing equations for slowly diffusing equilibria. Solving the equilibrium for given particle sources and external coils is in general complicated. We make no attempt to solve it in this study. Rather, we would like to address an even more important issue, viz., the stability, since such an equilibrium is physically realizable only when it is stable. In the following sections we will address this issue by numerical simulations. For the reasons mentioned in the Introduction, our simulation will be limited to a 2D Dean flow model on the $r - \phi$ plane, namely, an annular flow which is no-slip at edges, with a threaded axial magnetic field. The equilibrium is therefore one dimensional (1D), with r dependence only.

Our numerical model is governed by the following set of equations:

$$\partial_t \rho + \nabla \cdot (\rho \mathbf{u}) = S, \quad (3.24)$$

$$\rho \partial_t \mathbf{u} + \rho \mathbf{u} \cdot \nabla \mathbf{u} = -T \nabla \rho - \frac{\nabla B^2}{2} + \mathbf{B} \cdot \nabla \mathbf{B} + \mu \nabla^2 \mathbf{u} + F \hat{\phi}, \quad (3.25)$$

$$\partial_t \mathbf{B} = -\nabla \times \mathbf{E}, \quad (3.26)$$

$$\mathbf{E} = -\mathbf{u} \times \mathbf{B} + \eta \nabla \times \mathbf{B}. \quad (3.27)$$

The plasma is assumed isothermal for simplicity. A force in the azimuthal direction is applied to spin up the plasma. Assuming $\partial_z = 0$, we numerically solve the system

in the $r - \phi$ plane. The numerical algorithm is described in detail in Ref. [28]. The simulation was done in the region $[R, R+1] \times [0, \phi_0]$, which represents a section of the full annulus. We define the aspect ratio as inner radius divided by the radial box size. For the chosen simulation box, the aspect ratio is R . Periodic boundary conditions are imposed in the ϕ direction. The chosen simulation box length $L \equiv (R + 1/2)\phi_0$ was sufficient to study both the long wavelength KH modes and the short wavelength interchange modes. The boundaries in r are no-slip, perfectly conducting hard walls. The resolution of the simulations reported here is 100×100 .

Assuming an axisymmetric particle source, the 1D equilibrium with $\mathbf{u} = u_r \hat{r} + u_\phi \hat{\phi}$ and $\mathbf{B} = B \hat{z}$ is determined by:

$$\frac{1}{r} \frac{d(r\rho u_r)}{dr} = S, \quad (3.28)$$

$$-\frac{d}{dr} \left(\rho T + \frac{B^2}{2} \right) + \rho u_\phi^2 / r = 0, \quad (3.29)$$

$$\rho u_r \frac{du_\phi}{dr} + \rho \frac{u_\phi u_r}{r} = F + \mu \left(\frac{1}{r} \frac{d}{dr} \left(r \frac{du_\phi}{dr} \right) - \frac{u_\phi}{r^2} \right), \quad (3.30)$$

$$E_\phi = u_r B - \eta \frac{dB}{dr} = 0, \quad (3.31)$$

where in Eq. (3.29) we neglect some small terms proportional to u_r . This is justified since Eq. (3.31) implies $u_r \sim \eta$, and η is small.

From the hard wall boundary condition, $u_r|_{wall} = 0$. Hence, (3.31) implies $dB/dr|_{wall} = 0$, which, together with the no-slip boundary condition $u_\phi|_{wall} = 0$ and (3.29), imply $d\rho/dr|_{wall} = 0$. Except for those just mentioned, there are no further constraints on the equilibrium profile. For any given $\rho(r)$ and $u_\phi(r)$, the required particle source S and applied force F can be determined as follows. Eq. (3.29) determines B^2 up to a integration constant; with the B so obtained, Eq. (3.31) determines u_r ; Eq. (3.28) then determines the particle source S . The applied force F can be determined by using Eq. (3.30).

3.4 Velocity Shear Stabilization

Velocity shear stabilization of interchanges in Dean flow was studied analytically in Ref. [32]. The stability criterion, based on a conservative estimate of negligible growth, is

$$R^2\Omega'^2 > \gamma_g^2 \ln(R_\mu), \quad (3.32)$$

where

$$\gamma_g = (-R\Omega^2 \rho' / \rho)^{1/2} \quad (3.33)$$

is the growth rate without velocity shear, R_μ is a Reynolds number, and primes denote derivative with respect to r . Since we do not include the effective gravity introduced in Ref. [32], the γ_g here does not depend on p' . Our first task is to test this theory in more detail. Given the somewhat arbitrary nature of the criterion, we limit ourselves to a qualitative confirmation. Two qualitative predictions can be deduced from the criterion (3.32). First, for the same unstable density profile and shear flow, larger R (aspect ratio) systems would be more stable, since $\gamma_g \sim 1/\sqrt{R}$. Second, the efficacy of the velocity shear stabilization decreases with a decrease of dissipative coefficients, somewhat counter-intuitively. We will examine these two predictions in this section.

We choose the equilibrium density profile

$$\rho_0 = 1 + A \cos(\pi x), \quad (3.34)$$

where $x \equiv r - R$. And we choose the flow profile to be the solution of

$$F_0 + \mu \left(\frac{1}{r} \frac{d}{dr} \left(r \frac{du_{\phi 0}}{dr} \right) - \frac{u_{\phi 0}}{r^2} \right) = 0, \quad (3.35)$$

i.e., the velocity profile driven by a constant applied force, subject to no-slip boundary conditions. In the limit $R \gg 1$, the flow is approximately parabolic, $u_{\phi 0} \simeq (F_0/2\mu)x(1-x)$. We choose $A = 0.5$, $F_0/\mu = 32$ for this simulation. The temperature is set to be unity. As mentioned, B^2 is determined up to an integration

constant from Eq. (3.29). We choose the constant such that $B(x = 1/2) = 5$. For the parameters we choose, the sound speed $C_S = 1$; the peak of $u_{\phi 0}$ corresponds to Mach number $M_S \equiv u_{\phi 0}/C_S \simeq 4$.

3.4.1 Cases with No Velocity Shear

As a benchmark, we first did some simulations with no velocity shear. Since no background flow is present, the centrifugal force from the rotation was replaced by an artificial gravity pointing outwardly. More precisely, Eq. (3.2) was replaced by

$$\rho \partial_t \mathbf{u} + \rho \mathbf{u} \cdot \nabla \mathbf{u} = -T \nabla \rho - \frac{\nabla B^2}{2} + \mathbf{B} \cdot \nabla \mathbf{B} + \mu \nabla^2 \mathbf{u} + \rho g_c \hat{r}, \quad (3.36)$$

where $g_c \equiv u_\phi^2/r$, with u_ϕ being the steady flow. In this way, we can use the same source term to maintain the same density profile in this artificial system.

We ran the simulation for $R = 2, 4, 6, 8$, and 10 ; and we took $\mu = \eta = 0.002$. As we varied the radius R , we kept the box length $L \equiv (R + 1/2)\phi_0 = 2$; i.e., the simulation box was approximately kept at the same size. Initially the density is higher inside. We started the simulation by adding an initial random perturbation of the order 10^{-3} to the momentum density in the r direction. For all cases, the initial perturbation grew exponentially, and the equilibrium was completely destroyed. Fig. 3.1 shows the time sequence of the density for the case $R = 4$ in six gray-scale frames. The unstable mode first showed up as the characteristic ‘‘mushrooms’’ of interchanges; as the plasma continued to swirl around the chamber, the density was further mixed up, resulting in a slightly higher density on the outside. This behavior is typical, for all cases; only the time scales are different.

To quantify the deviation of the density profile from the equilibrium, we define the following function

$$W(t) \equiv \langle |1 - \rho/\rho_0| \rangle, \quad (3.37)$$

where the angular brackets denote an average taken over the whole volume at a given time t . Fig. 3.2 plots the time evolution of $W(t)$ for different R . The growth

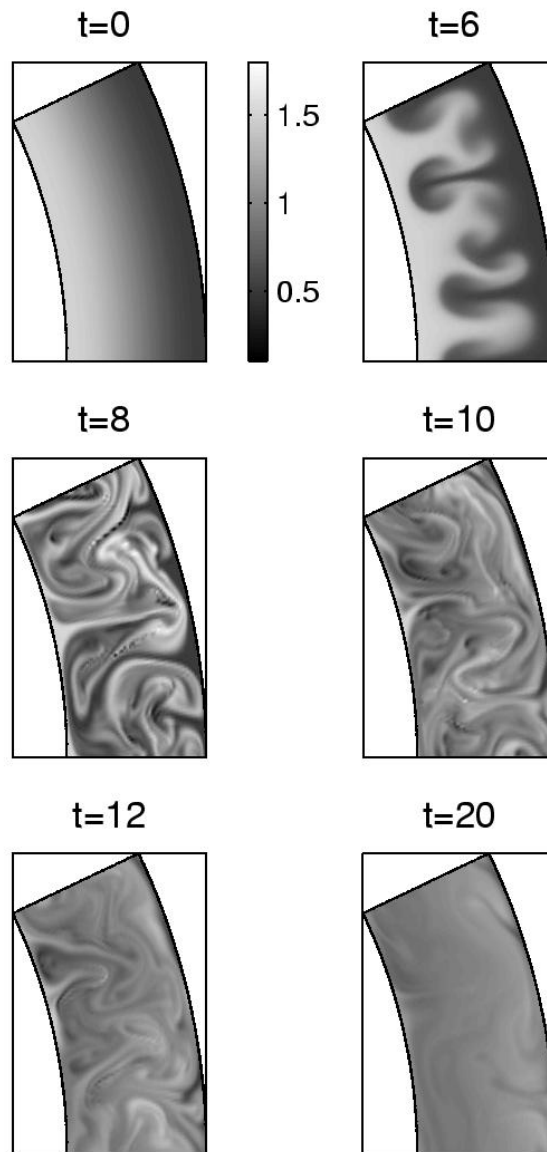


Figure 3.1: The time sequence of the density for the case with an aspect ratio $R=4$ in six gray-scale frames (velocity shear artificially suppressed).

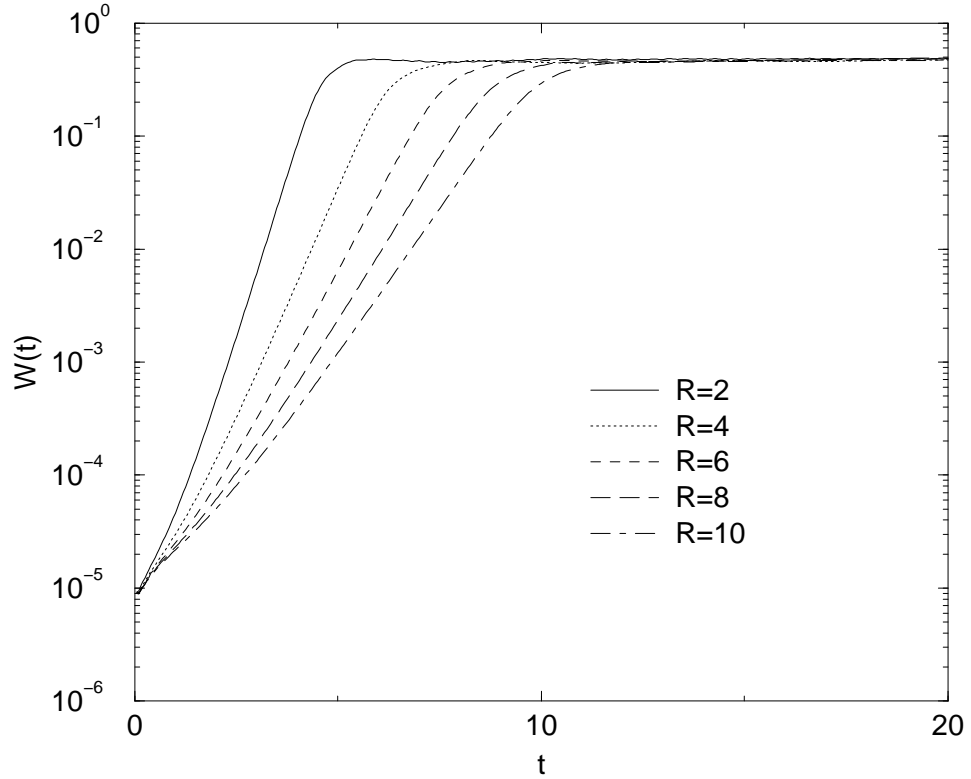


Figure 3.2: The time evolution of $W(t) \equiv \langle |1 - \rho/\rho_0| \rangle$ for $R = 2, 4, 6, 8,$ and 10 . $\eta = \mu = 0.002$. The velocity shear is artificially suppressed, while a “centrifugal force” is added. As the initial perturbation grew, $W(t)$ saturated to about 0.4 for all cases.

rate of the unstable mode can be estimated from the slope of the $W(t)$ curve in Fig. 3.2 (which is a semi-log plot) during linear growing regime. The growth rate scales as $1/\sqrt{R}$, as expected.

3.4.2 Cases with Velocity Shear

We next repeated the same numerical experiment, but with the velocity shear. As will be shown, the interchange mode was largely mitigated, though the stabilization

was incomplete. A series of simulations have been done to test the theoretical prediction.

Dependence on Aspect Ratio

First we test the aspect ratio dependence of the stabilization by shear flow. The theoretical prediction is that large aspect ratio systems should be more stable, essentially due to the fact that the mode growth rate without flow shear scales as $1/\sqrt{R}$. We repeated the same simulation for $R = 2, 4, 6, 8$, and 10 ; $\eta = \mu = 0.002$; but this time with the shear flow. Fig. 3.3 plots the time evolution of $W(t)$ for different R . The initial perturbation still grew, but now saturated to a much lower level compared to Fig. 3.2. For larger R the saturation level is lower, in agreement with the theoretical prediction. Fig. 3.4 plots the ϕ averaged density profile $\bar{\rho}$ (the overbar denotes averaging over ϕ) after the saturation of the interchange instability. The top left panel is the laminar density, shown for reference. The remaining five panels correspond to increasing R , with the laminar density overlaid (dashed). The large flattened portion in the middle for the case $R = 2$ is evident. As R becomes larger, the saturated density profile gets closer to the laminar profile. At $R = 10$, the laminar profile is almost completely retained. The localization of the disturbance near the middle is, presumably due to the fact that the flow shear is weakest there. This is consistent with previous simulations [21] and the analytic result of [6].

As a measurement of the turbulent flow, Fig. 3.5 plots the time evolution of the average radial kinetic energy, $\langle \rho u_r^2 / 2 \rangle$, where the average is taken over the volume. A noteworthy phenomenon is the “oscillatory” behavior, which could be understood as follows. In the beginning the instability led to turbulent flow and started mixing up the density. After the free energy was tapped, the density profile was flattened; the turbulence then lost its driving force and started to decay, followed by a “quiescent” period. As the system became quiescent, the particle source would try to “rebuild” the density profile, which made the system go unstable again. Since

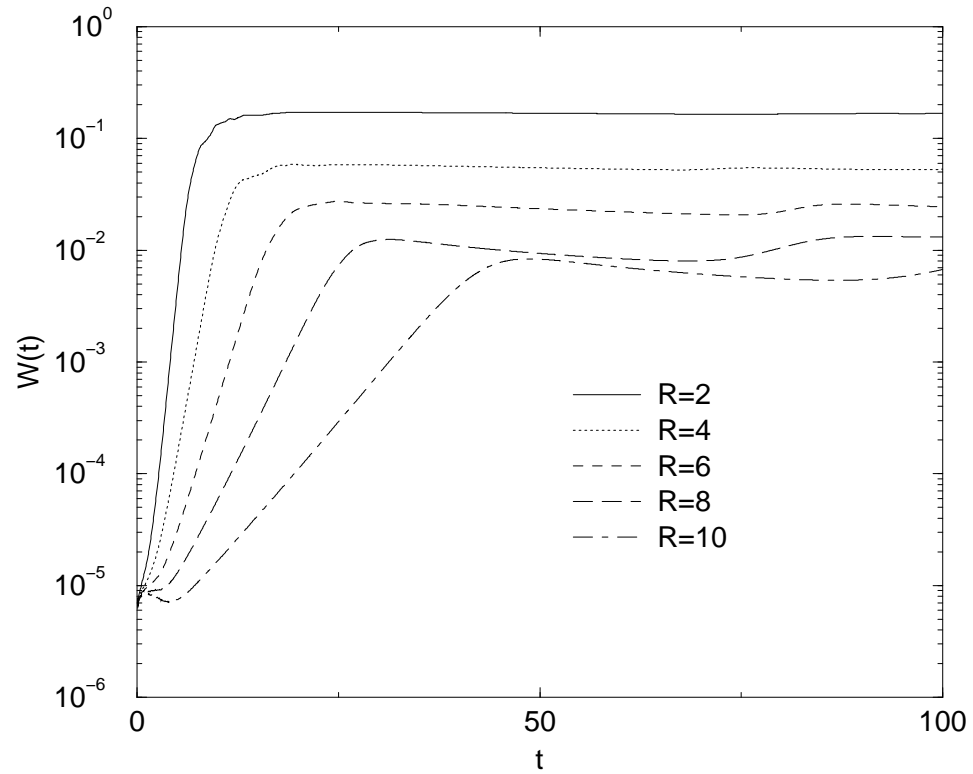


Figure 3.3: The time evolution of $W(t)$ for $R = 2, 4, 6, 8,$ and 10 . $\eta = \mu = 0.002$. As the initial perturbation grew, $W(t)$ saturated to different level for different R . Large aspect ratio systems appear more stable.

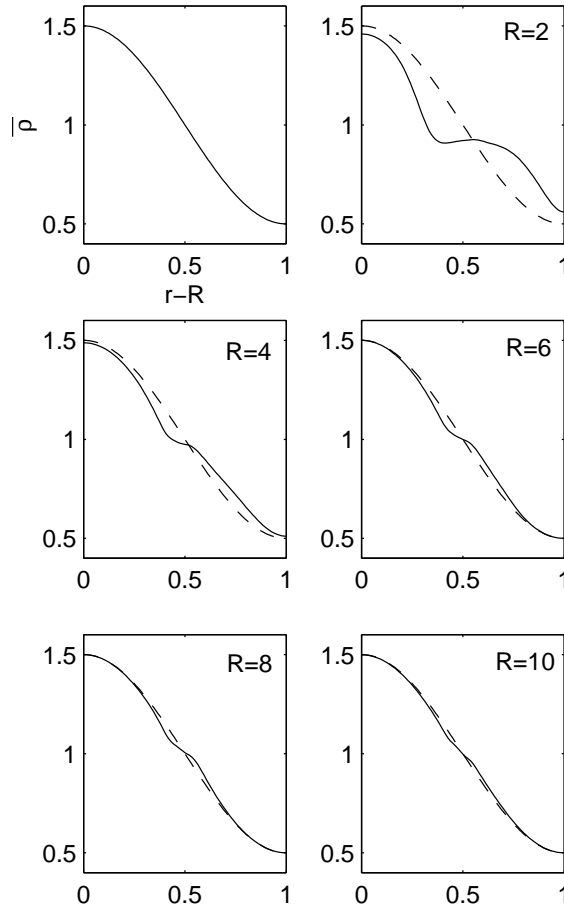


Figure 3.4: The saturated density profile (averaged over ϕ) after the onset of the interchange instability. The top left panel is the laminar density, shown for reference. The remaining five panels correspond to increasing R , with the laminar density overlaid (dashed). At $R = 2$, the density profile is heavily flattened at the middle (where the flow shear is weakest); however, at $R = 10$, the laminar profile is almost completely retained. $\eta = \mu = 0.002$ in these simulations.

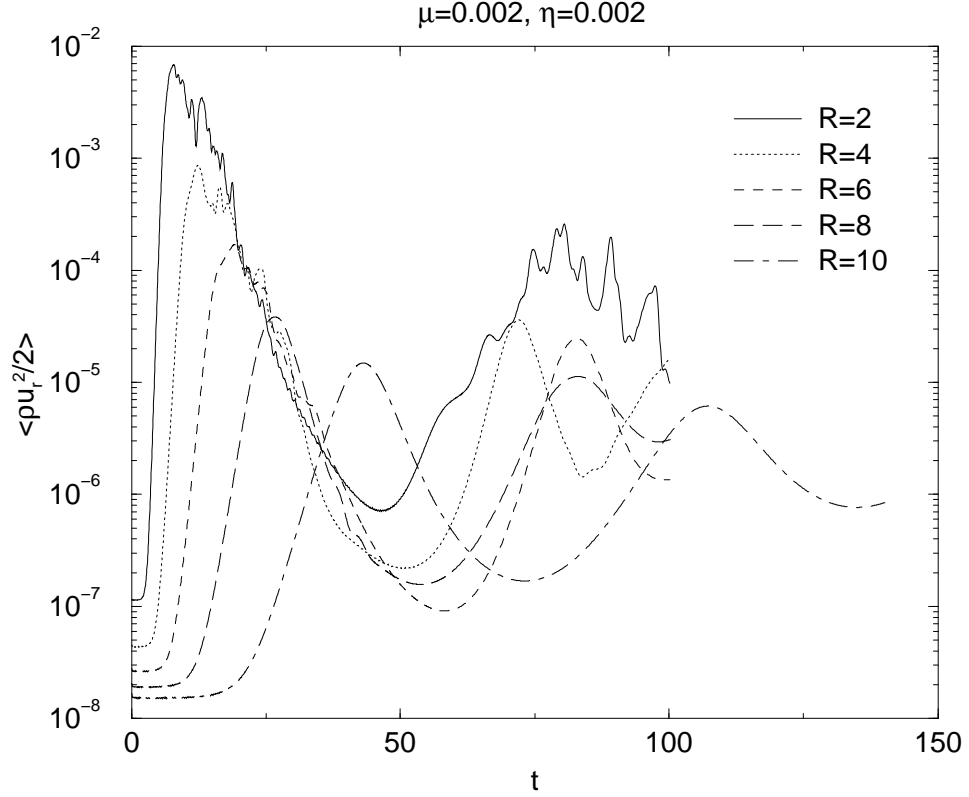


Figure 3.5: The time evolution of the averaged radial kinetic energy. Notice the oscillatory behavior. The difference at the “starting point” is due to the small laminar $u_r(\sim \eta)$, which is different for different cases.

the density profile never rebuilt to the original level before the instability destroyed it again, the subsequent peaks were always lower than the first one. Fig. 3.6 plots the time sequence of the density in six gray-scale frames, in which the above mentioned behavior is evident. It should be mentioned that although the interchanges do not destroy the whole density profile, the residual wobble could imply an enhanced cross-field transport in a real system [21].

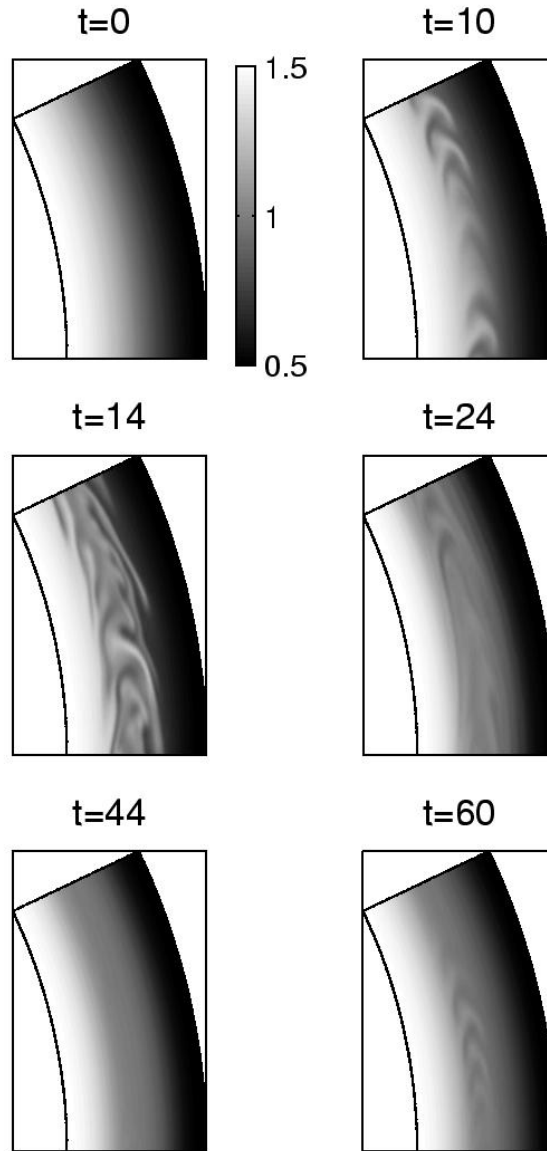


Figure 3.6: The time sequence of the density for the case $R=4$. Flute interchanges occurred but were localized at the middle ($t=10,14$). The interchanges flattened the density and started to decay ($t=24$), leading to a quiescent period ($t=44$). As the particle source tried to rebuild the density profile, the system went unstable again ($t=60$).

Dependence on Reynolds Number

To test the Reynolds number dependence of velocity shear stabilization, we simply re-did the same simulation with different dissipation coefficients. We fixed $R = 4$ throughout these simulations and varied η and μ . We wish to look at the effect of viscosity and resistivity separately. In one set of simulations, we kept $\mu = 0.0005$, and set η to three different values: 0.005, 0.0005, and 0.00005. In another set of simulations, we kept η but changed μ . Fig. 3.7 plots the saturated density profile (averaged along ϕ) for each case after the onset of interchanges, which clearly shows that the deviation from the laminar density profile gets larger as either μ or η gets smaller. Although both resistivity and viscosity seem to affect the stability in the same way, a more detailed look reveals some difference. Fig. 3.8 depicts the time evolution of the average radial kinetic energy, for both sets of simulations. All the cases (except the one with $\mu = 0.005$ and $\eta = 0.0005$) seem to have the same initial growth rate, yet the dissipation affects the subsequent decay of the disturbance. The plots show that the peak of the radial kinetic energy roughly scales as μ (the bottom), and is independent of η (the top). We observe that although the peak of $\langle \rho u_r^2 / 2 \rangle$ is roughly independent of η , smaller η causes a slower decay of the disturbance. This is presumably the cause of the large deviation from the laminar density profile. Viscosity, on the other hand, affects the turbulent flow more significantly, as it directly dissipates of the kinetic energy.

In summary, although the stability criterion (3.32) for interchange modes is essentially local, it nevertheless provides a fairly intuitive picture of the stabilizing mechanism. Its theoretical predictions are qualitatively borne out by direct simulations.

3.4.3 The “Weakest” Point

We observe that the residual wobbles were localized about the radius where $d\Omega/dr = 0$. Therefore, one is led to suggest that a system could be completely laminar

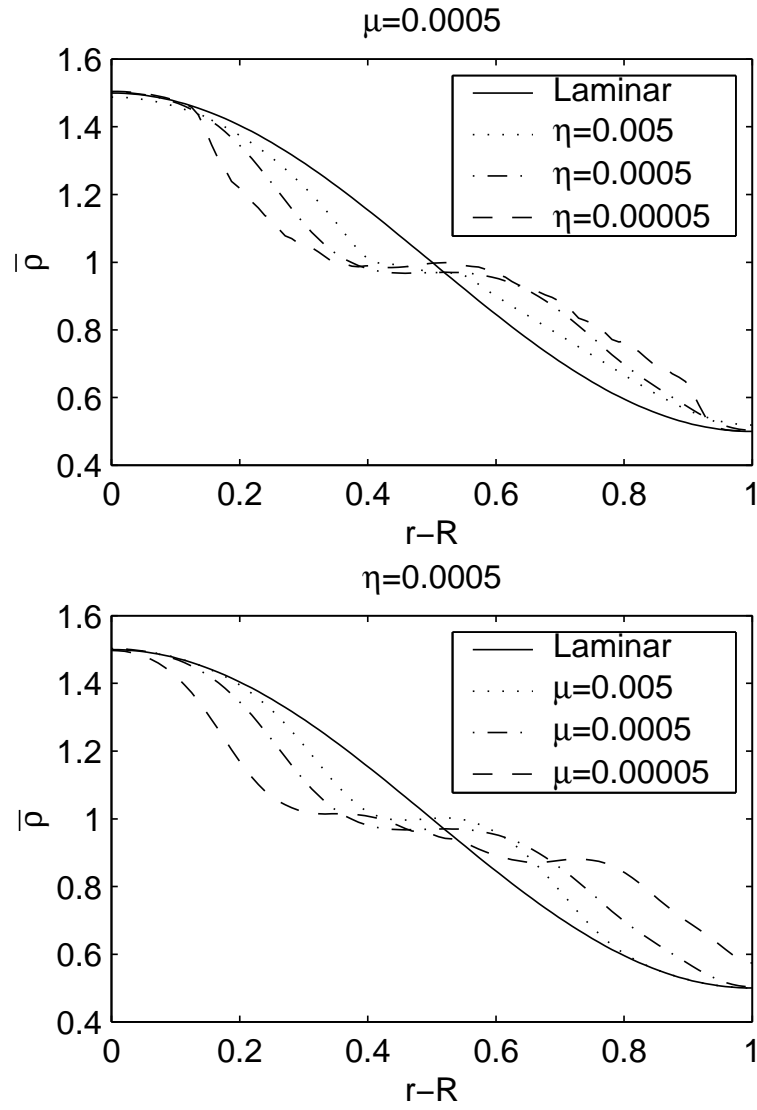


Figure 3.7: The saturated density profile (averaged along ϕ) after the interchanges. Top: various η with fixed μ . Bottom: various μ with fixed η . The dependence on dissipation is evident. As dissipation gets smaller, velocity shear stabilization becomes less efficient. $R = 4$ in all these simulations.

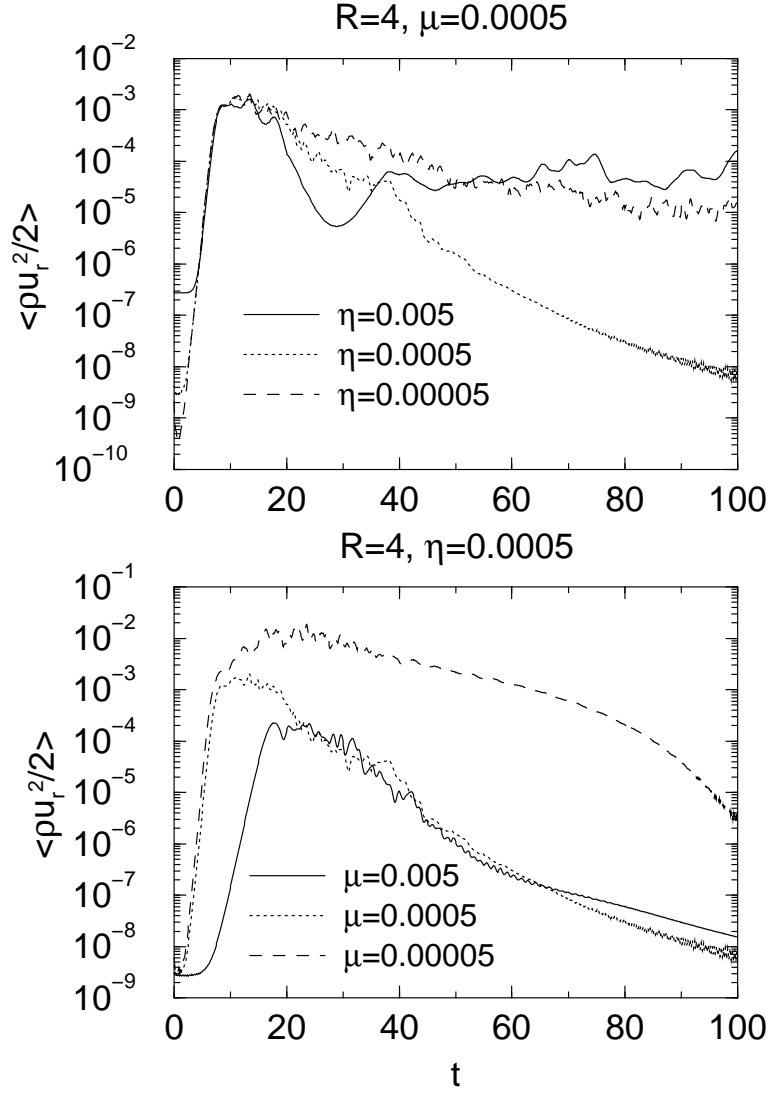


Figure 3.8: The time evolution of the averaged radial kinetic energy. Top: various η with fixed μ . Bottom: various μ with fixed η .

provided $d\rho_0/dr > 0$ at this “weakest” point. To test for this, we now changed the laminar density profile to

$$\rho_0(x) = 1 - C \cos(2\pi(x - Dx(1 - x))), \quad (3.38)$$

where the parameters C and D determine the amplitude and the position of the central density peak, respectively. Several different parameters have been tried. Here we only report the result of two cases: $C = 0.25$, $D = 0.5$ and $C = 0.25$, $D = -0.5$. We took $R = 4$, $L = 2$, and $\eta = \mu = 0.0005$. The amplitude $C = 0.25$ was chosen so that the Rayleigh’s inflection point criterion is not violated (to be discussed in more detail later). Both cases have destabilizing stratification somewhere, hence both are unstable to the “no-shear” test. However, the former has a stabilizing stratification at the weakest point, while the latter has a destabilizing one. When we ran both cases with flow shear, the former is completely stable, while unstable modes developed in the latter, resulting in a flattop of the density profile. This is clearly shown in Fig. 3.9, where we plot the laminar density profile of the two cases, with the saturated density profile of the unstable case overlaid. Therefore, we conclude that it is highly desirable to have a stabilizing stratification at the weakest point. By judiciously placing particle sources we presumably have some control over that.

3.5 Kelvin–Helmholtz Instability

It is well-known that flow shear could drive the Kelvin–Helmholtz instability.[19] For the Dean flow system, one can prove that in the limit $R \rightarrow \infty$, the following “generalized” Rayleigh’s inflection point theorem holds, namely

$$\frac{d}{dr} \left(\frac{\rho}{r} \frac{d}{dr} (r^2 \Omega) \right) \neq 0 \quad (3.39)$$

is a sufficient condition for ideal stability [32]. For finite R systems one can not expect the same condition to hold. An immediate counterexample is that, the

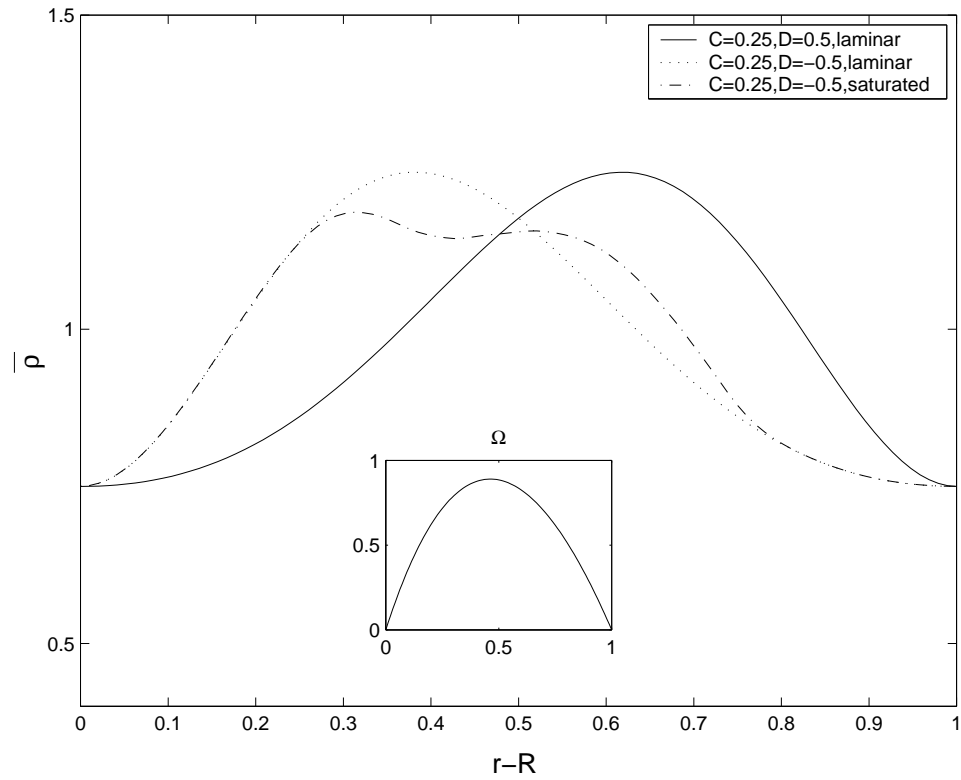


Figure 3.9: The laminar density profile of the two cases, one with a stabilizing stratification at the weakest point (solid line), the other with a destabilizing stratification (dotted line). Unstable modes developed in the latter, resulting in a flattop of the density profile (dash-dot line). The inset shows the laminar angular frequency of the flow for reference.

cases in Sec. 3.4 all satisfy the Rayleigh’s criterion, yet all of them are unstable. Nonetheless one may still expect the Rayleigh’s criterion to be a somewhat useful indicator for long wavelength modes. One should also bear in mind that even in the limit $R \rightarrow \infty$, violation of Rayleigh’s criterion does not always imply instabilities.

To demonstrate the utility of Rayleigh’s criterion, we report the result of two simulations. Both have density profiles of the form of (3.38); one with $C = 0.5$, $D = 0.5$ and the other with $C = 0.5$, $D = -0.5$. We took $R = 4$, $L = 2$, $\eta = \mu = 0.002$. Both cases violate Rayleigh’s criterion; in addition, the latter has a destabilizing density stratification at the weakest point. Now we see a different kind of unstable behavior. Fig. 3.10 shows the time sequence of the former case in six gray-scale frames. The characteristic Kelvin cat’s eye of the Kelvin–Helmholtz instability are clearly visible. Fig. 3.11 shows the time sequence of the latter one. Since the density stratification in this case is destabilizing at the weakest point, the interchanges set in at first, followed by a Kelvin–Helmholtz type of behavior. Taking a look at the time evolution of the average radial kinetic energy (Fig. 3.12) reveals more about the difference between the two cases. After the initial, violent stage, both cases settled down to a somewhat quiescent new state. However, we observed that in the latter case, the average radial kinetic energy fluctuated about 10^{-5} , due to the residual wobbles about the weakest point, in a manner described in Sec. 3.4. On the other hand, the former case enjoyed a long period (~ 100 sound times) of a nearly stable state, with $\langle \rho u_r^2/2 \rangle < 10^{-7}$. At $t \simeq 170$, the system started going unstable again, and $\langle \rho u_r^2/2 \rangle$ finally settled to about 10^{-4} . To elaborate, in Fig. 3.13 we plot $\bar{\rho}$, $((\bar{\rho}/r)(r^2\bar{\Omega})')'$, and $\overline{\rho u_r^2/2}$ at four representative times. At $t = 0$, $((\bar{\rho}/r)(r^2\bar{\Omega})')'$ is greater than zero in a region around $r = R + 0.9$. After the free energy was released, at $t = 100$, $((\bar{\rho}/r)(r^2\bar{\Omega})')'$ is less than zero everywhere. At this stage the system is very stable, as one can see from the very small radial kinetic energy. However, as the particle source rebuilt the density profile, $((\bar{\rho}/r)(r^2\bar{\Omega})')'$ about the point $r = R + 0.8$ was again approaching zero at $t = 175$. It was about

this time unstable modes started to grow again. Finally, after the unstable modes saturated, at $t = 250$, the density profile was about “marginal” to the Rayleigh’s criterion. We also notice that at this stage the radial convection was “global” instead of being localized at some small region (which was the case for the residual wobbles of interchanges). Compared to the localized residual wobbles, this global radial flow could be more harmful to the cross-field heat transport. To assess that we have to use a nonisothermal equation of state, which is beyond the scope of the present study.

3.6 Other Issues

3.6.1 Hysteresis

In all the simulations mentioned above, we first calculated the 1D equilibrium, seeding it with a 2D random noise as the starting point for the 2D stability test. We then looked for the saturated state after the onset of instabilities. This approach, rather than starting from some nonequilibrium 2D state, saves us some time since the density adjustment takes place on a resistive time scale, which is usually long. However, this does not preclude the possibility that the system could run into violent turbulence and get “clamped” somewhere during the formation. To test for this, we reran the case $R = 2$, $\eta = \mu = 0.002$ in 2D with the initial density and the magnetic field both flat (both were calculated from the equilibrium we expected to achieve, since our particle source conserves total mass and the perfect conducting boundary condition conserves total magnetic flux). The initial flow was set to zero, with some random noise added. If there had been any hysteresis, the final state would have been qualitatively different from what we reported previously. This was found not to be the case. We therefore concluded that there was no hysteresis.

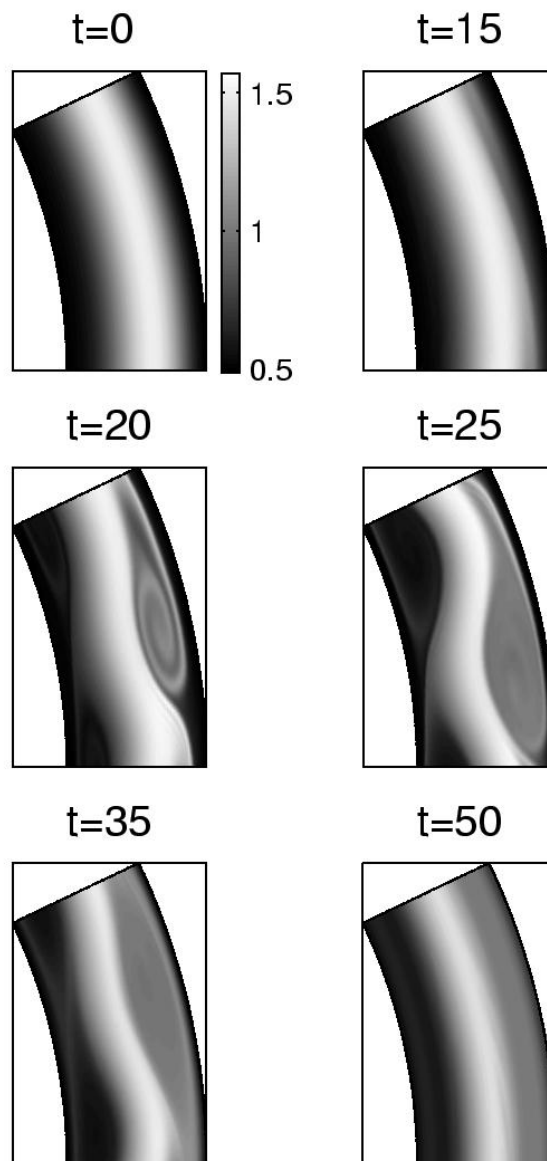


Figure 3.10: The time sequence for the case $C = 0.5$, $D = 0.5$. The characteristic Kelvin cat's eyes showed up as a result of the Kelvin–Helmholtz instability. After the system released the free energy, it settled down to a new, quiescent state.

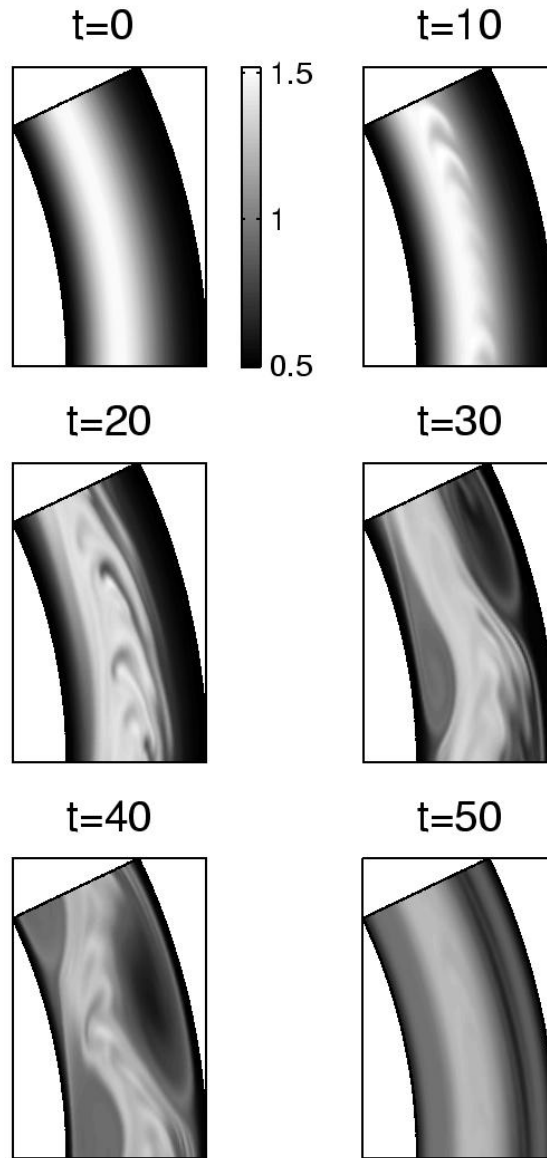


Figure 3.11: The time sequence for the case $C = 0.5$, $D = -0.5$. Because of the destabilizing stratification at the weakest point, the interchanges set in at first ($t=10$). Later on, the Kelvin–Helmholtz type of instability started to grow ($t=30$). After the free energy released, the system settled down to a new state, with some residual wobbles at the center.

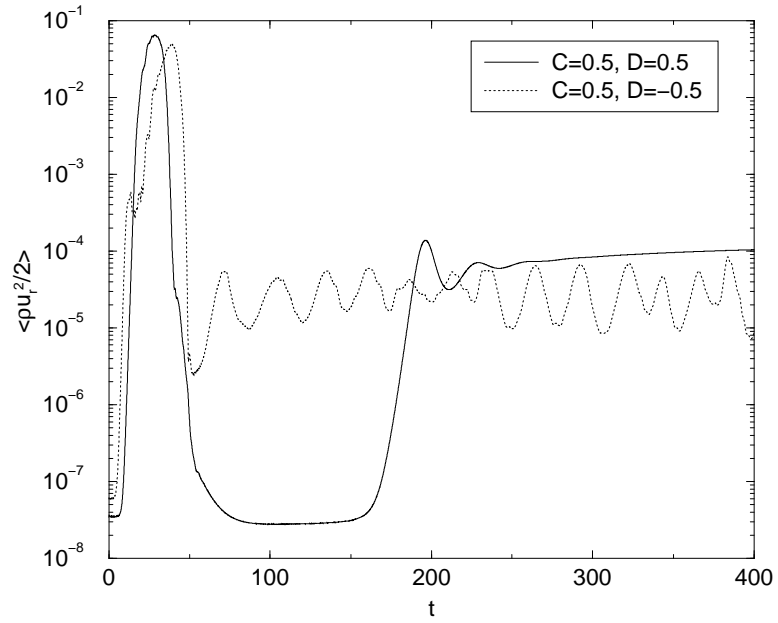


Figure 3.12: The time evolution of $\langle \rho u_r^2 / 2 \rangle$. The case $C = 0.5$, $D = -0.5$ has a destabilizing stratification at the weakest point. After the free energy was released, some residual wobbles remained around the weakest point. Those wobbles correspond to the oscillatory $\langle \rho u_r^2 / 2 \rangle$. The case $C = 0.5$, $D = 0.5$, on the other hand, enjoyed a long period of stable stage after releasing its free energy, until a sudden growth of unstable modes at $t \sim 170$.

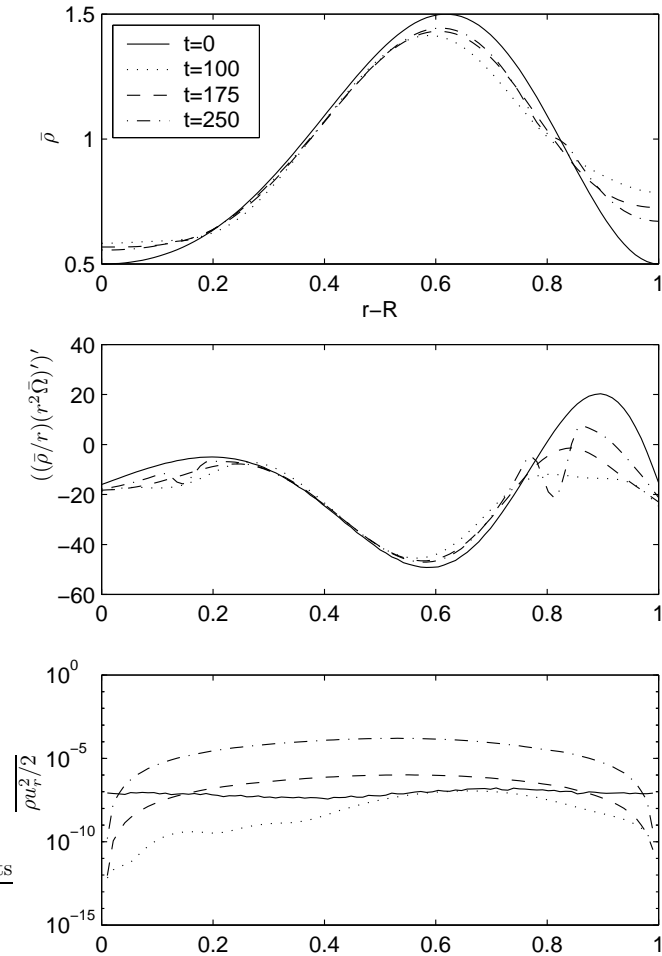


Figure 3.13: The ϕ averaged density, Rayleigh's criterion, and radial kinetic energy profile, for the case $C = 0.5$, $D = 0.5$, at four representative times. Notice that as the Rayleigh's criterion approached zero at $t = 175$, unstable modes started to grow. Also notice the global nature of the saturated axial flow, at $t = 250$. This global flow could cause a much more enhanced cross-field transport than localized wobbles could do.

3.6.2 Asymmetric Source

It is well-known that asymmetric sources drive convection cells. For a system close to marginal stability, the driven convection could be very large [58]. Thus far our derivation and simulation assume axisymmetric particle sources. The question how an asymmetric source may affect the result is relevant, since an axisymmetric source could be more difficult and costly to realize in practice. If the particle source is fixed in the laboratory frame, one may naturally suggest that the fast rotation could smear out the asymmetric source and effectively make it “quasi”-symmetric. Furthermore, since velocity shear is effective in tearing apart the convection caused by the interchange mode, the same effect may apply to the asymmetric source driven convection. To test for this, we re-did several simulations with asymmetric source by replacing $S(r) \rightarrow S(r)(1 + 0.5 \cos(4\pi\phi/\phi_0))$. For those completely laminar cases, the asymmetric source caused a small fluctuation of u_r along the ϕ direction. The fluctuation in u_r was of the order of the laminar u_r ; therefore, the asymmetry did not seem to significantly enhance the cross-field transport. The density profile remained intact as well. On the other hand, for those wobbling cases, the asymmetric source introduced no discernible effect. We conclude that an asymmetric source may not cause problems. If this is indeed the case, the implementation could be easier.

3.6.3 Generalized Ohm’s Law and Thermoelectric Effect

In this study, we use the Ohm’s law in its simplest form. To better model the real system the generalized Ohm’s law should be taken into account, and the thermoelectric effect should also be considered [11, 59, 34]. Including this physics will certainly change the detail of the slowly diffusing equilibrium described in Sec. 3.2. However, we observe that none of this extra physics can provide a unidirectional toroidal current drive. Since such a toroidal current is required to balance the centrifugal force, including this physics does not seem to change the main conclusion of this Chapter, namely that particle sources are necessary to maintain a centrifugally confined

steady state, and that particle sources may be utilized to control the density profile, therefore affect the stability.

3.7 Summary and Conclusion

In this Chapter we studied the equilibrium and the stability of a slowly diffusing rotating plasma with particle sources. We summarize our findings as follows:

(1) Particle sources (and sinks) are necessary for a steady state of centrifugally confined plasmas. The density profile of the steady state depends on the placement of particle sources.

(2) Such a slowly diffusing steady state is realizable only when it is stable. Our simulation shows velocity shear stabilization of interchanges, and the steady state is largely maintained. The velocity shear stabilization may not be complete, noticeably around the “weakest point” where $\Omega' = 0$. In those cases the interchanges flatten the density profile about the weakest point, therefore bring the system close to marginal stability. Some residual wobbles still remain; however, they are well localized and the “transport barrier” near the walls is still maintained. Furthermore, by adjusting the particle source we could have a stabilizing stratification about the weakest point, therefore achieve a completely stable equilibrium.

(3) The Kelvin–Helmholtz instability is also studied. When the generalized Rayleigh’s criterion is violated, the KH modes could occur. The KH instability again will not destroy the steady state completely; it rather brings the system close to marginal stability, with some residual convection.

We are now in a position to address the question why the system of Chapter 2 was so stable. In that case both the density and the pressure stratification were stabilizing at the weakest point (in a rotating mirror both the density and the pressure could drive interchanges). It will then be interesting to see how the residual wobbles may affect the cross-field transport in a centrifugally confined plasma, if one can produce a unfavorable profile by “injudiciously” placing the source.

In conclusion, introducing a shear flow complicates the stability of the system, yet this complication also means more flexibility. In particular, the density profile plays a significant role in the stability of a rotating system, while it is completely irrelevant in a static system. Certainly a strong velocity shear is not always stabilizing. However, since the stability is profile dependent, by adjusting various profiles via various sources we may have some control over it.

Chapter 4

Interchanges in Low Density Plasmas — with Applications to Line-Tied Slab and Centrifugally Confined Plasma

4.1 Introduction

In the usual derivation of the magnetohydrodynamic (MHD) equations, it is assumed that the electric force $\mathbf{E}\nabla \cdot \mathbf{E}/4\pi$ is negligible compared to the inertial forces $\rho\mathbf{u} \cdot \nabla\mathbf{u}$, and the displacement current is omitted [24]. These assumptions are justified by estimating these terms as

$$\frac{|\mathbf{E}\nabla \cdot \mathbf{E}/4\pi|}{|\rho\mathbf{u} \cdot \nabla\mathbf{u}|} \sim \frac{E^2/L}{\rho u^2/L} \sim \frac{B^2}{\rho c^2} \sim \frac{V_A^2}{c^2}, \quad (4.1)$$

$$\frac{|\partial_t \mathbf{E}/c|}{|\nabla \times \mathbf{B}|} \sim \frac{E/c\tau}{B/L} \sim \frac{uL/\tau}{c^2} \sim \frac{uV}{c^2}, \quad (4.2)$$

where L and τ are the characteristic length and time scales, c the speed of light, $V_A = B/\sqrt{4\pi\rho}$ the Alfvén speed, and V a characteristic speed, e.g., the sound speed $C_S = \sqrt{\gamma p/\rho}$, Alfvén speed V_A , or flow speed u ; $E \sim uB/c$ is assumed. In most plasmas of interest, the speed of light is the fastest, and the approximation may be justified. However, in a low density plasma with $V_A \gtrsim c$, the approximations are no longer valid. Including the electric force and the displacement current leads to the full momentum equation (see below in (4.4)), where $\mathbf{E} \times \mathbf{B}/4\pi c$ is the momentum density of the electromagnetic (EM) field [39]. Therefore, another way to justify the MHD approximation is to compare the momentum density of the plasma with that of the

EM field: $\rho \mathbf{u} : \mathbf{E} \times \mathbf{B} / 4\pi c \sim 1 : V_A^2 / c^2$. The usual MHD approximation amounts to neglecting the EM field momentum, as well as other terms of the same size, compared to the plasma momentum. Apparently this approximation is inappropriate when $V_A \gtrsim c$.

The present study is motivated by centrifugally confined plasma, an alternative approach to magnetic confinement fusion which utilizes the centrifugal force of a rapidly rotating plasma of magnetic mirror geometry to augment confinement along the magnetic field [23, 31]. For a typical hydrogen plasma with $B = 5 \times 10^4$ gauss and $n = 10^{14} \text{cm}^{-3}$, $V_A \simeq 10^9 \text{cm/s}$. In a centrifugally confined plasma, the plasma density could drop by a factor of more than a thousand along the field toward the mirror throats. That means that the Alfvén speed could be comparable or even exceed the speed of light, and the usual MHD description becomes inappropriate.

The predominant MHD instability in centrifugally confined plasmas is the flute interchange. Therefore, the interchange instability of low density plasmas need revisiting. This Chapter addresses this and is organized as follows: In Sec. 4.2 we set up the governing equations which are applicable for low density plasmas. In Sec. 4.3 we first apply the equations to a relatively simpler setting, namely interchanges in a line-tied slab geometry with gravity. After acquiring a general understanding from that, we then apply the equations to centrifugally confined plasmas in Sec. 4.4. In both Secs. we first derive a set of reduced equations appropriate for the problem, then linearize the reduced equations for small perturbations to study the stability. We summarize and conclude in Sec. 4.5.

4.2 Basic Equations

The governing fluid equations applicable for low density plasma with $V_A \sim c$ are:

$$\frac{\partial \rho}{\partial t} + \nabla \cdot (\rho \mathbf{u}) = 0, \quad (4.3)$$

$$\rho \frac{\partial \mathbf{u}}{\partial t} + \rho \mathbf{u} \cdot \nabla \mathbf{u} + \frac{1}{4\pi c} \frac{\partial(\mathbf{E} \times \mathbf{B})}{\partial t} = -\nabla p + \frac{1}{4\pi}(\nabla \cdot \mathbf{E})\mathbf{E} + \frac{1}{4\pi}(\nabla \times \mathbf{E}) \times \mathbf{E} + \frac{1}{4\pi}(\nabla \times \mathbf{B}) \times \mathbf{B} + \rho \mathbf{g}, \quad (4.4)$$

$$\frac{\partial p}{\partial t} + \mathbf{u} \cdot \nabla p + \gamma p \nabla \cdot \mathbf{u} = 0, \quad (4.5)$$

$$\frac{\partial \mathbf{B}}{\partial t} = -c \nabla \times \mathbf{E}, \quad (4.6)$$

$$\nabla \cdot \mathbf{B} = 0, \quad (4.7)$$

$$\mathbf{E} = -\frac{\mathbf{u} \times \mathbf{B}}{c}, \quad (4.8)$$

$$\nabla \times \mathbf{B} = \frac{1}{c} \frac{\partial \mathbf{E}}{\partial t} + \frac{4\pi}{c} \mathbf{J}. \quad (4.9)$$

Standard notation is used. Eq. (4.3) is the continuity equation; Eq. (4.4) is the full momentum equation without omitting any term [39], with a gravity \mathbf{g} included; Eq. (4.5) is the adiabatic evolution of pressure; Eq. (4.6) is Faraday's law; Eq. (4.7) is the solenoidal constraint on the magnetic field; Eq. (4.8) is the perfectly conducting approximation of ideal MHD; Eq. (4.9) is Ampère's law with displacement current. Notice that Eqs (4.3)–(4.8) form a complete set; the Ampère's law (4.9) is shown only as a reference.

4.3 Flute Interchanges in a Line-Tied Slab

Consider a simple system that includes line-tying, as follows. A strong, nearly uniform magnetic field along the z -axis is embedded in a tenuous plasma. The plasma is confined between two perfectly conducting plates which are perpendicular to the z -axis at $z = 0, L_z$, and infinite in extent in both x and y directions. There is a uniform external gravity pointing in the $-\hat{x}$ direction.

4.3.1 Reduced Equations

We begin by deriving reduced equations for this system. We assume that the perpendicular length scale L_\perp is much smaller than L_z , and that the dominant magnetic

field is along the z direction, i.e., $B_\perp \ll B_z$. The system is low- β since we are considering low density plasmas. We further assume that $u_z \ll u_\perp$ since our primary interests are the interchange modes, which are perpendicular to the magnetic field. Based on these assumptions, we introduce the following ordering [60] in terms of a small quantity ϵ :

$$\frac{L_\perp}{L_z} \sim \frac{B_\perp}{B_z} \sim \frac{u_z}{u_\perp} \sim \epsilon, \quad (4.10)$$

$$p \sim \rho u^2 \sim \rho g L_\perp \sim B_\perp^2 \sim \epsilon^2 B_z. \quad (4.11)$$

From the ordering (4.10), we have

$$\partial_z \sim \epsilon \nabla_\perp. \quad (4.12)$$

Since we are interested in slow, sub-Alfvénic motions, we further assume:

$$L_\perp \partial_t \sim u_\perp \sim \epsilon V_{Az} \sim \epsilon c. \quad (4.13)$$

In the following derivation of reduced equations, we substitute the expansion $\mathbf{B} = \mathbf{B}_0 + \mathbf{B}_1 + \mathbf{B}_2 + \dots$, $\mathbf{u} = \mathbf{u}_0 + \mathbf{u}_1 + \mathbf{u}_2 + \dots$, wherein each term is smaller than the previous one by an order of ϵ , into equations (4.3)–(4.8), equating both sides of each equation, order by order, until we get a complete set of equations.

Assuming to the lowest order, $\mathbf{B}_0 = B_0 \hat{z}$ is a constant, uniform field, we can infer from the lowest significant order of equations (4.6) and (4.7) that $\nabla_\perp \cdot \mathbf{u}_{0\perp} = 0$ and $\nabla_\perp \cdot \mathbf{B}_{1\perp} = 0$. Therefore, $\mathbf{u}_{0\perp}$ and $\mathbf{B}_{1\perp}$ can be expressed in terms of a stream function ϕ and a flux function ψ :

$$\mathbf{u}_{0\perp} = \hat{z} \times \nabla_\perp \phi, \quad (4.14)$$

$$\mathbf{B}_{1\perp} = \hat{z} \times \nabla_\perp \psi. \quad (4.15)$$

The lowest order of Eq. (4.4) gives a trivial result $\nabla_\perp B_0^2 = 0$, whereas the $O(\epsilon)$ of Eq. (4.4) gives:

$$\nabla_\perp B_{1z} = 0. \quad (4.16)$$

Taking Eq. (4.4) to $O(\epsilon^2)$, using (4.14) and (4.15), we have:

$$\begin{aligned} \left(\rho + \frac{B_0^2}{4\pi c^2}\right) \partial_t \mathbf{u}_{0\perp} + \rho \mathbf{u}_{0\perp} \cdot \nabla_{\perp} \mathbf{u}_{0\perp} = \\ \frac{1}{4\pi} [-\nabla_{\perp}(B_0 B_{2z}) - \nabla_{\perp}^2 \psi \nabla_{\perp} \psi + B_0 \hat{z} \times \nabla_{\perp}(\partial_z \psi)] \\ - \nabla_{\perp} p + \frac{B_0^2}{4\pi c^2} \nabla_{\perp}^2 \phi \nabla_{\perp} \phi - \rho g \hat{x}. \end{aligned} \quad (4.17)$$

Notice that the z component of Eq. (4.17) yields the trivial identity, which proves the self-consistency of the ordering $u_z \sim \epsilon u_{\perp}$. We can eliminate p_0 and B_{2z} in (4.17) by applying an annihilator $\hat{z} \times \nabla_{\perp}$ on (4.17); after some algebra:

$$\nabla_{\perp} \cdot \left[\left(\rho + \frac{B_0^2}{4\pi c^2} \right) (\partial_t + \mathbf{u}_{0\perp} \cdot \nabla_{\perp}) \nabla_{\perp} \phi \right] = \frac{1}{4\pi} (B_0 \partial_z + \mathbf{B}_{1\perp} \cdot \nabla_{\perp}) \nabla_{\perp}^2 \psi + g \partial_y \rho. \quad (4.18)$$

Taking Eq. (4.6) to $O(\epsilon)$, we have:

$$\partial_t \mathbf{B}_1 = \nabla_{\perp} \times (\mathbf{u}_{0\perp} \times \mathbf{B}_1) - B_0 (\nabla_{\perp} \cdot \mathbf{u}_1) \hat{z} + B_0 \partial_z \mathbf{u}_{0\perp}. \quad (4.19)$$

By applying $\hat{z} \times$ on (4.19) to eliminate \mathbf{u}_1 , we have

$$\nabla_{\perp} (\partial_t \psi + \mathbf{u}_{0\perp} \cdot \nabla_{\perp} \psi) = \nabla_{\perp} (B_0 \partial_z \phi), \quad (4.20)$$

which can be integrated to yield

$$\partial_t \psi + \mathbf{u}_{0\perp} \cdot \nabla_{\perp} \psi = B_0 \partial_z \phi + f(z, t), \quad (4.21)$$

where $f(z, t)$ can be set to zero without affecting the physical quantity \mathbf{B}_1 . Thus far we have obtained two equations (4.18) and (4.21) with three variables ρ , ϕ , and ψ ; we need one more equation to close the set. This is given by the lowest order of Eq. (4.3):

$$\partial_t \rho + \mathbf{u}_{0\perp} \cdot \nabla_{\perp} \rho = 0. \quad (4.22)$$

Eq. (4.22) together with Eqs. (4.18) and (4.21) constitute a complete set of equations for three variables ρ , ϕ , and ψ . Since only the lowest order of \mathbf{u} and the

first order \mathbf{B}_\perp appear in the final set of equations, we may drop the order index “0” and “1” in $\mathbf{u}_{0\perp}$ and $\mathbf{B}_{1\perp}$. With the definitions

$$\frac{d}{dt} \equiv \partial_t + \mathbf{u}_\perp \cdot \nabla_\perp \equiv \partial_t + (\hat{z} \times \nabla_\perp \phi) \cdot \nabla_\perp, \quad (4.23)$$

and

$$\mathbf{B} \cdot \nabla \equiv B_0 \partial_z + \mathbf{B}_\perp \cdot \nabla_\perp \equiv B_0 \partial_z + (\hat{z} \times \nabla_\perp \psi) \cdot \nabla_\perp, \quad (4.24)$$

we can now summarize the full set of reduced equations for low density slab plasmas in the following compact form:

$$\nabla_\perp \cdot \left[\left(\rho + \frac{B_0^2}{4\pi c^2} \right) \frac{d}{dt} \nabla_\perp \phi \right] = \frac{1}{4\pi} \mathbf{B} \cdot \nabla \nabla_\perp^2 \psi + g \partial_y \rho, \quad (4.25)$$

$$\frac{d\psi}{dt} = B_0 \partial_z \phi, \quad (4.26)$$

$$\frac{d\rho}{dt} = 0. \quad (4.27)$$

The only difference between this and usual set is that $(\rho + B_0^2/4\pi c^2)$ in the left hand side of (4.25) replaces ρ in the usual reduced equations. The EM field momentum effectively increases the inertia by a factor of $(1 + V_A^2/c^2)$.

4.3.2 Linear Stability

We now linearize equations (4.25), (4.26) and (4.27) about an equilibrium $\rho = \rho(x)$, $\phi = 0$ and $\psi = 0$. The linearized equations for small perturbations $\tilde{\rho}$, $\tilde{\phi}$ and $\tilde{\psi}$ are:

$$\frac{\partial}{\partial t} \nabla_\perp \cdot (\rho \nabla_\perp \tilde{\phi}) + \frac{B_0^2}{4\pi c^2} \frac{\partial}{\partial t} (\nabla_\perp^2 \tilde{\phi}) = \frac{B_0}{4\pi} \frac{\partial}{\partial z} \nabla_\perp^2 \tilde{\psi} + \frac{\partial \tilde{\rho}}{\partial y} g, \quad (4.28)$$

$$\frac{\partial \tilde{\psi}}{\partial t} = B_0 \frac{\partial \tilde{\phi}}{\partial z}, \quad (4.29)$$

$$\frac{\partial \tilde{\rho}}{\partial t} - \frac{\partial \tilde{\phi}}{\partial y} \frac{d\rho}{dx} = 0. \quad (4.30)$$

Eliminating $\tilde{\rho}$ and $\tilde{\psi}$ in equation (4.28) by equations (4.29) and (4.30), we obtain

$$\frac{\partial^2}{\partial t^2} \nabla_\perp \cdot (\rho \nabla_\perp \tilde{\phi}) + \frac{B_0^2}{4\pi c^2} \frac{\partial^2}{\partial t^2} (\nabla_\perp^2 \tilde{\phi}) = \frac{1}{4\pi} B_0^2 \frac{\partial^2}{\partial z^2} \nabla_\perp^2 \tilde{\phi} + \frac{\partial \rho}{\partial x} \frac{\partial^2 \tilde{\phi}}{\partial y^2} g. \quad (4.31)$$

The existence of perfect conducting plates imposes the boundary condition $\nabla_{\perp}\tilde{\phi} = 0$ at $z = 0, L_z$. If we assume an eikonal solution

$$\tilde{\phi} = \tilde{\phi}(x) \sin(k_z z) \exp(ik_y y - i\omega t), \quad (4.32)$$

then the boundary condition implies quantized $k_z = N\pi/L_z$, for all positive integer values of N . Since short transverse wavelength modes are the most unstable modes [24], we restrict ourselves to the short wavelength limit, i.e. $k_y \gg \partial_x$. Neglecting ∂_x in equation (4.31) compared with k_y , we obtain:

$$\omega^2 k_y^2 \left(\rho + \frac{B_0^2}{4\pi c^2} \right) \tilde{\phi} = \left(\frac{B_0^2 k_z^2}{4\pi} - \rho' g \right) k_y^2 \tilde{\phi}. \quad (4.33)$$

From Eq. (4.33) we immediately get the local dispersion relation for short wavelength modes:

$$\omega^2 = \frac{k_z^2 V_A^2 - g\rho'/\rho}{1 + V_A^2/c^2}. \quad (4.34)$$

In the limit $V_A \ll c$, the usual local dispersion relation is recovered. From the local dispersion relation (4.34) and quantized k_z , we can immediately obtain the stability condition:

$$\frac{V_A^2 \pi^2}{L_z^2} > -g \frac{\rho'}{\rho}, \quad (4.35)$$

which, roughly speaking, means that the Alfvén frequency must be greater than the growth rate of gravity-induced flute interchange modes for the magnetic tension to stabilize the interchange instability. Notice that the stability criterion (4.35) does not depend on the parameter V_A^2/c^2 , but the dispersion relation (4.34) does. For a low density plasma the EM field momentum effectively increases the inertia, yet the driving force of interchanges – the gravity – only acts on the plasma. As a result, the growth rate is reduced by a factor of $\sqrt{1 + V_A^2/c^2}$.

4.4 Centrifugally Confined Plasmas

As mentioned in the Introduction, the main motivation for this study comes from centrifugally confined plasmas. Previously the MHD stability of centrifugally con-

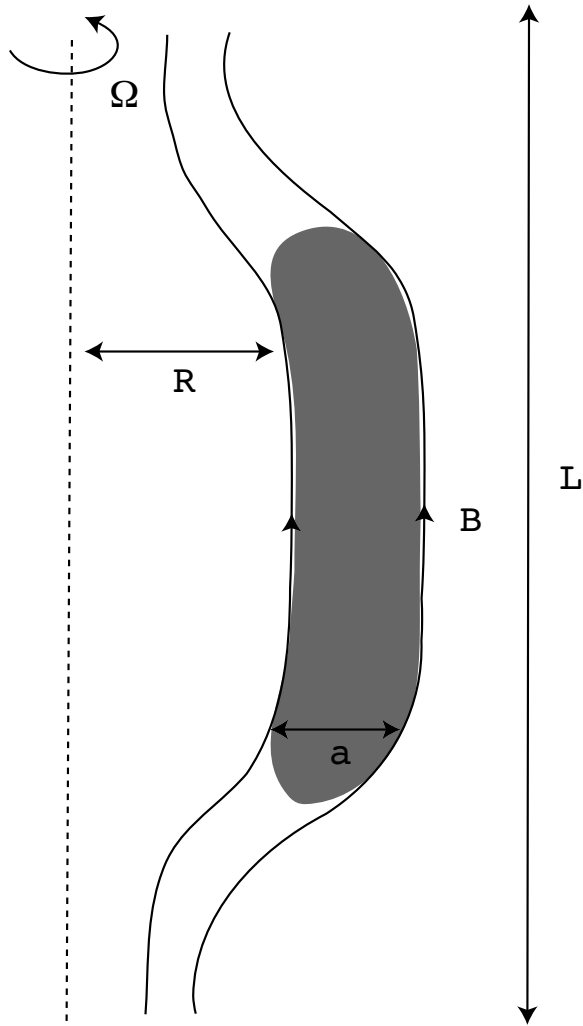


Figure 4.1: A sketch of a centrifugally confined plasma.

finer plasmas has been studied analytically using a straight-field Dean flow model [32], where the effect of magnetic curvature is modeled with an outwardly pointing effective gravity acting on the pressure. In this section we will extend the calculation of Ref. [32] to include a curved magnetic field explicitly, and take into account the effect of possible low density plasmas at both ends. It seems reasonable that the dominant contribution to the possible flute instability comes from the center where both the density and the pressure are high; hence, we expect that taking into account of the low density plasma would not change the basic result. Moreover, our experience of Sec. 4.3 tells us that low density plasmas are more stable; thus, taking into account of the low density effect should make the system somewhat more stable. The following calculation confirms our intuition. Figure 4.1 shows a sketch of a centrifugally confined plasma, where we denote the radial size of the plasma as a , the major radius as R , and the elongation as L . For simplicity, we assume periodicity along the axial direction in the following analysis.

4.4.1 Reduced Equations

We limit ourselves to a low- β system, therefore we assume the following ordering:

$$C_S \sim u \sim \epsilon V_A \sim \epsilon c; \quad (4.36)$$

and we are only interested in slow, sub-Alfvénic time scales, therefore:

$$\partial_t \sim \mathbf{u} \cdot \nabla. \quad (4.37)$$

Notice that although $V_A \sim c$ is not always true throughout the whole system, we have to make this optimal ordering to take into account the possible low density parts. We follow the same method of Sec. 4.3, by substituting expansions $\mathbf{B} = \mathbf{B}_0 + \mathbf{B}_1 + \mathbf{B}_2 \dots$ and $\mathbf{u} = \mathbf{u}_0 + \mathbf{u}_1 + \mathbf{u}_2 + \dots$ into the governing equations. Since most of the magnetic field is provided by external coils, we thus assume \mathbf{B}_0 to be the external field, which is independent of time. For simplicity, we also assume the external field to be purely

poloidal. Therefore, \mathbf{B}_0 can be expressed by a flux function ψ :

$$\mathbf{B}_0 = -\frac{1}{r}\hat{\zeta} \times \nabla\psi, \quad (4.38)$$

where r and ζ denote the radius and angular coordinates of the usual cylindrical coordinate system (r, ζ, z) .

The assumption of \mathbf{B}_0 as the external field implies $\nabla \times \mathbf{B}_0 = 0$ within the system, in accordance with the leading order of Eq. (4.4), which simply yields the trivial identity. From $\nabla \times \mathbf{B}_0 = 0$, the flux function ψ satisfies

$$\nabla \cdot \left(\frac{\nabla\psi}{r^2} \right) = 0. \quad (4.39)$$

It can be inferred from $\partial_t \mathbf{B}_0 = 0$ and Eq. (4.6) that to the lowest order, $\nabla \times \mathbf{E}_0 = 0$. Hence the lowest order \mathbf{E}_0 is electrostatic, and can be expressed by an electrostatic potential ϕ :

$$\mathbf{E}_0 = -\frac{1}{c}\nabla\phi. \quad (4.40)$$

Using the definition (4.40) in Eq. (4.8), to the lowest order, gives $\nabla\phi = \mathbf{u}_0 \times \mathbf{B}_0$. That implies

$$\mathbf{B}_0 \cdot \nabla\phi = 0, \quad (4.41)$$

and

$$\mathbf{u}_0 = u_{\parallel}\hat{b} + \frac{\hat{b} \times \nabla\phi}{B_0}, \quad (4.42)$$

where $\hat{b} \equiv \mathbf{B}_0/B_0$ is the unit vector along the magnetic field.

To $O(\epsilon)$ of Eq. (4.4), we have $\mathbf{B}_0 \times (\nabla \times \mathbf{B}_1) = 0$, which implies $\nabla \times \mathbf{B}_1 = \chi \mathbf{B}_0$, with some function χ . Taking the divergence of both sides, we get $\mathbf{B}_0 \cdot \nabla\chi = 0$; i.e., χ is a constant along a field line. Recalling that a centrifugal confinement device has an ‘‘open’’ field line configuration, it is reasonable to assume that $\mathbf{J} \cdot \mathbf{B} = 0$ at both mirror throats of the device, to all orders; otherwise there will be a charge leakage along the field. Since $(\mathbf{J} \cdot \mathbf{B})_1 = (4\pi/c)\mathbf{B}_0 \cdot \nabla \times \mathbf{B}_1 = (4\pi/c)\chi B_0^2 = 0$ at both ends, χ is zero there. As we have shown that χ is a constant along a field line, χ must be zero throughout the whole system, which implies $\nabla \times \mathbf{B}_1 = 0$.

Now we take Eq. (4.4) to $O(\epsilon^2)$, which yields

$$\rho \frac{\partial \mathbf{u}_0}{\partial t} + \rho \mathbf{u}_0 \cdot \nabla \mathbf{u}_0 + \frac{\mathbf{B}_0 \times \partial_t \nabla \phi}{4\pi c^2} = -\nabla p + \frac{1}{4\pi c^2} \nabla^2 \phi \nabla \phi + \frac{1}{4\pi} (\nabla \times \mathbf{B}_2) \times \mathbf{B}_0. \quad (4.43)$$

Again, we obtain two equations by acting on Eq. (4.43) by $\mathbf{B}_0 \cdot$ and $\mathbf{B}_0 \times$. The former simply gives

$$\mathbf{B}_0 \cdot (\rho \partial_t \mathbf{u}_0 + \rho \mathbf{u}_0 \cdot \nabla \mathbf{u}_0 + \nabla p) = 0, \quad (4.44)$$

and the latter gives

$$\frac{1}{4\pi} (\nabla \times \mathbf{B}_2)_\perp = \frac{\hat{b}}{B_0} \times \left(\rho \partial_t \mathbf{u}_0 + \rho \mathbf{u}_0 \cdot \nabla \mathbf{u}_0 + \nabla p - \frac{1}{4\pi c^2} \nabla \phi \nabla^2 \phi \right) - \frac{1}{4\pi c^2} \partial_t \nabla \phi. \quad (4.45)$$

Notice that from $O(\epsilon^2)$ of Eq. (4.9), we have

$$\nabla \times \mathbf{B}_2 + \frac{1}{c^2} \partial_t \nabla \phi = \frac{4\pi}{c} \mathbf{J}_2. \quad (4.46)$$

If we define the following ‘‘integration over a flux tube’’ operator:

$$\langle f \rangle \equiv \int (dl/B_0) f, \quad (4.47)$$

where dl is the line element along a field line and the integration is taken between the two mirror throats, then we have

$$\langle \nabla \cdot \nabla \times \mathbf{B}_2 \rangle = \langle \nabla \cdot (\nabla \times \mathbf{B}_2)_\perp \rangle + \langle \nabla \cdot (\nabla \times \mathbf{B}_2)_\parallel \rangle = 0. \quad (4.48)$$

From the divergence theorem, $\langle \nabla \cdot (\nabla \times \mathbf{B}_2)_\parallel \rangle$ can be transformed into a surface integration. Since $(\nabla \times \mathbf{B}_2)_\parallel$ lies on a flux surface by definition, and the contributions from both ends of a flux tube cancel each other due to the periodicity, we have $\langle \nabla \cdot (\nabla \times \mathbf{B}_2)_\parallel \rangle = 0$; therefore,

$$\langle \nabla \cdot (\nabla \times \mathbf{B}_2)_\perp \rangle = 0. \quad (4.49)$$

Eqs. (4.44) and (4.49) determine the time evolution of u_\parallel and ϕ . To complete the set, we need two more equations for ρ and p , which can be obtained by taking the leading order of (4.3) and (4.5).

Since only the leading order of \mathbf{B} and \mathbf{u} appear in the reduced equations, we may drop the subscript “0” for simplicity. Now we summarize the full set of reduced equations as follows: The full set of equations for ϕ , u_{\parallel} , ρ , and p are:

$$\partial_t \rho + \nabla \cdot (\rho \mathbf{u}) = 0, \quad (4.50)$$

$$\partial_t p + \mathbf{u} \cdot \nabla p + \gamma p \nabla \cdot \mathbf{u} = 0. \quad (4.51)$$

$$\hat{b} \cdot (\rho \partial_t \mathbf{u} + \rho \mathbf{u} \cdot \nabla \mathbf{u} + \nabla p) = 0, \quad (4.52)$$

$$\left\langle \nabla \cdot \left(\frac{\hat{b}}{B} \times \left(\rho \partial_t \mathbf{u} + \rho \mathbf{u} \cdot \nabla \mathbf{u} + \nabla p - \frac{1}{4\pi c^2} \nabla \phi \nabla^2 \phi \right) \right) - \frac{1}{4\pi c^2} \partial_t \nabla^2 \phi \right\rangle = 0. \quad (4.53)$$

Notice that \mathbf{B} is the external field defined by (4.38) in terms of ψ , which must satisfy Eq. (4.39); \mathbf{u} is defined by (4.42) in terms of u_{\parallel} and ϕ ; ϕ has to satisfy (4.41).

4.4.2 Linearized Equations

Now we linearize Eqs. (4.50)–(4.53) about an axisymmetric equilibrium. The equilibrium is characterized by the electrostatic potential $\phi = \phi(\psi)$, which determines the azimuthal flow $\mathbf{u} = r\Omega\hat{\zeta}$, where $\Omega = d\phi/d\psi$ is the angular velocity. Because of the centrifugal force, neither p nor ρ is a function of ψ . From Eq. (4.52), p and ρ must satisfy

$$\hat{b} \cdot \nabla p = \rho r \Omega^2 (\hat{b} \cdot \hat{r}). \quad (4.54)$$

The linearization calculation is rather involved. Here we simply present the linearized equations and leave the detail of derivation to Appendix B. Denoting the perturbed quantities as $\tilde{\phi}$, \tilde{u}_{\parallel} , $\tilde{\rho}$, and \tilde{p} , the linearized equations are:

$$\frac{d\tilde{\rho}}{dt} - \frac{\partial \rho}{\partial \psi} G \frac{\partial \tilde{\phi}}{\partial \zeta} + \mathbf{B} \cdot \nabla \left(\frac{\rho \tilde{u}_{\parallel}}{B} \right) = 0, \quad (4.55)$$

$$\frac{d\tilde{p}}{dt} - \frac{\partial p}{\partial \psi} F \frac{\partial \tilde{\phi}}{\partial \zeta} + \gamma p \mathbf{B} \cdot \nabla \left(\frac{\tilde{u}_{\parallel}}{B} \right) + \tilde{u}_{\parallel} \hat{b} \cdot \nabla p = 0, \quad (4.56)$$

$$\rho \frac{d\tilde{u}_{\parallel}}{dt} - 2\rho r\Omega (\hat{r} \cdot \hat{b}) \frac{\partial \tilde{\phi}}{\partial \psi} = -\hat{b} \cdot \nabla \tilde{p} + \tilde{\rho} r \Omega^2 (\hat{r} \cdot \hat{b}), \quad (4.57)$$

$$\begin{aligned} \frac{d}{dt} \left(\frac{\partial}{\partial \psi} \left(\langle \rho_{\star} r^2 \rangle \frac{\partial \tilde{\phi}}{\partial \psi} \right) + \left\langle \frac{\rho_{\star}}{r^2 B^2} \right\rangle \frac{\partial^2 \tilde{\phi}}{\partial \zeta^2} \right) - \frac{\partial}{\partial \psi} \left\langle \rho_{\star} \frac{\partial(r^2 \Omega)}{\partial \psi} \right\rangle \frac{\partial \tilde{\phi}}{\partial \zeta} \\ = -2 \frac{\partial}{\partial \psi} \left(\Omega \langle \rho r \hat{b} \cdot \hat{r} \tilde{u}_{\parallel} \rangle \right) + 2 \left\langle \frac{\boldsymbol{\kappa} \cdot \nabla \psi}{B^2 r^2} \frac{\partial \tilde{p}}{\partial \zeta} \right\rangle - \Omega^2 \left\langle \frac{\hat{b} \cdot \hat{z}}{B} \frac{\partial \tilde{\rho}}{\partial \zeta} \right\rangle. \end{aligned} \quad (4.58)$$

where

$$\frac{d}{dt} \equiv \frac{\partial}{\partial t} + \Omega \frac{\partial}{\partial \zeta}, \quad (4.59)$$

$$\frac{\partial}{\partial \psi} \equiv \frac{1}{r^2 B^2} \nabla \psi \cdot \nabla, \quad (4.60)$$

$$\rho_{\star} \equiv \rho \left(1 + \frac{V_A^2}{c^2} \right), \quad (4.61)$$

$$F \equiv 1 - \frac{2\gamma p}{B^2 r^2 \partial p / \partial \psi} \boldsymbol{\kappa} \cdot \nabla \psi, \quad (4.62)$$

$$G \equiv 1 - \frac{2\rho}{B^2 r^2 \partial \rho / \partial \psi} \boldsymbol{\kappa} \cdot \nabla \psi, \quad (4.63)$$

and $\boldsymbol{\kappa} = \hat{b} \cdot \nabla \hat{b}$ is the curvature of magnetic field lines.

Eqs. (4.55)–(4.58) describe a linearized, quasi-two-dimensional dynamic system. The coupling between the two-dimensional interchanges and the dynamics parallel to the magnetic field through \tilde{u}_{\parallel} makes the system difficult to analyze. However, the coupling terms between \tilde{u}_{\parallel} and other variables are all proportional to $\hat{b} \cdot \nabla$ or $\hat{b} \cdot \hat{r}$. $\hat{r} \cdot \hat{b}$ scales as R/L . For simple interchange modes, i.e., sound waves along the field are not excited, $\hat{b} \cdot \nabla$ scales as $1/L$. If we consider only simple interchanges in a highly elongated system, then we may neglect \tilde{u}_{\parallel} in (4.55), (4.56), and (4.58), therefore decouple the interchanges from the dynamics of the third dimension. Under this ansatz, we have a simplified system as:

$$\frac{d\tilde{\rho}}{dt} - \frac{\partial \rho}{\partial \psi} G \frac{\partial \tilde{\phi}}{\partial \zeta} = 0, \quad (4.64)$$

$$\frac{d\tilde{p}}{dt} - \frac{\partial p}{\partial \psi} F \frac{\partial \tilde{\phi}}{\partial \zeta} = 0, \quad (4.65)$$

$$\begin{aligned} \frac{d}{dt} \left(\frac{\partial}{\partial \psi} \left(\langle \rho_\star r^2 \rangle \frac{\partial \tilde{\phi}}{\partial \psi} \right) + \langle \frac{\rho_\star}{r^2 B^2} \rangle \frac{\partial^2 \tilde{\phi}}{\partial \zeta^2} \right) - \frac{\partial}{\partial \psi} \left\langle \rho_\star \frac{\partial(r^2 \Omega)}{\partial \psi} \right\rangle \frac{\partial \tilde{\phi}}{\partial \zeta} \\ = 2 \left\langle \frac{\boldsymbol{\kappa} \cdot \nabla \psi}{B^2 r^2} \frac{\partial \tilde{p}}{\partial \zeta} \right\rangle - \Omega^2 \left\langle \frac{\hat{\mathbf{b}} \cdot \hat{\mathbf{z}}}{B} \frac{\partial \tilde{\rho}}{\partial \zeta} \right\rangle. \end{aligned} \quad (4.66)$$

4.4.3 Linear Stability – Normal Mode Analysis

Assuming the eikonal solution $\tilde{\phi} \rightarrow \tilde{\phi} \exp(-i\omega t + im\zeta)$, etc., we can replace d/dt in (4.64)–(4.66) by $-i\bar{\omega}t$, where $\bar{\omega} \equiv \omega - m\Omega$. Combining the resulting equations leads to a single eigenvalue equation:

$$\frac{d}{d\psi} \left(\langle \rho_\star r^2 \rangle \frac{d\tilde{\phi}}{d\psi} \right) - m^2 \langle \frac{\rho_\star}{r^2 B^2} \rangle \tilde{\phi} + \frac{m}{\bar{\omega}} \frac{d}{d\psi} \left\langle \rho_\star \frac{\partial(r^2 \Omega)}{\partial \psi} \right\rangle \tilde{\phi} = \frac{m^2}{\bar{\omega}^2} H \tilde{\phi}, \quad (4.67)$$

where

$$H(\psi) \equiv 2 \left\langle \frac{\boldsymbol{\kappa} \cdot \nabla \psi}{B^2 r^2} \frac{\partial p}{\partial \psi} F \right\rangle - \Omega^2 \left\langle \frac{\hat{\mathbf{b}} \cdot \hat{\mathbf{z}}}{B} \frac{\partial \rho}{\partial \psi} G \right\rangle. \quad (4.68)$$

The left-hand-side (LHS) of (4.67) represents the inertial effect, while the right-hand-side (RHS) represents the destabilizing or stabilizing effect driven by the density and pressure stratifications. Notice that the EM field momentum increases the density ρ in inertial terms to ρ_\star by a factor of $1 + V_A^2/c^2$, while the interchange driving term H remains unchanged. Therefore, we again expect low density plasmas to be more stable. Eq. (4.67) is analogous to the classic Taylor–Goldstein equation [22]. Many results related to the Taylor–Goldstein equation can be carried over to the present system with some generalization.

Sufficient Condition for the Non-existence of Unstable Normal Modes

First we prove a sufficient condition for the non-existence of unstable normal modes. Let $\omega = \omega_r + i\omega_i$, where ω_r and ω_i are the real and imaginary parts of ω , respectively.

With the definition

$$h \equiv \frac{\tilde{\phi}}{\bar{\omega}^2}, \quad (4.69)$$

and substituting h for $\tilde{\phi}$ in (4.67), we have

$$\begin{aligned} & (\langle \rho_\star r^2 \rangle \bar{\omega} h')' = \\ & m \left(\frac{(\langle \rho_\star r^2 \rangle \Omega')'}{2} - \left\langle \rho_\star \frac{\partial (r^2 \Omega)}{\partial \psi} \right\rangle' + m \left(\frac{\langle \rho_\star r^2 \rangle (\Omega')^2}{4\bar{\omega}} + \bar{\omega} \left\langle \frac{\rho_\star}{r^2 B^2} \right\rangle + \frac{H}{\bar{\omega}} \right) \right) h, \end{aligned} \quad (4.70)$$

where primes denote $d/d\psi$. Operating on (4.70) with $\int d\psi h^*$, integrating by parts, and using the homogeneous boundary condition, we obtain

$$\begin{aligned} - \int d\psi \langle \rho_\star r^2 \rangle \bar{\omega} |h'|^2 = \\ \int d\psi \left[m \left(\frac{(\langle \rho_\star r^2 \rangle \Omega')'}{2} - \left\langle \rho_\star \frac{\partial (r^2 \Omega)}{\partial \psi} \right\rangle' \right) \right. \\ \left. + m^2 \left(\frac{\langle \rho_\star r^2 \rangle (\Omega')^2 + 4H}{4\bar{\omega}} + \bar{\omega} \left\langle \frac{\rho_\star}{r^2 B^2} \right\rangle \right) \right] |h^2|. \end{aligned} \quad (4.71)$$

Taking the imaginary part of (4.71) gives

$$\omega_i \int d\psi \langle \rho_\star r^2 \rangle |h'|^2 = \omega_i \int d\psi m^2 \left(\frac{1}{|\bar{\omega}|^2} \left(\frac{\langle \rho_\star r^2 \rangle (\Omega')^2}{4} + H \right) - \left\langle \frac{\rho_\star}{r^2 B^2} \right\rangle \right) |h^2|. \quad (4.72)$$

If $\langle \rho_\star r^2 \rangle (\Omega')^2 / 4 + H \leq 0$ *everywhere* within the domain, then (4.72) cannot be satisfied unless $\omega_i = 0$. Therefore, we have proved the following sufficient condition for the non-existence of unstable normal modes:

$$-\frac{H}{\langle \rho_\star r^2 \rangle (\Omega')^2} \geq \frac{1}{4} \text{ everywhere} \Rightarrow \text{no unstable normal mode exists.} \quad (4.73)$$

This is a generalization of the classic result that *no unstable normal mode exists if the local Richardson number is everywhere greater than or equal to one quarter*[22]. The physical significance of (4.73) is that, if the stratification is sufficiently stabilizing to overcome the destabilizing effect of shear flow, then no unstable mode could exist.

If the condition (4.73) is not satisfied, unstable modes could exist. Eq. (4.72) then gives an upper bound of the growth rate:

$$|\omega_i|^2 \leq \max \left\{ \left(\langle \rho_\star r^2 \rangle (\Omega')^2 / 4 + H \right) / \langle \rho_\star / r^2 B^2 \rangle \right\}. \quad (4.74)$$

Generalized Rayleigh's Criterion

A well-known sufficient condition for the stability of an unstratified shear flow is the Rayleigh's inflexion point criterion [22]. To the best of our knowledge, there is no *exact* generalization of the Rayleigh's inflexion point criterion for stratified shear flows. We may try to apply Rayleigh's strategy by operating (4.67) with $\int d\psi \tilde{\phi}$, and integrating by parts, to yield

$$- \int d\psi \langle \rho_\star r^2 \rangle |\tilde{\phi}'|^2 = \int d\psi \left(m^2 \left\langle \frac{\rho_\star}{r^2 B^2} \right\rangle - \frac{m}{\bar{\omega}} \left\langle \rho_\star \frac{\partial (r^2 \Omega)}{\partial \psi} \right\rangle' + \frac{m^2 H}{\bar{\omega}^2} \right) |\tilde{\phi}|^2. \quad (4.75)$$

Taking the imaginary part of (4.75) gives

$$\omega_i \int d\psi \left(\frac{1}{|\bar{\omega}|^2} \left\langle \rho_\star \frac{\partial (r^2 \Omega)}{\partial \psi} \right\rangle' - \frac{2m(\omega_r - m\Omega)H}{|\bar{\omega}|^4} \right) |\tilde{\phi}|^2 = 0. \quad (4.76)$$

If $\omega_i \neq 0$, then we must have

$$\left\langle \rho_\star \frac{\partial (r^2 \Omega)}{\partial \psi} \right\rangle' = \frac{2m(\omega_r - m\Omega)H}{|\bar{\omega}|^2} \quad (4.77)$$

somewhere within the flow. Unfortunately, this condition involves both unknowns ω_r and ω_i , and does not imply a simple criterion like Rayleigh's. However, if $\langle \rho_\star \partial_\psi (r^2 \Omega) \rangle' \neq 0$ everywhere, then (4.77) gives an upper bound of growth rates:

$$|\omega_i| \leq \max \left| \frac{2mH}{\langle \rho_\star \partial_\psi (r^2 \Omega) \rangle'} \right|, \quad (4.78)$$

since $|\omega_i| \leq |\bar{\omega}| = 2m(\omega_r - m\Omega)H / |\bar{\omega}| \langle \rho_\star \partial_\psi (r^2 \Omega) \rangle'$ somewhere. In the limit $H \rightarrow 0$, the condition (4.77) implies the following generalized Rayleigh's criterion:

$$\langle \rho_\star \partial_\psi (r^2 \Omega) \rangle' \neq 0 \text{ everywhere} \Rightarrow \text{stability}. \quad (4.79)$$

For a system satisfying the criterion (4.79), and having a relatively weak interchange driving force, i.e., $|H| / |\langle \rho_\star \partial_\psi (r^2 \Omega) \rangle'|$ being much smaller than other characteristic frequencies of the system, e.g., $r\Omega/a$, $\sqrt{|H| / \langle \rho/r^2 B^2 \rangle}$, the condition (4.78) sets a rather stringent upper bound on the growth rate of long wavelength modes ($m \sim O(1)$), therefore long wavelength modes are *likely* to be stable. For this reason, the criterion (4.79) may still be an useful indicator for the stability of long wavelength modes, although no conclusive answer can be drawn from it in general when $H \neq 0$. From simple dimensional analysis, it can be shown that H may be negligible for long wavelength modes in an elongated ($L \gg R$) and large aspect ratio ($R \gg a$) system.

Localized Growing Modes Around the Point $\Omega' = 0$

An important result that can be deduced from normal mode analysis is that, if the local stratification is destabilizing at a point where $\Omega' = 0$, then localized unstable modes would be present there. This can be shown by applying the Simmons–Killworth asymptotic method as done by Benilov et. al. [6]. Letting

$$\tilde{\phi} = \frac{s}{\langle \rho_\star r^2 \rangle^{1/2}}, \quad (4.80)$$

we can rewrite (4.67) in terms of s :

$$s'' - W(\psi, \omega)s = 0, \quad (4.81)$$

where

$$W = \frac{\langle \rho_\star r^2 \rangle''}{2 \langle \rho_\star r^2 \rangle} - \frac{\langle \rho_\star r^2 \rangle'^2}{4 \langle \rho_\star r^2 \rangle} + \frac{m^2}{\langle \rho_\star r^2 \rangle} \left\langle \frac{\rho_\star}{r^2 B^2} \right\rangle - \frac{m \langle \rho_\star \partial_\psi (r^2 \Omega) \rangle'}{\langle \rho_\star r^2 \rangle \bar{\omega}} + \frac{m^2 H}{\langle \rho_\star r^2 \rangle \bar{\omega}^2}. \quad (4.82)$$

We solve Eq. (4.81) in the asymptotic limit $m \rightarrow \infty$. Assuming normal modes localized about ψ_0 with leading order frequency ω_0 (both undetermined at this stage), we expand V about ψ_0 and ω_0 :

$$s'' - \left(W|_{(\psi_0, \omega_0)} + \partial_\psi W|_{(\psi_0, \omega_0)} (\psi - \psi_0) + \partial_\omega W|_{(\psi_0, \omega_0)} (\omega - \omega_0) + \frac{1}{2} \partial_\psi^2 W|_{(\psi_0, \omega_0)} (\psi - \psi_0)^2 + \dots \right) s = 0. \quad (4.83)$$

As discussed in Ref. [6], the first two terms within the parenthesis of Eq. (4.83) do not allow localized solutions; therefore we must require

$$W|_{(\psi_0, \omega_0)} = 0, \quad (4.84)$$

and

$$\partial_\psi W|_{(\psi_0, \omega_0)} = 0. \quad (4.85)$$

Eqs. (4.84) and (4.85) give

$$\omega_0 = m\Omega(\psi_0) \pm N(\psi_0) + O(m^{-1}), \quad (4.86)$$

and

$$\Omega'(\psi_0) = O(m^{-1}), \quad (4.87)$$

where

$$N(\psi) \equiv \sqrt{\frac{-H}{\langle \rho_\star / r^2 B^2 \rangle}}. \quad (4.88)$$

Therefore, to leading order, ψ_0 is located at an extremum of the angular velocity profile. Now letting $\omega_1 \equiv \omega - \omega_0$, $\eta \equiv \psi - \psi_0$, Eq. (4.83) can be rewritten (to the leading non-trivial order) as:

$$s'' - (T\omega_1 + W\eta^2) s = 0, \quad (4.89)$$

where

$$T = \pm m^2 \left(\frac{2 \langle \rho_\star / r^2 B^2 \rangle}{\langle \rho_\star r^2 \rangle} \sqrt{\frac{\langle \rho_\star / r^2 B^2 \rangle}{-H}} \Big|_{\psi_0} + O(m^{-1}) \right), \quad (4.90)$$

$$W = \mp m^3 \left(\frac{\Omega'' \langle \rho_\star / r^2 B^2 \rangle}{\langle \rho_\star r^2 \rangle} \sqrt{\frac{\langle \rho_\star / r^2 B^2 \rangle}{-H}} \Big|_{\psi_0} + O(m^{-1}) \right); \quad (4.91)$$

the upper (lower) sign here corresponds to that defined in Eq. (4.86). We are looking for solutions that are localized about $\eta = 0$, i.e. $s \rightarrow 0$ as $\eta \rightarrow \pm\infty$. Eq. (4.89) is identical to the eigenvalue problem of a quantum harmonic oscillator; bounded solutions exist only if [15]

$$\omega_1 = -\frac{2W^{1/2}(n + 1/2)}{T}, \quad (4.92)$$

where n is a positive integer and $W^{1/2}$ is chosen such that $\text{Re}(W^{1/2}) > 0$. The corresponding eigenfunction is

$$s = \exp\left(-W^{1/2}\eta^2/2\right) H_n(W^{1/4}\eta), \quad (4.93)$$

where H_n is the Hermite polynomial of order n . If the system has a stabilizing stratification at ψ_0 , i.e., $H(\psi_0) < 0$, then $\omega \simeq \omega_0 + \omega_1$ is real, therefore the localized eigenmodes are stable. On the other hand, if $H(\psi_0) > 0$, then ω is complex. In this case, the growth rate of trapped unstable modes are:

$$\text{Im}(\omega) \simeq |N(\psi_0)| \left(1 - \left(n + \frac{1}{2} \right) \sqrt{\frac{\langle \rho_* r^2 \rangle |\Omega''|}{2m \langle \rho_* / r^2 B^2 \rangle |N|_{|\psi_0}}} \right). \quad (4.94)$$

That is, at a point ψ_0 where velocity shear vanishes ($\Omega'(\psi_0) = 0$), localized modes of short wavelengths ($m \rightarrow \infty$) grow at the local growth rate $|N(\psi_0)|$.

4.4.4 Linear Stability – Initial-Value Analysis

It is well-known that normal mode analysis cannot completely determine the stability of a system with shear flow, essentially due to the fact that normal modes may not form a complete set. A classic example is the inviscid plane Couette flow, where normal mode analysis yields no solution. In Ref. [17], Case suggested posing flow stability as an initial-value problem. He solved the inviscid plane Couette flow by performing a Laplace transform in time, and he found that for an arbitrary initial condition, the solution can be expressed as a linear superposition of continuum modes (although there is no *discrete* normal modes). In a subsequent study of the stability of an ideal, stratified atmosphere in a half-infinite space with a linear shear flow[16], Case found algebraic decay of an initial disturbances in the asymptotic limit $t \rightarrow \infty$. The Laplace transform method, although conceptually very straightforward, usually leads to complicated analysis even for very simple systems, and different authors obtained different algebraically decaying rates (see Ref. [14] and references therein). The controversy was finally resolved by Brown and Stewartson

[14], whose result agrees with later results of Knobloch [46] and Hassam [30] obtained by transforming to the comoving frame of the equilibrium flow. The early studies in the fluid community [16, 20, 14, 46] usually focused on the stabilizing effect of a stabilizing stratification on a shear flow, where disturbances are found to decay algebraically as $t \rightarrow \infty$. However, the same analysis can be readily applied to an ideal shear flow with a destabilizing stratification, and initial perturbations can be shown to grow algebraically as $t \rightarrow \infty$. In recent years, shear flow is widely recognized as a stabilizing effect in the plasma community (see Ref. [62] and references therein). In Ref. [30], Hassam found that stabilization is possible only when nonideal effects such as viscosity and diffusivity are taken into account — as the perturbation structure becomes finer and finer due to the shear flow, nonideal effects become important and eventually damp out the algebraic growth.

For an unbounded, linear shear flow, initial value analysis can be significantly simplified by transforming to the comoving frame of the equilibrium flow [30, 46]. Unfortunately, this method is not applicable for general flow profiles or bounded flows. Here we limit ourselves to a local analysis as done in Ref. [32, 33], which is valid for local disturbances of a length scale much smaller than the characteristic length scale of the background shear flow and stratification. By making the following transformations $x = \psi$, $\xi = \zeta - \Omega t$, $\tau = t$, we have $\partial_\psi = \partial_x - \Omega' \tau \partial_\xi$, $\partial_\zeta = \partial_\xi$, $\partial_t = \partial_\tau - \Omega \partial_\xi$, $d/dt = \partial_\tau$; therefore, in these new coordinates, Eqs. (4.64)-(4.66) become

$$\partial_\tau \tilde{\rho} - \frac{\partial \rho}{\partial \psi} G \frac{\partial \tilde{\phi}}{\partial \xi} = 0, \quad (4.95)$$

$$\partial_\tau \tilde{p} - \frac{\partial p}{\partial \psi} F \frac{\partial \tilde{\phi}}{\partial \xi} = 0, \quad (4.96)$$

$$\begin{aligned} \partial_\tau \left((\partial_x - \Omega' \tau \partial_\xi) \left(\langle \rho_\star r^2 \rangle (\partial_x \tilde{\phi} - \Omega' \tau \partial_\xi \tilde{\phi}) \right) + \left\langle \frac{\rho_\star}{r^2 B^2} \right\rangle \frac{\partial^2 \tilde{\phi}}{\partial \xi^2} \right) \\ - \frac{\partial}{\partial \psi} \left\langle \rho_\star \frac{\partial(r^2 \Omega)}{\partial \psi} \right\rangle \frac{\partial \tilde{\phi}}{\partial \xi} = 2 \left\langle \frac{\boldsymbol{\kappa} \cdot \nabla \psi}{B^2 r^2} \frac{\partial \tilde{p}}{\partial \xi} \right\rangle - \Omega^2 \left\langle \frac{\hat{b} \cdot \hat{z}}{B} \frac{\partial \tilde{\rho}}{\partial \xi} \right\rangle. \end{aligned} \quad (4.97)$$

We assume that the disturbances are localized about some flux surface $\psi = \psi_0$ (which can be different from the ψ_0 of Sec. 4.4.3) and the characteristic wavelengths of the disturbances are much shorter than the length scale of equilibrium profiles. Under this “local” ansatz, the derivatives of equilibrium variables are negligible compared with derivatives of perturbed variables, and Eq. (4.97) is approximately

$$\partial_\tau \left(\langle \rho_\star r^2 \rangle (\partial_x - \Omega' \tau \partial_\xi)^2 \tilde{\phi} + \left\langle \frac{\rho_\star}{r^2 B^2} \right\rangle \frac{\partial^2 \tilde{\phi}}{\partial \xi^2} \right) = 2 \left\langle \frac{\boldsymbol{\kappa} \cdot \nabla \psi}{B^2 r^2} \frac{\partial \tilde{p}}{\partial \xi} \right\rangle - \Omega^2 \left\langle \frac{\hat{b} \cdot \hat{z}}{B} \frac{\partial \tilde{\rho}}{\partial \xi} \right\rangle, \quad (4.98)$$

where equilibrium variables are evaluated at $\psi = \psi_0$. The same approximation is applied to Eqs. (4.95) and (4.96). In these coordinates, x is ignorable. We look for modes with $\partial_x = 0$ since those are the fastest growing modes. ξ is also ignorable: we let $\partial_\xi \rightarrow im$. Eliminating $\tilde{\rho}$ and \tilde{p} , we obtain for $\tilde{\phi}$

$$\partial_\tau^2 \left[\left(\left\langle \frac{\rho_\star}{r^2 B^2} \right\rangle + \langle \rho_\star r^2 \rangle (\Omega' \tau)^2 \right) \tilde{\phi} \right] = H(\psi_0) \tilde{\phi}. \quad (4.99)$$

Eq. (4.99) can be solved exactly by Legendre polynomials, but the asymptotic behavior of the two linearly independent solutions as $t \rightarrow \infty$ can be readily obtained as $\tilde{\phi} \sim \tau^\alpha$, where

$$\alpha = \frac{-3 \pm \sqrt{1 + 4H / \langle \rho_\star r^2 \rangle (\Omega')^2}}{2}. \quad (4.100)$$

And from (4.95) and (4.96), we have both $\tilde{\rho}$ and $\tilde{p} \sim \tau^{\alpha+1}$; therefore, if the local stratification is destabilizing ($H > 0$), both $\tilde{\rho}$ and \tilde{p} grow unboundedly (but only algebraically). If viscosity and resistivity are taken into account, as done in Ref. [30], the algebraic growth is efficiently phase mixed by the velocity shear, resulting in stabilization. A conservative stability criterion based on negligible growth is:

$$(\Omega')^2 > \frac{H}{\langle \rho_\star r^2 \rangle} \ln(R_\mu), \quad (4.101)$$

where R_μ is a Reynolds number. The effective density $\rho_\star = (1 + V_A^2/c^2)\rho$ in the denominator indicates that a low density plasma is easier to stabilize. An analysis similar to Ref. [30] was done by Knobloch [46], although the latter did not put stress

on velocity shear stabilization. Recently a similar analysis has also been carried out including finite Larmor radius effects. These were found to be stabilizing, and a stabilization criterion similar to (4.101) was obtained¹.

4.5 Summary and Discussion

In this Chapter we study the interchange instability of low density plasmas by including the electric force and displacement current that are usually omitted in the MHD equations. We first apply the equations in a line-tied slab geometry and find that including these terms effectively increases the inertia of plasma by a factor of $1 + V_A^2/c^2$; as a result, the interchange growth rate is reduced a factor $\sqrt{1 + V_A^2/c^2}$. We then study interchanges in centrifugally confined plasmas, which extends a previous calculation [32] to take into account the effects of both curved magnetic field and low density plasma. Analytic results in Ref. [32] are generalized in this study. If we schematically let $\Omega' \sim \Omega/RaB$, $F \sim G \sim O(1)$, $\kappa \sim 1/L$ in the velocity shear stabilization criterion (4.101), we have the schematic stability criterion

$$\frac{R}{a} > \frac{\ln(R_\mu)}{1 + V_A^2/c^2} \left(\frac{a}{L_\rho} + \frac{1}{M_S^2} \frac{Ra}{LL_p} \right), \quad (4.102)$$

where L_ρ is the density scale size, L_p is the pressure scale size, and $M_S \equiv R\Omega/C_S$ is the sonic Mach number. In the limit $V_A \ll c$, the schematic stability criterion in Ref. [32] is recovered. Notice that ρ_* appears in (4.101) through an average over a flux tube. If $V_A \ll c$ throughout most of the system and $V_A \sim c$ only near the mirror throats, then the contribution of low density plasma effects is negligible.

Finally, we comment that although the low density plasma effect is negligible unless $V_A \gtrsim c$ everywhere, Eqs. (4.3)–(4.9) may still be useful if one is to simulate a magnetized plasma in which the density could become significantly low using an explicit time stepping scheme. The reason is as follows: For explicit time

¹S.-W. Ng, private communication.

stepping schemes, the Courant-Friedrichs-Levy (CFL) stability criterion[57] requires that $\Delta t < O(1)\Delta x/V$, where Δx is the grid size, Δt the time step, and V corresponds to any characteristic speeds, e.g., flow speed, phase speeds of waves, of the system. In the usual MHD, wave speeds ($\sim V_A$) approach infinity as the density goes to zero; therefore the CFL criterion poses a very strict limit on the time step. On the other hand, the MHD wave dispersion relation of Eqs. (4.3)–(4.9) can be shown to be:

$$\omega^2 \left(\left(1 + \frac{V_A^2}{c^2} \right) \tilde{\mathbf{u}} - \frac{(\mathbf{V}_A \cdot \tilde{\mathbf{u}}) \mathbf{V}_A}{c^2} \right) = (C_S^2 + V_A^2) (\mathbf{k} \cdot \tilde{\mathbf{u}}) \mathbf{k} + \mathbf{k} \cdot \mathbf{V}_A ((\mathbf{k} \cdot \mathbf{V}_A) \tilde{\mathbf{u}} - (\mathbf{k} \cdot \tilde{\mathbf{u}}) \mathbf{V}_A - (\mathbf{V}_A \cdot \tilde{\mathbf{u}}) \mathbf{k}), \quad (4.103)$$

where $\tilde{\mathbf{u}}$ is the perturbed velocity, \mathbf{k} is the wave number vector, $\mathbf{V}_A = \mathbf{B}/4\pi\rho$. In the limit $V_A \ll c$, the usual MHD wave dispersion relation is recovered. Eq. (4.103) gives three independent modes, with

$$\left(\frac{\omega}{k} \right)^2 = \frac{V_A^2 \cos^2 \theta}{1 + V_A^2/c^2}, \quad (4.104)$$

$$\left(\frac{\omega}{k} \right)^2 = \frac{K \pm \sqrt{K^2 - 4C_S^2 V_A^2 (1 + V_A^2/c^2) \cos^2 \theta}}{2(1 + V_A^2/c^2)}, \quad (4.105)$$

where θ is the angle between \mathbf{k} and \mathbf{B} , and

$$K \equiv C_S^2 + V_A^2 + C_S^2 V_A^2 \cos^2 \theta/c^2. \quad (4.106)$$

Eq. (4.104) corresponds to the shear Alfvén wave and the plus and minus signs of Eq. (4.105) correspond to the fast and slow magnetosonic waves, respectively. One can prove that the phase velocity ω/k of (4.104) and (4.105) is always slower than the speed of light (assuming $C_S < c$); therefore the time step is only limited by $\Delta t < O(1)\Delta x/c$, which is less stringent.

Chapter 5

Magnetorotational and Parker Instabilities in Magnetized Plasma Dean Flow as Applied to Centrifugally Confined Plasmas

5.1 Introduction

Thus far, all the previous studies are based on the ordering $C_S \lesssim u \ll V_A$, where C_S is the sound speed, u is the flow speed, and V_A is the Alfvén speed. In that case, the strong magnetic field stabilizes any fluctuation along the field, and the calculations were done for non-axisymmetric flute modes. From the fusion viewpoint, however, the output power is proportional to the square of the particle density; for a device with a given magnetic field, a high β ($\equiv 2p/B^2 \sim C_S^2/V_A^2$) system with $u \sim V_A$ is highly desirable. For such a system, the magnetic field may not be strong enough to stabilize fluctuations along the field. Thus, ideal MHD instabilities with axial wavenumbers need investigation.

An immediate concern is the magnetorotational instability (MRI) [65, 18, 2, 4]. Since the recent work by Balbus and Hawley [2], the MRI has attracted broad attention and is believed to be the cause of the turbulent angular momentum transport in accretion disks. Roughly speaking, the stability criterion based on a local analysis is (see Appendix C):

$$(kV_A)^2 > -\frac{d\Omega^2}{d\ln(r)}, \quad (5.1)$$

where k is the wavenumber and Ω is the angular frequency. Condition (5.1) can only be violated where $\partial_r \Omega^2 < 0$, which is usually true for most astrophysical disks. In a centrifugally confined plasma, a parabola-like Ω profile is expected [32, 36], hence the MRI is possible in the outboard half of the system. Condition (5.1) also indicates that a system with high Alfvén Mach number ($M_A \sim r\Omega/V_A$) and high elongation (which allows smaller k) is more prone to the MRI. Since both attributes are desirable for centrifugal confinement schemes (high M_A means high β , and elongation assists velocity shear stabilization, see Ref. [33]), whether or not the MRI is a fundamental limit needs more investigation.

Another possible destabilizing mechanism is magnetic buoyancy. It was first pointed out by Parker [54] that a magnetized plasma partially supported against gravity by a magnetic field could be unstable. When the Parker instability occurs, the plasma in a flux tube spontaneously fragments into clumps, which are then pulled “downward” by the gravity. Meanwhile, the dilute parts of the flux tube bulge upward, in a way that resembles a buoyant light bubble in a heavy fluid. Parker suggested this as an explanation for the non-uniformity of the interstellar medium inside a galaxy. Although there is no gravity in the centrifugal confinement scheme, the plasma is supported by the magnetic field against the centrifugal force, which plays the role of the gravity. It was pointed out in Ref. [45] that for rotating stellar winds or accretion disks in which the magnetic pressure of non-uniform poloidal magnetic fields balance the combination of gravity and centrifugal forces, a poloidal buoyancy mode resembling the Parker instability could occur. The same instability would also be an issue for the centrifugal confinement scheme.

In this Chapter, we study the above-mentioned issues in more detail. To avoid the complication of the curved-field geometry of the centrifugal confinement scheme, we model the system with the straight-field Dean flow model, as we did in our previous study [32]. The effect of a curved field, though not fully understood at present, will be briefly assessed later. It is worth pointing out that although the

MRI and the magnetic buoyancy instability involve different mechanisms, they are inextricably coupled, and there is no way to clearly distinguish one from the other.

This Chapter is organized as follows: In Sec. 5.2, we set up the Dean flow model and the governing equations. In Sec. 5.3, we first linearize the equations about the equilibrium, then numerically solve the eigenvalue equation so obtained by a shooting code. Before solving the general equation, two simple limiting cases, the cold plasma limit and the incompressible limit, are considered. In Sec. 5.4, we confirm the results of Sec. 5.3 by a series of initial-value simulations. In Sec. 5.5, We discuss the implications for centrifugally confined plasmas. We conclude in Sec. 5.6.

5.2 The Dean Flow Model

For simplicity, we consider only the axisymmetric case. In the cylindrical coordinate system (r, ϕ, z) , the most general divergence-free magnetic field can then be written as

$$\mathbf{B} = I\nabla\phi + \nabla\phi \times \nabla\psi \equiv B_\phi\hat{\phi} + \mathbf{B}_\perp. \quad (5.2)$$

We decompose the flow velocity into the azimuthal component and the perpendicular component: $\mathbf{u} = u_\phi\hat{\phi} + \mathbf{u}_\perp$. The ideal MHD equations with an adiabatic equation of state (for $\partial/\partial\phi = 0$) are:

$$\frac{d\rho}{dt} = -\rho\nabla \cdot \mathbf{u}_\perp, \quad (5.3)$$

$$\rho \frac{d\mathbf{u}_\perp}{dt} = -\frac{\nabla_\perp I^2}{2r^2} - \frac{\nabla_\perp \psi}{r^2} \left(\nabla^2 \psi - 2\frac{\partial_r \psi}{r} \right) + \rho \frac{u_\phi^2}{r} \hat{r} - \nabla_\perp p, \quad (5.4)$$

$$\rho \frac{du_\phi}{dt} = \frac{\mathbf{B}_\perp \cdot \nabla_\perp I}{r} - \rho \frac{u_\phi u_r}{r}, \quad (5.5)$$

$$\frac{dI}{dt} = r^2 \mathbf{B}_\perp \cdot \nabla_\perp \left(\frac{u_\phi}{r} \right) - I r^2 \nabla \cdot \left(\frac{\mathbf{u}_\perp}{r^2} \right), \quad (5.6)$$

$$\frac{d\psi}{dt} = 0, \quad (5.7)$$

$$\frac{dp}{dt} = -\gamma p \nabla \cdot \mathbf{u}_\perp, \quad (5.8)$$

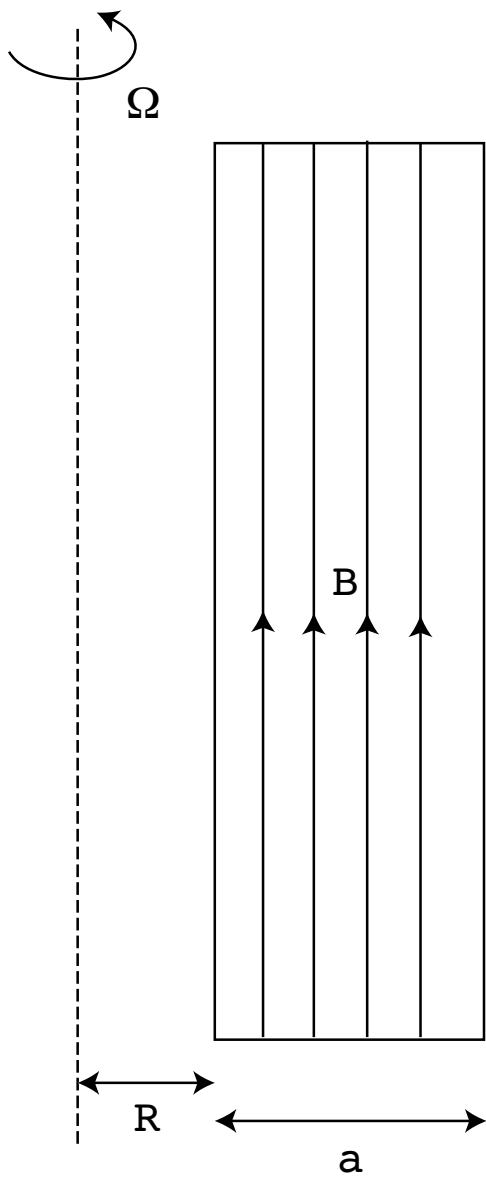


Figure 5.1: A Dean flow model for the straight section of a centrifugally confined plasma. A plasma within an annular box with inner radius R , width a and elongation L is threaded by a straight magnetic field in \hat{z} .

where

$$\frac{d}{dt} \equiv \frac{\partial}{\partial t} + \mathbf{u}_\perp \cdot \nabla_\perp, \quad (5.9)$$

$$\nabla_\perp \equiv \hat{r}\partial_r + \hat{z}\partial_z. \quad (5.10)$$

Standard notation is used. ρ is the plasma density, p is the pressure, and γ is the adiabatic index.

Fig. 5.1 depicts the Dean flow model we used. The plasma is contained in an annular box with inner radius R , box width a , and elongation L . We assume the following equilibrium: $p = \text{const}$, $\rho = \text{const}$, $\mathbf{B} = B(r)\hat{z} = -(1/r)\partial_r\psi\hat{z}$, and $\mathbf{u} = r\Omega(r)\hat{\phi}$. The centrifugal force is balanced by the magnetic force:

$$\rho r \Omega^2 = B \partial_r B = \frac{\partial_r \psi}{r^2} \left(\partial_r^2 \psi - \frac{\partial_r \psi}{r} \right). \quad (5.11)$$

The assumed flat density profile and pressure profile may seem special. To be sure, the gradient of those profiles will affect the stability criteria. However, this model captures the essential physics: the sheared velocity profile allows the MRI, and the compressibility allows a magnetic buoyancy instability. It is worth mentioning that in the centrifugal confinement scheme, a hot plasma is supported by the magnetic field against both the centrifugal force and the pressure gradient; for optimum confinement, a sonic Mach number of $M_S = 4 \sim 5$ is desired, which is to say that the centrifugal force dominates the pressure gradient provided the aspect ratio $R/a \ll M_S^2 \sim 20$. If the system has such a large aspect ratio (~ 20 , which is unlikely), we can no longer neglect the pressure gradient in force balance, and accordingly the constant pressure assumption is not appropriate.

5.3 Linear Stability Analysis

5.3.1 Derivation of the Eigenvalue Equation

We now linearize (5.3)-(5.8) about the above-mentioned equilibrium. We assume perturbations of the form $\rho \rightarrow \rho(r) + \tilde{\rho}(r) \exp(ik_z z - i\omega t)$, etc. The resulting lin-

earized equations are:

$$-i\omega\tilde{\rho} = -\rho \left(\tilde{u}_r' + ik_z\tilde{u}_z + \frac{\tilde{u}_r}{r} \right), \quad (5.12)$$

$$-i\omega\rho\tilde{u}_r = \frac{B}{r} \left(\tilde{\psi}'' - k_z^2\tilde{\psi} - \frac{\tilde{\psi}'}{r} \right) + \frac{\rho\Omega^2}{B}\tilde{\psi}' + 2\rho\Omega\tilde{u}_\phi + \tilde{\rho}r\Omega^2 - \tilde{p}', \quad (5.13)$$

$$-\omega\rho\tilde{u}_z = \frac{\rho\Omega^2}{B}k_z\tilde{\psi} - k_z\tilde{p}, \quad (5.14)$$

$$-i\omega\rho\tilde{u}_\phi = ik_z\frac{B}{r}\tilde{I} - 2\rho\Omega\tilde{u}_r - \rho r\Omega'\tilde{u}_r, \quad (5.15)$$

$$-\omega\tilde{I} = k_z r\Omega'\tilde{\psi} + k_z r B\tilde{u}_\phi, \quad (5.16)$$

$$-i\omega\tilde{\psi} = rB\tilde{u}_r, \quad (5.17)$$

$$-i\omega\tilde{p} = -\gamma p \left(\tilde{u}_r' + ik_z\tilde{u}_z + \frac{\tilde{u}_r}{r} \right), \quad (5.18)$$

where primes denote differentiation with respect to r . Eliminating \tilde{u}_z , \tilde{u}_ϕ , $\tilde{\rho}$, \tilde{p} , $\tilde{\psi}$, and \tilde{I} from Eq. (5.12)-(5.18), after some algebra, we obtain the following eigenvalue equation for \tilde{u}_r :

$$(\omega^2 - k_z^2 V_A^2) \left(F\tilde{u}_r'' + \frac{(rF)'}{r}\tilde{u}_r' + G\tilde{u}_r \right) - 4\omega^2\Omega^2(\omega^2 - k_z^2 C_S^2)\tilde{u}_r = 0, \quad (5.19)$$

where $C_S^2 \equiv \gamma p/\rho$, and $V_A^2(r) \equiv B^2(r)/\rho$ are the square of the sound speed and the Alfvén speed, respectively. The two functions $F(\omega, k_z, r)$ and $G(\omega, k_z, r)$ are defined as:

$$F = (V_A^2 + C_S^2)\omega^2 - k_z^2 V_A^2 C_S^2, \quad (5.20)$$

$$G = \omega^4 - \left(k_z^2 + \frac{1}{r^2}\right)F + 2\omega^2\Omega^2 - 2k_z^2 C_S^2(\Omega^2 - r\Omega\Omega') - k_z^2 r^2 \Omega^4. \quad (5.21)$$

In deriving Eq. (5.12)-(5.19), we use Eq. (5.11) repeatedly to express $B'(r)$ in terms of Ω .

We can eliminate the first-order derivative term of Eq. (5.19) by substituting $\tilde{u}_r = (rF)^{(-1/2)}u$. The eigenvalue equation for u is

$$(\omega^2 - k_z^2 V_A^2) (Fu'' + Hu) - 4\omega^2\Omega^2(\omega^2 - k_z^2 C_S^2)u = 0, \quad (5.22)$$

where

$$H = \omega^4 - \left(k_z^2 + \frac{3}{4r^2}\right)F + (2k_z^2 C_S^2 - \omega^2)2r\Omega\Omega' + \frac{r^2\Omega^4(\omega^2 - k_z^2 C_S^2)^2}{F} - k_z^2 r^2 \Omega^4. \quad (5.23)$$

We assume impenetrable hard wall boundary conditions; therefore, Eq. (5.22) has to be solved subject to the homogeneous boundary conditions $u(R) = u(R+a) = 0$.

In this study, we will take the parabolic angular frequency profile $\Omega = 4\Omega_0(r - R)(a + R - r)/a^2$ as our basic model, which mimics what we expect in the centrifugal confinement scheme. The system is then characterized by three parameters: the Mach number $M_S \equiv (R + a/2)\Omega_0/C_S$, the Alfvén Mach number $M_A \equiv (R + a/2)\Omega_0/(V_A|_{R+a})$, and the aspect ratio R/a . We took $R/a = 1/3$ for most parts of the study; the effect of the aspect ratio will be discussed briefly later. The main task of this work is to assess the stability with respect to the parameter space.

The eigenvalue equation (5.22) is quite complicated; numerical solutions are needed. A simple shooting code in MATHEMATICA is written for this purpose. The code allows complex eigenvalue ω^2 ; however, we found no solution with complex eigenvalue in this study (although we cannot prove this in general). Before tackling the general case, we will consider some limiting cases first.

5.3.2 Cold Plasma Limit, $C_S \rightarrow 0$

As a first limit, we assume the plasma to be cold. In the $C_S \rightarrow 0$ limit, equation (5.22) becomes

$$\begin{aligned} &\omega^2 V_A^2 u'' \\ &+ \left(\omega^4 - \left(k_z^2 + \frac{3}{4r^2} \right) \omega^2 V_A^2 - 2r\Omega\Omega'\omega^2 + \frac{r^2\Omega^4\omega^2}{V_A^2} - k_z^2 r^2 \Omega^4 - \frac{4\omega^4\Omega^2}{(\omega^2 - k_z^2 V_A^2)} \right) u = 0. \end{aligned} \quad (5.24)$$

The eigenvalue ω^2 of (5.24) can be shown to be real as follows. First we divide Eq. (5.24) by $\omega^2 V_A^2$, then operate the result by $\int_R^{R+a} dr u^*$. Integrating by parts and

applying the homogeneous boundary conditions, we obtain:

$$\int_R^{R+a} |u'|^2 dr = \int_R^{R+a} \left(\frac{\omega^2}{V_A^2} - k_z^2 - \frac{3}{4r^2} - \frac{2r\Omega\Omega'}{V_A^2} + \frac{r^2\Omega^4}{V_A^4} - \frac{k_z^2 r^2 \Omega^4}{\omega^2 V_A^2} - \frac{4\omega^2 \Omega^2}{V_A^2 (\omega^2 - k_z^2 V_A^2)} \right) |u|^2 dr. \quad (5.25)$$

The imaginary part of (5.25) is:

$$Im(\omega^2) \int_R^{R+a} \left(\frac{1}{V_A^2} + \frac{k_z^2 r^2 \Omega^4}{|\omega^2|^2 V_A^2} + \frac{4\Omega^2 k_z^2}{|\omega^2 - k_z^2 V_A^2|^2} \right) |u|^2 dr = 0. \quad (5.26)$$

The coefficient of $Im(\omega^2)$ in (5.26) is positive definite; therefore we must have $Im(\omega^2) = 0$. Since ω^2 is real, ω is either real or purely imaginary, which means the transition from stable modes to unstable modes must occur through $\omega = 0$. Therefore, we can look for marginal stability by letting $\omega = 0$ in Eq. (5.24), which simply yields $k_z = 0$ provided $\Omega \neq 0$. Since no marginal mode with nonzero k_z exists, either the system is stable for all k_z wavenumbers, or modes of all k_z are unstable. Now consider the short wavelength modes, $k_z \gg 1/a, 1/R$, and for the moment assume $|\omega| \ll k_z V_A$, since we are not interested in the those fast modes, which are stable. Under these approximations, Eq. (5.24) becomes

$$u'' - k_z^2 \left(1 + \frac{r^2 \Omega^4}{\omega^2 V_A^2} \right) u = 0. \quad (5.27)$$

Since k_z is large by assumption, for any localized solution of (5.27) which peaks at a certain radius r_0 , we must have

$$\left(1 + \frac{r^2 \Omega^4}{\omega^2 V_A^2} \right)_{r_0} \simeq 0; \quad (5.28)$$

otherwise the second term in the LHS of Eq. (5.27) will be very large. Eq. (5.28) gives the local dispersion relation $\omega^2 \simeq -r^2 \Omega^4 / V_A^2$, which corresponds to unstable modes with growth rate $\simeq r\Omega^2 / V_A$. This is the well known local Parker instability growth rate (see Ref. [54, 45], also Appendix D.1), with the centrifugal acceleration $r\Omega^2$ replacing the gravity in astrophysical systems. In this limit, the major

destablization mechanism comes from the centrifugal force, and the differential rotation Ω' is less important. The self-consistency condition $|\omega| \ll k_z V_A$ requires $r\Omega^2 \ll k_z V_A^2$, which can be easily satisfied with k_z large enough. The above local dispersion relation is confirmed for the basic model by numerical solutions with large k_z .

We have proved that short wavelength modes are unstable provided $\Omega \neq 0$. From our previous marginal mode argument, we have actually proved the system to be unstable for all k_z wavenumbers. The reason for this is not difficult to understand. If the plasma is cold, we can always compress the plasma along the field without consuming any work; that means we can build up a local high density region simply by compression — with no cost. One can make the local density as high as needed until the magnetic tension can no longer stop the centrifugal force from pulling it outward, Likewise, the low density part will be pushing inward due to the excess of the magnetic pressure. As we will see, including the plasma temperature, thus restoring the sound wave, stabilizes the Parker instability, especially for short wavelength modes.

5.3.3 Incompressible Limit, $C_S \rightarrow \infty$

We next consider the incompressible limit. In this limit, the system cannot have the magnetic buoyancy instability and MRI is the only mechanism of destabilization. Since the centrifugal confinement scheme, as we mentioned, requires high M_S , this limit may not be realistic. However, this limit can help us elucidate why the MRI is unlikely to be an issue in the centrifugal confinement scheme. In the $C_S \rightarrow \infty$ limit, Eq. (5.22) becomes

$$\begin{aligned}
 & (\omega^2 - k_z^2 V_A^2)^2 u'' \\
 & - \left(\left(k_z^2 + \frac{3}{4r^2} \right) (\omega^2 - k_z^2 V_A^2)^2 - 4k_z^2 (\omega^2 - k_z^2 V_A^2) r \Omega \Omega' - k_z^4 r^2 \Omega^4 - 4\omega^2 k_z^2 \Omega^2 \right) u = 0.
 \end{aligned}
 \tag{5.29}$$

It can be shown that ω^2 in the incompressible limit is real, as follows. It is easier to start from the $C_S \rightarrow \infty$ limit of the \tilde{u}_r equation, (5.19):

$$\begin{aligned} & (r(\omega^2 - k_z^2 V_A^2) \tilde{u}_r')' \\ & - \left(\left(k_z^2 + \frac{1}{r^2} \right) r(\omega^2 - k_z^2 V_A^2) + 2k_z^2 r \Omega(\Omega - r\Omega') - \frac{4\omega^2 \Omega^2 k_z^2 r}{\omega^2 - k_z^2 V_A^2} \right) \tilde{u}_r = 0. \end{aligned} \quad (5.30)$$

Applying $\int_R^{R+a} dr \tilde{u}_r^*$ on Eq. (5.30) and integrating by parts, we obtain:

$$\begin{aligned} & \int_R^{R+a} r(\omega^2 - k_z^2 V_A^2) |\tilde{u}_r'|^2 dr \\ & + \int_R^{R+a} \left(\left(k_z^2 + \frac{1}{r^2} \right) r(\omega^2 - k_z^2 V_A^2) + 2k_z^2 r \Omega(\Omega - r\Omega') - \frac{4\omega^2 \Omega^2 k_z^2 r}{\omega^2 - k_z^2 V_A^2} \right) |\tilde{u}_r|^2 dr = 0. \end{aligned} \quad (5.31)$$

Taking the imaginary part of Eq. (5.31), we get

$$Im(\omega^2) \left(\int_R^{R+a} r |\tilde{u}_r'|^2 dr + \int_R^{R+a} \left(\left(k_z^2 + \frac{1}{r^2} \right) r + \frac{4k_z^4 \Omega^2 V_A^2 r}{|\omega^2 - k_z^2 V_A^2|^2} \right) |\tilde{u}_r|^2 dr \right) = 0. \quad (5.32)$$

The coefficient of $Im(\omega^2)$ in (5.32) is positive definite; therefore we must have $Im(\omega^2) = 0$.

We solve the eigenvalue equation (5.29) by shooting method. For various M_A and R/a we have tried, no unstable mode was found for the basic model. This is confirmed by the result of the general case that the system is always stable when M_S is smaller than some critical value (see Sec. 5.3.4, and direct simulations in Sec. 5.4). In order to gain some understanding of this fact, we consider the local Wertzel-Kramers-Brillouin (WKB) dispersion relation as follows. It should be mentioned that the validity of the WKB dispersion relation for this kind of problem is questionable; nevertheless, previous studies show that it agrees with the global result to a certain extent, therefore it can be used as a reasonable stability criteria (see, for example, Ref. [40]). By letting $\partial_r^2 \rightarrow -k_r^2$ in Eq. (5.29), the WKB

dispersion relation is:

$$\begin{aligned} \left(k^2 + \frac{3}{4r^2}\right) \omega^4 - 2k_z^2 \left(V_A^2 \left(k^2 + \frac{3}{4r^2}\right) + 2(\Omega^2 + r\Omega\Omega')\right) \omega^2 \\ + k_z^4 \left(\left(k^2 + \frac{3}{4r^2}\right) V_A^4 + 4V_A^2 r\Omega\Omega' - r^2\Omega^4\right) = 0, \end{aligned} \quad (5.33)$$

with $k^2 \equiv k_r^2 + k_z^2$. Eq. (5.33) is quadratic in ω^2 , and it is easy to show that the determinant is positive, hence ω^2 is real. To have unstable modes, i.e. $\omega^2 < 0$, the constant term has to be negative, or

$$\left(k^2 + \frac{3}{4r^2}\right) V_A^4 < -4V_A^2 r\Omega\Omega' + r^2\Omega^4. \quad (5.34)$$

Eq. (5.34) indicates the key characteristic of the MRI — the flow shear is destabilizing only when $\Omega' < 0$. For the parabolic Ω profile we assumed, only the outboard half of the system could be unstable. Eq. (5.34) also indicates that a system with a larger angular frequency and a weaker magnetic field is more likely to be unstable. However, the force balance condition (5.11) relates the magnetic field strength to the angular frequency — they are no longer independent. This fact makes the centrifugal confinement device quite different from the accretion disk [4] and the proposed MRI experiment of liquid metal [40], where the centrifugal force is mostly balanced by gravity in the former (Keplerian flow) and pressure gradient in the later. In those cases the magnetic field could be arbitrarily weak, that makes the systems more prone to the MRI. Now we do a simple dimensional analysis. Roughly speaking, in the outboard half, $V_A^2 \sim ar\Omega^2$ from Eq. (5.11), and $\Omega' \sim -\Omega/a$. The minimum total wave number k is limited by the longest wavelength allowed by the system size, hence $k \gtrsim \pi/a$. Substituting all these into (5.34), we can see the instability criterion is not satisfied. Although this is a very crude estimate, it indicates that the MRI is unlikely to be an issue for the centrifugal confinement scheme. The reason for that is simple: for a system with parabola-like angular frequency, the MRI is only possible in the outboard half, where the magnetic field is strong enough to stabilize the MRI. One might think that for a system in which the angular frequency

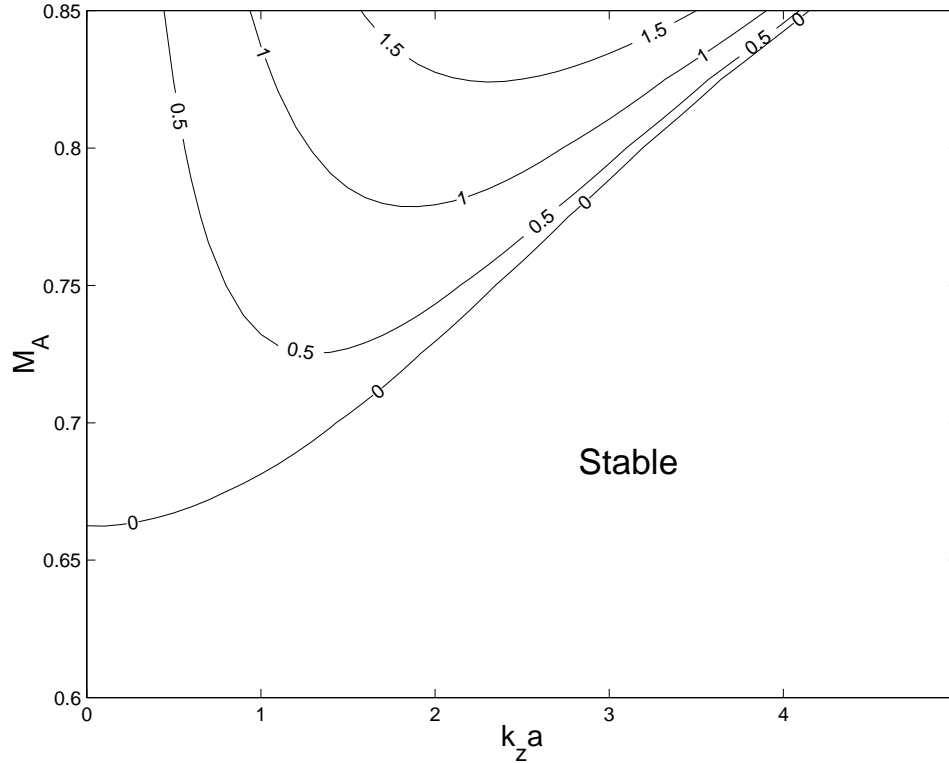


Figure 5.2: Normalized growth rates of the most unstable modes for the case $M_S = 4$, $R/a = 1/3$. The growth rate is normalized to the inverse of the sound time scale, C_S/a .

decreases all the way outward, e.g. the Couette flow, the MRI could be possible. This is certainly true. In some cases of the Couette flow, we do have found localized unstable modes about the inner wall, where the magnetic field is weak. However, for most cases this is not even possible, as the magnetic field strength increases so quickly with the radius r that no unstable mode can be found.

5.3.4 Stability over the Parameter Range

We now numerically solve the system in the general case by the shooting code. The code found no unstable modes for low M_S systems, whereas for high M_S systems

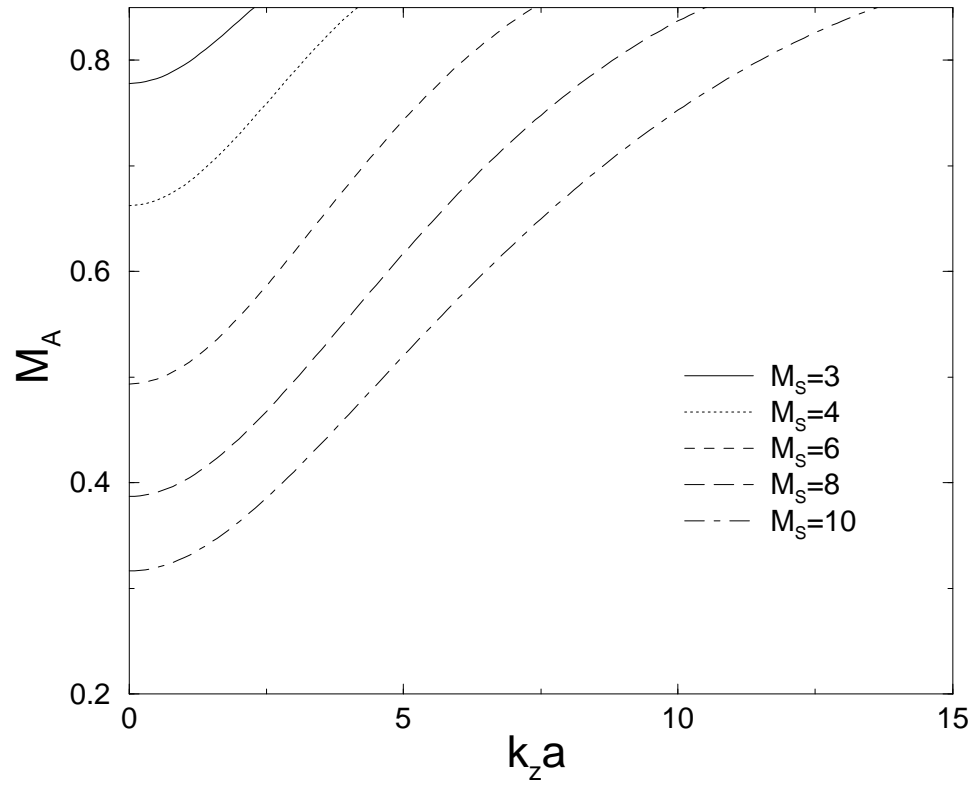


Figure 5.3: Marginal stability curves for $M_S = 3, 4, 6, 8, 10$, with $R/a = 1/3$. The region above the curve is unstable.

unstable modes were found in the region of large M_A and small k_z . Fig. 5.2 shows the contour plot of the growth rates of the most unstable mode for the case $M_S = 4$ in the parameter space of M_A and the normalized wave number $k_z a$. The system is more unstable for high M_A since the magnetic field is weaker, and is stable for short wavelengths because of the strong magnetic recovering force at short wavelengths. It is also important to see how the unstable parameter range varies with respect to different M_S . This can be done by solving the marginal stability for different M_S . Since the ω^2 of the unstable modes we found are real, we may solve for marginal stability by setting ω^2 to zero in Eq. (5.22), which gives (assume $k_z \neq 0$):

$$u'' - \left(k_z^2 + \frac{3}{4r^2} + \frac{4r\Omega\Omega'}{V_A^2} - \frac{r^2\Omega^4}{V_A^4} - \frac{r^2\Omega^4}{V_A^2 C_S^2} \right) u = 0. \quad (5.35)$$

Eq. (5.35) is a Schrödinger type eigenvalue equation of u with eigenvalue k_z^2 . If Eq. (5.35) has no positive eigenvalue k_z^2 , then the system is stable. Before we solve it numerically, a general observation can be made as follows. If we let $r \rightarrow R$, $\Omega' \rightarrow -\Omega/a$ in (5.35), and notice that $u'' \sim -(\pi/a)^2 u$ for a solution with the longest wavelength in the r direction, we have the schematic stability criterion:

$$-\frac{\pi^2}{a^2} - \frac{3}{4R^2} + \frac{4M_A^2}{Ra} + \frac{M_A^4}{R^2} + \frac{M_A^2 M_S^2}{R^2} < 0. \quad (5.36)$$

The last term of the LHS of Eq. (5.36) is the only one related to M_S . Since that term is positive and proportional to M_S^2 , a system with higher M_S is more unstable. This is consistent with our previous results that the system is unstable for all M_A and k_z in the cold limit ($M_S \rightarrow \infty$) and is completely stable in the incompressible limit ($M_S \rightarrow 0$). Fig. 5.3 depicts the marginal stability curves for different M_S , which clearly shows the enlargement of the unstable region as M_S increases.

5.4 Initial-Value Simulation

So far our conclusions were obtained by solving the linearized normal mode equation by the shooting code. However, it should be kept in mind that the normal modes

could be incomplete, and some normal modes might even be difficult to find by a shooting code, especially those solutions involving cancellation of large terms in the equation. Even without the above-mentioned problems, one still can not expect to obtain a complete answer by a shooting code. A shooting code can find some normal modes, but certainly not all — usually for a given k_z there exists infinite number of normal modes. Therefore, it is desirable to check the result by direct simulation.

For this purpose, we solved the time dependent 2D MHD equations for our basic model. The code we used is nonlinear although for this work we are only interested in linear stability. The numerical algorithm is described in detail in Ref. [28]. The code has viscosity and resistivity explicitly. In addition to those physical transports, it also has hyperviscosity (proportional to Δx^3 , where Δx is the grid size) for numerical stability. In order to have an ideal MHD equilibrium, the steady state is "frozen-in" (otherwise resistivity will flatten the magnetic field profile and viscosity will slow down the flow) and the code steps only the deviation from the steady state; therefore the non-ideal effect of the code is limited to those perturbed quantities. Periodic boundary conditions are assumed in the z direction, which quantize the allowable wavenumbers in the z axis. The steady state was initially seeded with a random perturbation of the size $10^{-4}C_S$ in u_r , u_ϕ , and u_z to see if the system goes unstable in time evolution. We wish to confirm (1) that the mode growth rate obtained by the shooting code agrees with the direct simulation in the linear stage, and (2) that the system is indeed stable in the parameter range where no unstable modes were found. To calculate the growth rate for each wavenumber from the simulation data, first we perform Fourier transformation on u_r to obtain the amplitude of each wavelength as a function of r :

$$A(k_z, r) = \int_0^L u_r(r, z) \exp(ik_z z) dz, \quad (5.37)$$

then average the log of the norm of $A(k_z, r)$ over radius:

$$\langle \ln |A| \rangle = \frac{1}{a} \int_R^{R+a} \ln |A(k_z, r)| dr. \quad (5.38)$$

Model	(r,z) Grid	L/a	M_S	M_A	Shooting Code	Simulation
1a	45×133	2π	6	0.75	unstable	unstable
1b	45×133	1.2	6	0.75	stable	stable
1c	45×133	1.3	6	0.75	unstable	unstable
1d	60×261	2π	6	0.75	unstable	unstable
2a	45×133	2π	6	0.6	unstable	unstable
2b	45×133	2	6	0.6	stable	stable
3a	45×133	2π	4	0.75	unstable	unstable
3b	45×133	2	4	0.75	stable	stable

Table 5.1: A comparison between the normal mode shooting code results and the initial-value simulation results.

By plotting $\langle \ln |A| \rangle$ with respect to time, one can then obtain the growth rate for each wavenumber by means of a least-squares fit during the linear growing period. This test has been run for various Mach numbers, Alfvén Mach numbers, elongation, and resolution. In terms of stability, the simulation results agree with the shooting code ones for all the cases we have tested, as summarized in Table 5.1.

Fig. 5.4 shows the time evolution of $\langle \ln |A| \rangle$ for the six longest wavelength modes in model 1a. According to linear analysis, $k_z a = 1$ to 5 will be unstable. The simulation shows that $k_z a = 6$ is also unstable, after $t \simeq 4$. An obvious possible reason for this is the nonlinear coupling between modes. As we can see from Fig. 5.4, the mode with $k_z a = 1$ has two stages of "linear growing", with a smaller growth rate within $t = 2$ to 5, followed by a sudden boost at $t \simeq 5$. This sudden boost also indicates nonlinear coupling. For the same reason, although the $k_z a = 5$ mode should be weakly unstable according to linear analysis, we cannot trust the "linear growth" of that mode shown in Fig. 5.4, since the behavior resembles that of $k_z a = 6$. To verify the hypothesis of nonlinear coupling, we tested the model 1b, with elongation 1.2, which limits the smallest wavenumber to $k_z a = 5.24$. According to

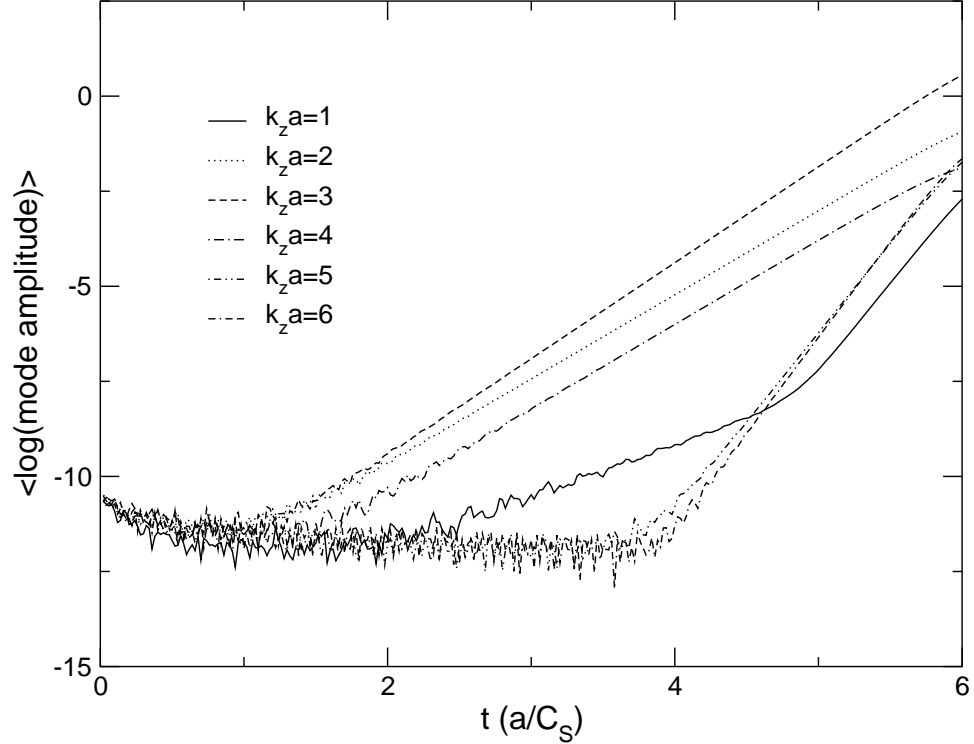


Figure 5.4: Time evolution of $\langle \ln |A| \rangle$ for various wavenumbers of model 1a.

linear analysis, this wavenumber will be stable, which is confirmed by the simulation. Model 1b has been run for $t=30$ to ensure that no slowly growing modes exist. As a comparison to model 1b, model 1c, with a slightly longer elongation 1.3, has the smallest wavenumber $k_z a = 4.83$, which is unstable according to the linear analysis. This linear growth is clearly shown in Fig. 5.5.

The mode growth rates calculated from model 1a-1c are plotted in Fig. 5.6 and compared with the growth rate from the shooting code. We found that the growth rate from simulation agrees with the shooting code result but is slightly lower, which is clearly due to the non-ideal terms in the code. To test this possibility, we have to decrease the viscosity and resistivity. This can be done in a simulation with higher resolution, which also reduces hyperviscosity. Model 1d is essentially a high resolution version of model 1a, but the resistivity and the viscosity are decreased by

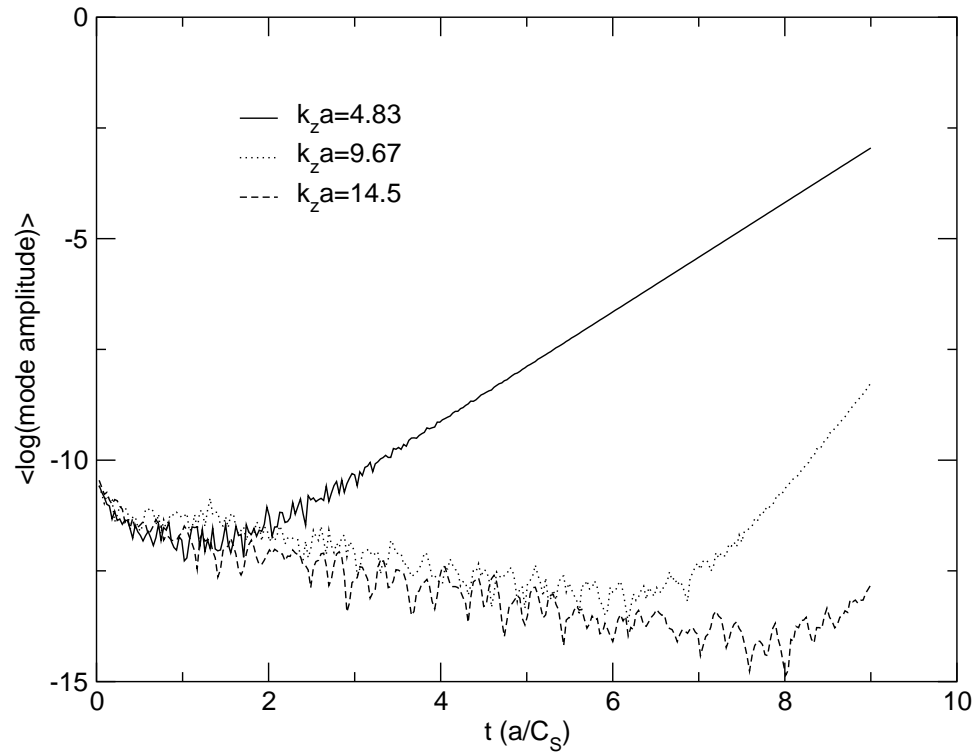


Figure 5.5: Time evolution of $\langle \ln |A| \rangle$ for various wavenumbers of model 1c. The growth of the mode $k_z a = 9.67$ is due to nonlinear coupling.

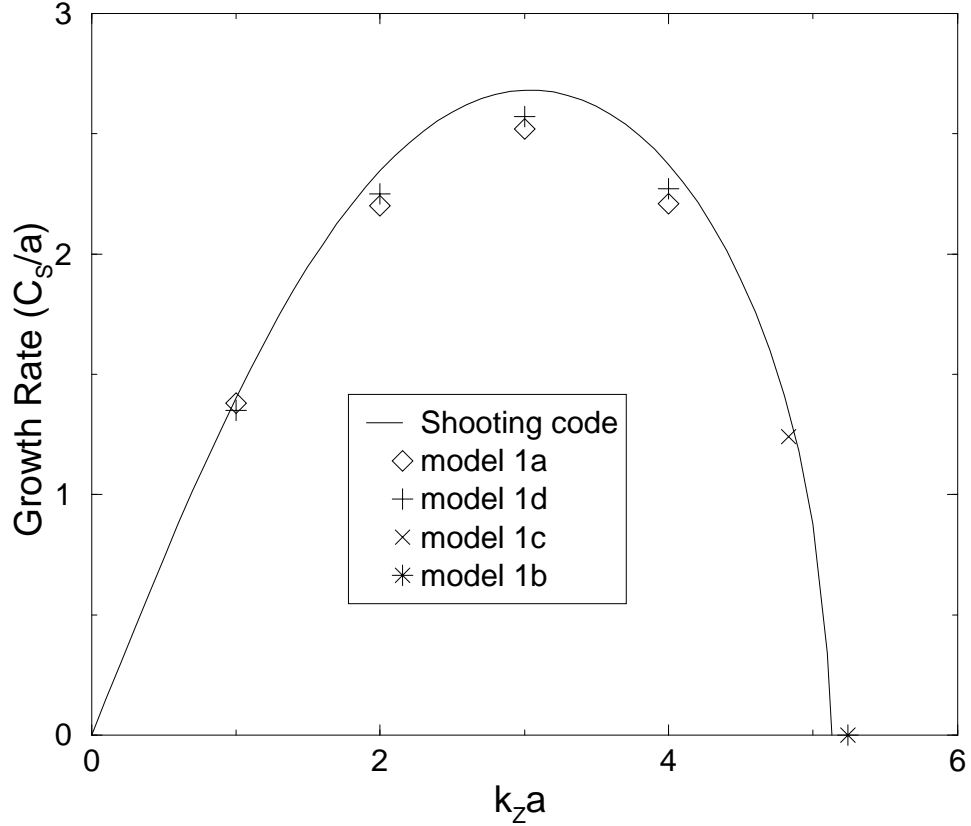


Figure 5.6: A comparison of the linear growth rate obtained by simulation and by linear analysis.

a factor of two. The resulting growth rates are closer to the ones from the shooting code, as also shown in Fig. 5.6.

The agreement between the linear analysis and the simulation lays a solid foundation for the results obtained in the previous section. In particular, the stable region found by the shooting code is indeed so.

5.5 Implications for Centrifugally Confined Plasmas

As we mentioned in the Introduction, a high β system is desirable for a fusion device. Since $\beta = 2p/B^2 = (2/\gamma)M_A^2/M_S^2$, to achieve high β we have to achieve

high M_A . As we can see from Fig. 5.3, for a plasma with $M_S = 4$, the maximum stable $M_A \simeq 0.66$, which yields $\beta \simeq 3.3\%$ ($\gamma = 5/3$ is assumed). However, the above estimate is based on infinite elongation, which allows all possible $k_z a$ down to zero. For a system with finite elongation L , we have $k_z a \geq \pi a/L$, which makes the system more stable. However, elongation only slightly affects the stability. For example, the maximum stable $M_A \simeq 0.7$ when $L/a = 2$, which is not much different from the infinite elongation case. Notice that while our previous study [33] shows that large elongation is desirable for velocity shear stabilization of the interchange instability, the present study indicates that a system with long elongation is more prone to the magnetic buoyancy instability. However, since elongation only slightly affects the maximum M_A , large elongation could be possible.

Another “knob” that could change the maximum M_A is the aspect ratio. From the force balance equation (5.11), V_A^2 scales as $aR\Omega^2$, which means M_A^2 scales as R/a . Therefore, a large aspect ratio seems to be desirable to achieve a high β system. From the magnetic buoyancy stability point of view, a large aspect ratio is also desirable. This is seen as follows. The magnetic buoyancy instability is driven by the centrifugal force $R\Omega^2$, which scales as $M_S^2 C_S^2/R$. For a centrifugally confined fusion plasma, $M_S \simeq 4$, and $T \simeq 10$ keV are required. Therefore, $M_S^2 C_S^2$ is fixed and the centrifugal force is proportional to $1/R$. For exactly the same reason, a large aspect ratio also helps the velocity shear stabilization of interchange modes, as we have shown before [32], since the interchange mode is also driven by the centrifugal force. Fig. 5.7 depicts the marginal stability curves for various M_S with aspect ratio $R/a = 1$. When compared with Fig. 5.3 for $R/a = 1/3$, the benefit of large aspect ratio is clearly evident. For $M_S = 4$, $M_A \simeq 1.05$ can be achieved, which yields $\beta \simeq 8.3\%$.

It should be mentioned that there are two limits on the achievable M_A . The first limit is set by the MHD equilibrium: from Eq. (5.11), we have $M_A^2 \lesssim R/a$. The other limit is set by the MHD stability. For a high M_S centrifugal confined

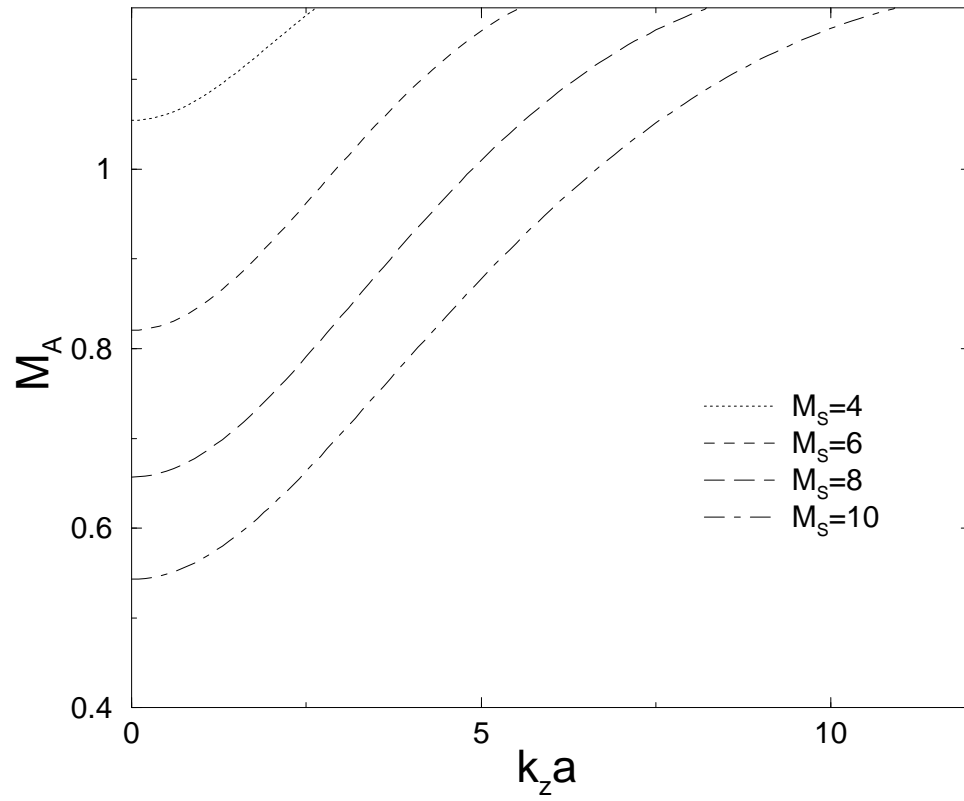


Figure 5.7: Marginal stability curves for $M_S = 4, 6, 8, 10$, with $R/a=1$.

plasma, the schematic criterion (5.36) is mainly a competition between the first term and the last term of the LHS. Hence, the stability limit is, roughly speaking, $M_A^2 \lesssim (\pi/M_S)^2(R/a)^2$. Since the equilibrium limit scales as R/a and the stability limit scales as $(R/a)^2$, it is possible that the later exceeds the former in a large aspect ratio system, and the system is stable up to the equilibrium limit. For example, a $M_S = 3$ system is stable to all M_A in the case $R/a = 1$ (Fig. 5.7), whereas it is unstable at large M_A when $R/a = 1/3$ (Fig. 5.3).

5.6 Summary and Discussion

In this Chapter, we studied the linear ideal MHD stability of a Dean flow plasma supported by an axial magnetic field. We found that the system is likely to be free of the MRI; however, the magnetic buoyancy instability could occur. The effect of aspect ratio on the MHD stability is also studied. Large aspect ratio is found to be stabilizing for the centrifugal confinement scheme. We conclude our study by discussing some issues and open questions in the present study:

1. We considered only axisymmetric stability in this study. The primary manifestation of the MRI is two dimensional [2, 4], as is the Parker instability [54]. Thus, our axisymmetric stability is an informative starting point. In addition, for $M_A \ll 1$, we have done a fully 3D stability of the centrifuge [36, 32] and found stability for large M_S . With the foregoing information, a fairly clear picture of the parameter space can be discerned. To complete this picture, however, an $M_A \sim 1$, 3D stability analysis needs to be done.
2. In this Chapter, we model a centrifugally confined plasma via the Dean flow model, which certainly lacks some important features. In addition to the special choices for the density, the pressure, and the flow profile, an obvious omission is the lack of the curved magnetic field, which is essential to the centrifugal confinement scheme. At first sight, curved field lines would seem

more prone to the buoyancy instability. However, whether the buoyancy instability is catastrophic is not clear. It is well known in astrophysics that the plasma eventually saturates to several localized clumps after the onset of the Parker instability [51], whereas the MRI usually results in turbulent behavior [4]. Since we have shown that the MRI is unlikely, saturation is expected. In fact, we have run the nonlinear simulation beyond the linear growing stage. For $M_S = 4$, saturation was achieved, and the final state has localized plasma clumps that in fact look like centrifugally confined plasmas. For higher M_S , the plasma was compressed to a thin disk that made running the simulation rather difficult. A full discussion of this issue is beyond the scope of this Chapter. However, if the system indeed saturates, the buoyancy instability might not be catastrophic, and the estimate of the maximum M_A in the previous section may be pessimistic. It should also be mentioned that Ref. [51] assumed perfect “frozen-in” of the magnetic field. If the system is allowed to last longer than the resistive time scale, as one would expect for a steady state fusion device, then we can no longer neglect the effect of resistivity. To be sure, the numerical simulation in Ref. [43] shows that on the resistive time scale, after the onset of the Parker instability, the magnetic field relaxes to a nearly uniform field, the plasma is supported against gravity almost by the pressure gradient only, and the structure generated by the initial clumping disappears. From the result of Chapter 3, this is also what one would expect for a resistive Dean flow, if there is no particle source. Even if the external field is curved, the situation will be essentially the same. However, with particle sources to drive the magnetic field from relaxing to nearly a vacuum field, a steady state with saturated clumps could be anticipated. In the next Chapter, we will touch upon a few of the foregoing issues, although a complete understanding is still lacking.

Chapter 6

Nonlinear Development of the Parker Instability

In Chapter 5 we studied the linear stability of a high β Dean flow, and established that the MRI is unlikely, while the Parker instability could occur. Of greater interest is the nonlinear behavior of the Parker instability. This has been studied quite extensively in the astrophysical context with gravity [51, 44, 49]. In this Chapter we present simulations of the nonlinear behavior of the Parker instability in a rotating plasma. The equations evolved are MHD equations with simple transport [36], except that an isothermal equation of state is assumed for simplicity. Perfect conducting hard wall boundary conditions are assumed in the radial direction.

The first simulation was done in the simplest setting, i.e., a 2D Dean flow. Dean flow is annular, azimuthal flow between two concentric cylinders with no-slip boundary conditions. We examine this case for a plasma with an axial magnetic field. The inner and outer radii were taken to be 0.45 and 1.45. The elongation of the simulation box is 6, and periodic boundary conditions were assumed in the axial direction. A constant azimuthal force was applied to drive the flow. A one dimensional (1D) steady state was first established by putting in particle sources and sinks. The steady state had $M_S \simeq 4$ and $M_A \simeq 1$. Note this equilibrium has an effective gravity from the centrifugal force pointing radially outward. This force also makes the plasma lean against the magnetic field, compressing it some and setting up a situation for a Parker type instability. The steady state was then seeded with 2D random noise. An instability resulted and a plasma clump was spontaneously

formed (Fig. 6.1). The plasma clump first formed as a highly concentrated density peak and the magnetic field was significantly bent ($t=45$). The magnetic tension then straightened the magnetic field line slightly; as the system approached a steady state, the density peak became milder than it was initially ($t=150$). This simulation has been repeated for different elongation. For longer elongation, more than one clump could form in the beginning. The separation between these initial clumps was determined by the wavelength of the fastest growing mode. However, these initial clumps usually recombined to form larger clumps. As the system approached a steady state, there was always only a single clump left in the simulation box for all cases we have tried. This suggests that the single clump state is some kind of the lowest energy state, although the latter hypothesis remains to be checked out.

The Dean flow simulation is, of course, not realistic as applied to a centrifugally confined plasma. In particular, it possesses translational symmetry along the axial direction which is absent in any real system. To better model the real system, a second simulation was done in a highly elongated, slightly curved magnetic mirror field. In this system there is no 1D equilibrium to start with, therefore the Parker instability can only be observed until some thresholds are crossed, as one constantly changes the system parameters. Two simple scenarios can be constructed: (1) Start from a low density, then keep increasing the density by particle sources, until the density exceeds the critical value for instability. (2) Hold the total particle number fixed, and keep increasing the rotation speed until the critical speed is exceeded. Fig. 6.2 shows the time sequence of a simulation in the second scenario. Up-down symmetry was assumed in this simulation so only half of the system is shown in the figure. The system was started with a flat density and with no rotation. As the plasma was spun up by the applied force, centrifugal forces started to push the plasma away from the mirror throat, resulting in a centrifugally confined state ($t=30,150$). However, as the plasma rotation exceeded the critical speed, a highly localized plasma clump suddenly formed, first off-center ($t=210$), then shifted toward

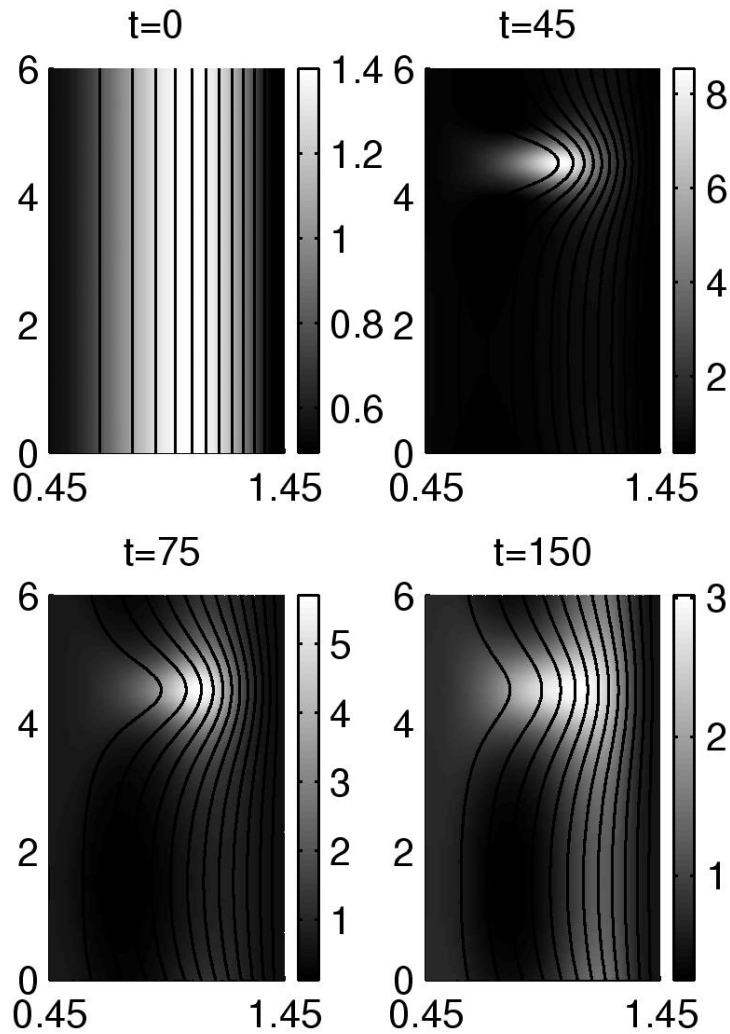


Figure 6.1: The Parker instability in a Dean flow. The density profile is shown in gray scale, with magnetic fields overlaid. Notice that the two axes are not to scale. Also notice that different color codes are used in different time slices. Times are shown on the Alfvénic time scale.

the center of the mirror and finally settled down there ($t=300$).

Both simulations were subsequently repeated in 3D. The single clump state of the first simulation was shown to be unstable to 3D perturbations, while the 3D version of the second simulation showed no difference from the 2D one. No general conclusion can be drawn from these simulation at this stage. As discussed in Chapter 2–4, even in low β systems, the stability of electrostatic azimuthal modes already depends on several factors, e.g., the density and the pressure stratification and the flow profile. In high β systems with electromagnetic modes, the stability will be conceivably more complicated.

It is evident there is a similarity between the Parker instability and centrifugal confinement. In the centrifugal confinement scheme the curved field is externally imposed; the plasma is then forced to clump in the central mirror portion by centrifugal forces. The Parker instability, however, can be viewed as leading to such clumping as an end result. In particular, an initially axially uniform plasma in a collinear magnetic field can spontaneously clump, bending the field lines where it clumps to accentuate the clumping. The resulting state is highly suggestive of centrifugal confinement. The question arises if this phenomenon can aid centrifugal confinement, if there is a self-organized state. This issue is not fully understood at present. Preferred wavelengths of the initial clumping and final clumping scales need better study. Relaxation to lowest energy state calculations have been done for the Parker instability [51] and these are indeed suggestive of self-organization. This topic is currently under investigation.

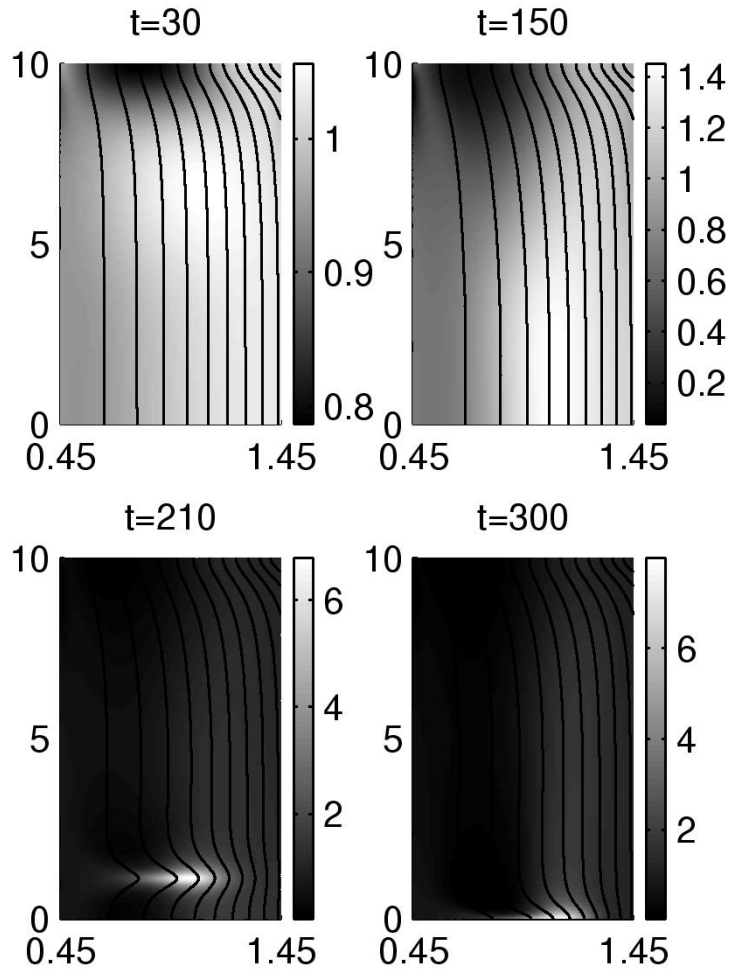


Figure 6.2: The Parker instability in a highly elongated, slightly curved mirror field. Only half of the system is shown. As the rotation exceeded the critical speed, a plasma clump suddenly formed, first off-center ($t=210$), then shifted toward the center and finally settled down there ($t=300$). Times are shown in the Alfvénic time scale.

Chapter 7

Summary and Outlook

In this dissertation we have gathered together and put into context our work on the MHD equilibrium and stability of centrifugally confined plasmas. We can now summarize our current understanding as follows. (1) Interchange modes could be stabilized by the velocity shear. A high sonic Mach number M_S is needed to stabilize the pressure gradient driven interchanges; in an elongated system, the M_S requirement can be lowered. The KH instability is ideally stable provided the generalized Rayleigh's Inflexion criterion is satisfied. (2) Particle sources are needed to attain a magnetically confined steady state. The placement of particle sources determines the steady state density profile. Since the density profile is crucial, both for interchanges and the KH instability, particle sources should be judiciously placed. In this sense, particle sources can be regarded as an additional "knob" to optimize the stability of the system. (3) Low density plasmas with $V_A \sim c$ are more stable to interchanges, essentially due to the fact that the electromagnetic field acts as an effective mass, therefore increases the inertia by a factor of $(1 + V_A^2/c^2)$. The effect of the expected occurrence of low density plasma near the mirror throats of a centrifugally confined plasma is, however, negligible after averaging over a flux tube. A pronounced effect is possible only if $V_A \sim c$ throughout the whole system. (4) In a high β system, an instability resembling the classical Parker instability could occur. The MRI mechanism, on the other hand, is insufficient to destabilize the system. Simulations show the formation of highly localized plasma clumps after the onset of

the Parker instability.

Several issues remain to be resolved. First, the full implication of the Parker instability is still unclear. Because of the similarity between centrifugal confinement and the Parker instability, the Parker instability may not be destructive to the centrifugally confined system; rather, it might simply mean a significant sudden change to the configuration of the system. One may even regard the resulting plasma clumps as a self-organized centrifugally confined state. Even though the plasma seems to self-organize into clumps in 2D, whether or not the clumped 2D state could withstand 3D perturbations is not clear. A systematic study of the 3D Parker instability is needed.

Second, the KH instability caused by non-ideal effects is an unexplored realm for centrifugally confined plasmas. In unmagnetized fluids, it is well-known that unstable modes exist at high Reynolds number and long wavelengths [22]. However, transition to turbulence was extensively observed at much lower Reynolds number than theoretically predicted [64]. The transition to turbulence, however, usually involves 3D structures; that means a strong magnetic field would significantly affect the result. To be sure, the interplay of velocity shear and magnetic shear is one of the intriguing topics. It has been proposed to use magnetic shear to aid velocity shear stabilization and to suppress the non-ideal KH instability [23]. Interestingly enough, the combination of velocity shear and magnetic shear, both thought to be stabilizing, sometimes may be destabilizing [41, 42]. The validity of this proposal has to be further assessed.

Third, a more realistic model of non-ideal effects should be incorporated, as that could have significant effect on velocity shear stabilization. So far our studies are limited to very simple forms for the non-ideal effects; more sophisticated physics should be included for a better understanding. Recently, the finite Larmor radius effect has been taken into account in velocity shear stabilization calculations ¹. Work

¹S.-W. Ng, private communication.

along these lines is in progress.

An experiment to investigate MHD stability and other basic physics of centrifugally confined plasmas is currently ongoing at the University of Maryland [23]. Preliminary results from the Maryland Centrifugal Experiment (MCX) indicate a confined plasma which seems to be quiescent on time scales much longer than the MHD instability time scale. Further experimental and theoretical studies should be illuminating.

The MCX project is still in its early stage. As new experimental data are coming out and theories are developing, it is always a good idea to look back to what have been done before on similar ideas. Besides those references cited in the main text, here we compile a short list of literature related to centrifugal confinement. Hopefully this will be useful to later workers. The idea of centrifugal confinement stems from the 1950s. The review article of Lehnert [48] is a good summary of early attempts before the 1970s. The Russian research during the 1970s to the early 1990s can be found in Refs. [9, 5, 66, 12, 13, 1]. The famous Pastukhov factor on longitudinal losses was first derived in Ref. [55]. Longitudinal losses in a rotating mirror is discussed in a review article of Pastukhov, Ref. [56].

Appendix A

Electric Current Driven Cylindrical Hartmann Flow

In this Appendix we demonstrate that with an external axial magnetic field, a steady state rotating MHD flow can be driven by an externally supplied electric current. The essential idea is sketched in Fig. A.1, which depicts an electrically conducting fluid contained in an annular duct. The inner and outer walls of the duct are conducting, while the top and bottom walls are insulating. An axial magnetic field is applied, and an external voltage (or current) supply drives a current within the conducting fluid. The azimuthal force $\mathbf{J} \times \mathbf{B}/c$ drives the fluid against the viscous deceleration, hence a steady flow can be achieved. Historically, Hartmann was the first to investigate theoretically and experimentally the MHD flow in the gap between two parallel plates with an external magnetic field [29]. Hence, various kinds of MHD channel flows with an external magnetic field are generally referred to as the Hartmann flow in literatures [50, 61, 52]. We follow this convention here, even though the flow we are going to discuss is not the original one investigated by Hartmann.

A.1 Governing Equations

To determine the solution within the channel, we have to specify how the external circuit is connected. This will, in general, be complicated, although the solution may not strongly depend on the detail of the circuit. For example, if the two

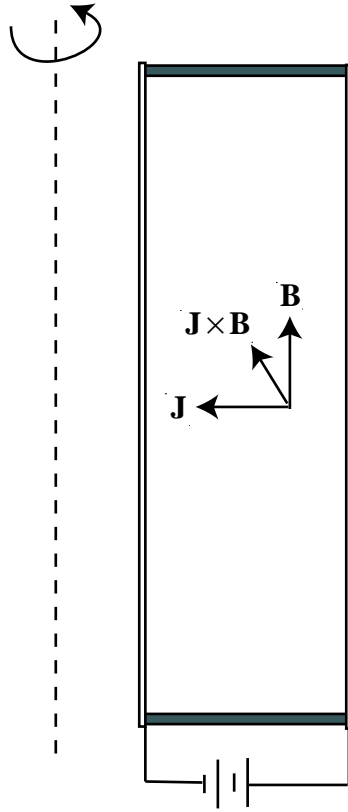


Figure A.1: Sketch of an electric current driven cylindrical Hartmann flow.

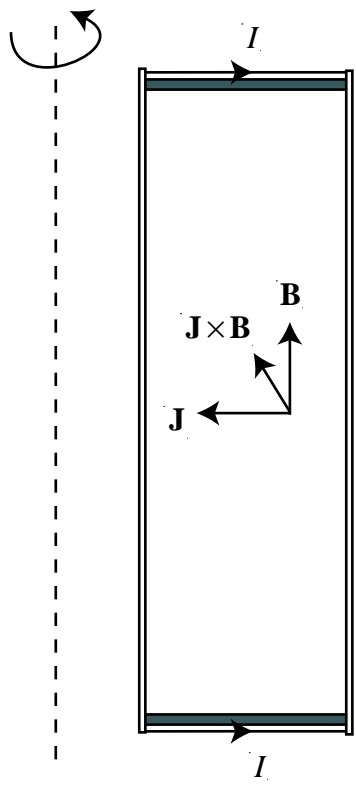


Figure A.2: Sketch of the "simplified" electric current driven cylindrical Hartmann flow.

conducting walls are connected by a wire, which breaks the azimuthal symmetry, then we have to solve a 3D problem. To avoid the complication, we consider a simplified case as depicted in Fig. A.2. Immediately outside of the insulating top and bottom walls are two thin current sheets, each with a total current I . The inner and outer conducting walls are assumed to be perfect. For simplicity, we assume an incompressible conducting fluid with a constant density. This is a good approximation for liquid metals, but a plasma would be considerably more complicated. The governing equations of steady state are:

$$\rho \mathbf{u} \cdot \nabla \mathbf{u} = -\nabla p + \mathbf{J} \times \mathbf{B}/c + \rho \nu \nabla^2 \mathbf{u}, \quad (\text{A.1})$$

$$\mathbf{E} = -\frac{\mathbf{u} \times \mathbf{B}}{c} + \eta \mathbf{J}, \quad (\text{A.2})$$

$$\mathbf{J} = \frac{c}{4\pi} \nabla \times \mathbf{B}, \quad (\text{A.3})$$

$$\nabla \times \mathbf{E} = 0, \quad (\text{A.4})$$

$$\nabla \cdot \mathbf{B} = 0, \quad (\text{A.5})$$

$$\nabla \cdot \mathbf{u} = 0, \quad (\text{A.6})$$

where standard notations are used. In the following discussion we use (r, ϕ, z) to denote the cylindrical coordinates. We look for a steady state solution with $\mathbf{u} \simeq u_\phi \hat{\phi}$, and $\mathbf{B} \simeq B_0 \hat{z} + B_\phi \hat{\phi}$, where $B_0 = \text{const}$ is the external field. The current density within the fluid is

$$\mathbf{J} = \frac{c}{4\pi} \nabla \times \mathbf{B} = \frac{c}{4\pi} \nabla(rB_\phi) \times \frac{\hat{\phi}}{r}. \quad (\text{A.7})$$

From Eq. (A.7) one can readily see that rB_ϕ is the stream function of the current density — the current flows along contour lines of rB_ϕ . The governing equations for B_ϕ and u_ϕ are given by the ϕ component of the force balance equation (A.1):

$$\frac{B_0}{4\pi} \frac{\partial B_\phi}{\partial z} + \rho \nu \left(\frac{\partial}{\partial r} \left(\frac{1}{r} \frac{\partial(ru_\phi)}{\partial r} \right) + \frac{\partial^2 u_\phi}{\partial z^2} \right) = 0, \quad (\text{A.8})$$

and the ϕ component of Eq. (A.4):

$$\frac{B_0}{c} \frac{\partial u_\phi}{\partial z} + \frac{\eta c}{4\pi} \left(\frac{\partial}{\partial r} \left(\frac{1}{r} \frac{\partial(rB_\phi)}{\partial r} \right) + \frac{\partial^2 B_\phi}{\partial z^2} \right) = 0. \quad (\text{A.9})$$

The boundary conditions have to be specified. We assume no-slip boundary condition $u_\phi = 0$ at walls. The top and bottom walls are insulators, which means no current can flow into the walls. Therefore, we require $J_z = 0$. The inner and outer walls are perfect conductor, which also implies $E_z = \eta J_z = 0$. Therefore, the boundary condition for B_ϕ is

$$\frac{\partial(rB_\phi)}{\partial r} = 0. \quad (\text{A.10})$$

It can be deduced by symmetry and Eq. (A.10) that $rB_\phi|_{\text{top}} = -rB_\phi|_{\text{bottom}} = \text{const}$. The constant can be determined by the fact that in a steady state, the total current across the flow should be equal to the total external current $2I$:

$$-\int_{-L}^L 2\pi r J_r = \frac{c}{2}(rB_\phi)|_{-L}^L = 2I, \quad (\text{A.11})$$

where we assume that the top and the bottom walls locate at $z = \pm L$; therefore, we have

$$rB_\phi|_{z=L} = -rB_\phi|_{z=-L} = 2I/c. \quad (\text{A.12})$$

A.2 Numerical Solutions

First we nondimensionalize the governing equations by normalizing lengths to L , magnetic fields to B_0 , and speeds to U , where

$$U \equiv \frac{B_0 c}{4\pi} \sqrt{\frac{\eta}{\rho\nu}}. \quad (\text{A.13})$$

Then Eqs. (A.8) and (A.9) become

$$H_a \frac{\partial B_\phi}{\partial z} + \frac{\partial}{\partial r} \left(\frac{1}{r} \frac{\partial(ru_\phi)}{\partial r} \right) + \frac{\partial^2 u_\phi}{\partial z^2} = 0, \quad (\text{A.14})$$

and

$$H_a \frac{\partial u_\phi}{\partial z} + \frac{\partial}{\partial r} \left(\frac{1}{r} \frac{\partial(rB_\phi)}{\partial r} \right) + \frac{\partial^2 B_\phi}{\partial z^2} = 0, \quad (\text{A.15})$$

where

$$H_a \equiv \frac{B_0 L}{c\sqrt{\rho\nu\eta}} \quad (\text{A.16})$$

is the Hartmann number. The boundary condition (A.12) becomes

$$rB_\phi|_{z=1} = -rB_\phi|_{z=-1} = 2I/cLB_0 \equiv K. \quad (\text{A.17})$$

Other boundary conditions $u_\phi = 0$ and $\partial_r(rB_\phi) = 0$ remain unchanged. It can be readily seen that both B_ϕ and u_ϕ are proportional to K . Therefore, without loss of generality, we let $K = 1$ in the following discussion.

We numerically solve Eqs. (A.14) and (A.15) by a Chebyshev collocation method. Without going into the detail, interested readers are referred to Refs. [63, 10] for excellent accounts of the method. We choose the inner and outer radii to be 0.5 and 1.5 in the normalized coordinate. Fig. A.3 to Fig. A.6 show the numerical solutions of rB_ϕ and u_ϕ for $H_a = 1, 10, 50, 100$. For smaller H_a (Fig. A.3 and Fig. A.4), the current is more or less uniformly spread through the whole volume, and the flow speed varies smoothly. At higher H_a (Fig. A.5 and Fig. A.6), two thin boundary layers (the so-called Hartmann layers) form at the top and the bottom, in which the flow speed drops sharply to satisfy the no-slip boundary condition. Another two less thin boundary layers (the so-called side layers) also appear near the side walls. The thickness of the Hartmann layer scales as $1/H_a$, while the thickness of the side layer scales as $1/\sqrt{H_a}$ [52]. Within the bulk flow, the flow speed is nearly z -independent, in accordance with the law of isorotation $\mathbf{B} \cdot \nabla(u_\phi/r) = 0$ of the ideal MHD. Notice that most current flows through the boundary layers in high H_a cases.

Transforming back to the dimensional form, we have

$$[u_\phi] = \frac{I}{2\pi L} \sqrt{\frac{\eta}{\rho\nu}} u_\phi, \quad (\text{A.18})$$

where the square bracket in the left-hand-side is used to denote dimensional quantities. Now suppose we vary B_0 while keep everything else fixed. One may naively think that $[u_\phi]$ will be proportional to B_0 , since the driving force $\sim IB_0/c$. That is found not to be the case. For example, the maximum of $[u_\phi]$ at $H_a = 100$ is less than twice as large as that at $H_a = 10$ (see the captions of Fig. A.4 and Fig.

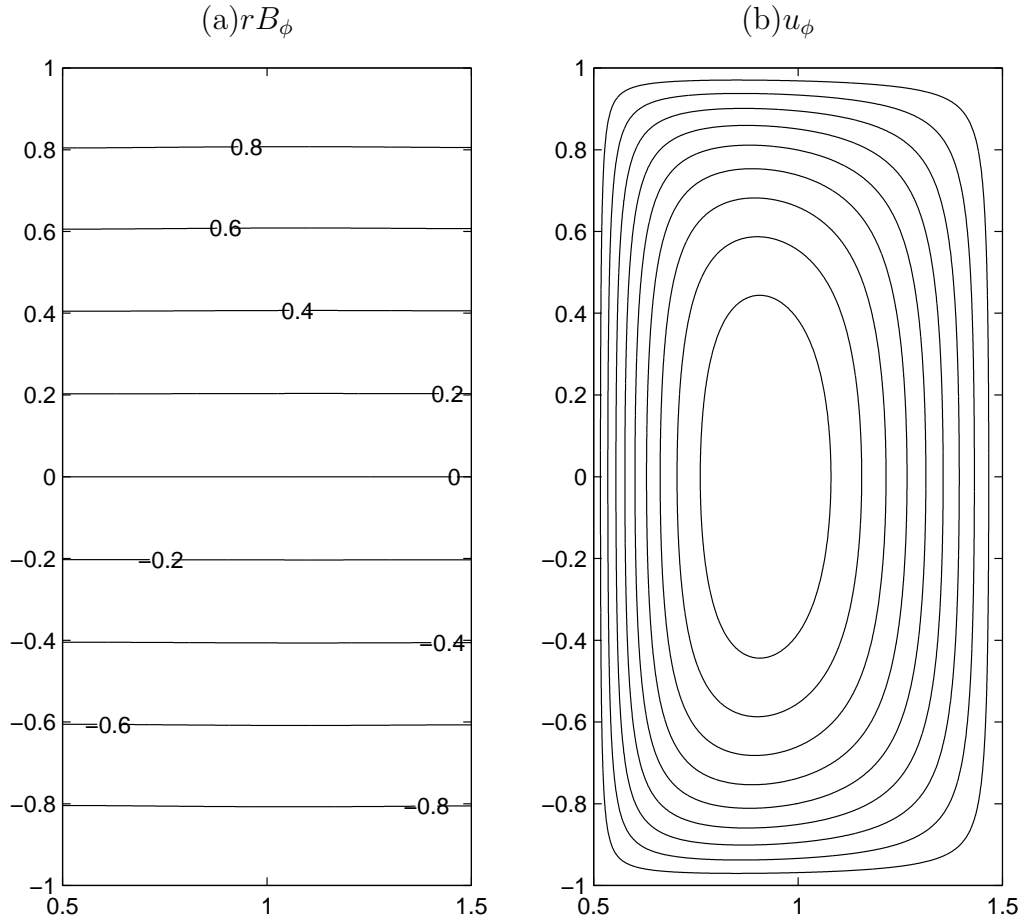


Figure A.3: The solution for $H_a = 1$. Panel (a) shows contours of rB_ϕ , which are also current paths. Panel (b) shows contours of u_ϕ . The contours (from the outside to the inside) correspond to 0.1, 0.2, ..., 0.9 of the peak value of u_ϕ , which is 0.11.

A.6). In this case an increase in B_0 by a factor of 10 only increases u_ϕ by a factor of less than 2. Apparently this is due to the fact that most current flows through the boundary layers when H_a is large, therefore is ineffective to drive the bulk flow. In fact, one can show from boundary layer analysis that $u_\phi \rightarrow 1/r$ in the bulk flow as $H_a \rightarrow \infty$; that means that $\max[u_\phi] \rightarrow (I/2\pi[r_i])\sqrt{\eta/\rho\nu}$ as $B_0 \rightarrow \infty$, where $[r_i]$ is the inner radius of the duct.

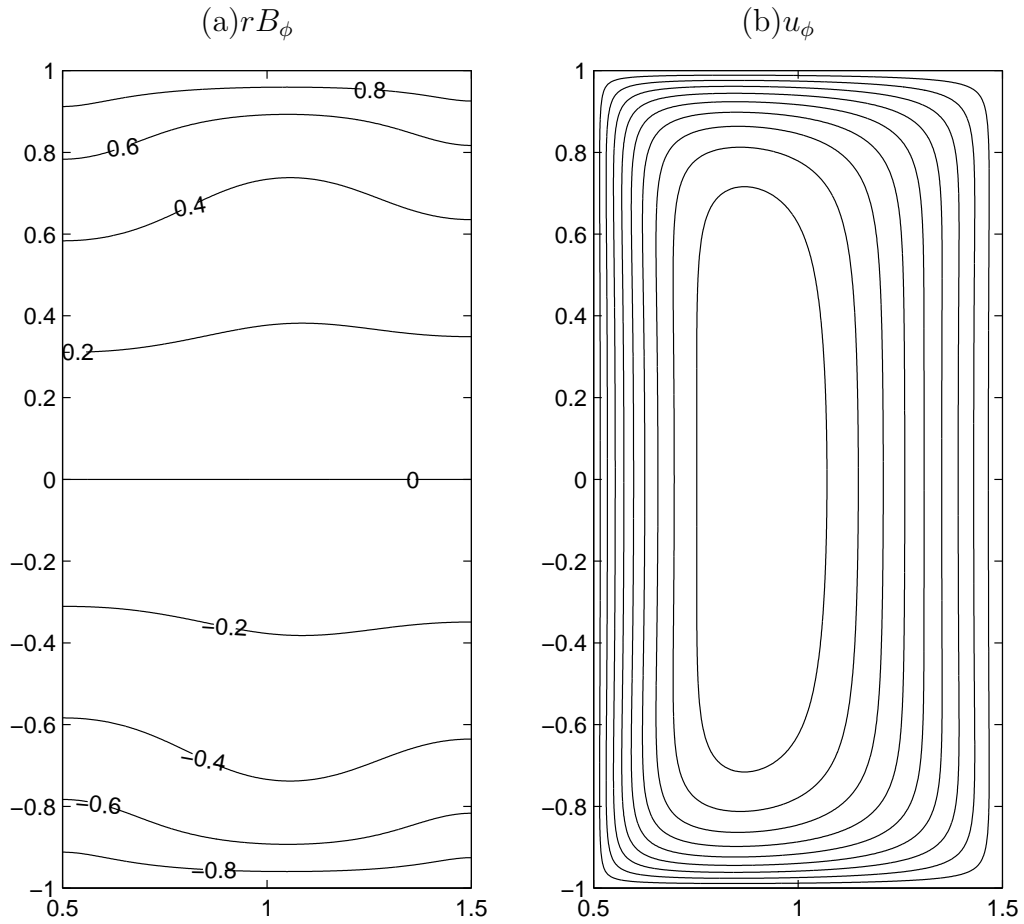


Figure A.4: The solution for $H_a = 10$. Panel (a) shows contours of rB_ϕ , which are also current paths. Panel (b) shows contours of u_ϕ . The contours (from the outside to the inside) correspond to 0.1, 0.2, ..., 0.9 of the peak value of u_ϕ , which is 0.67.

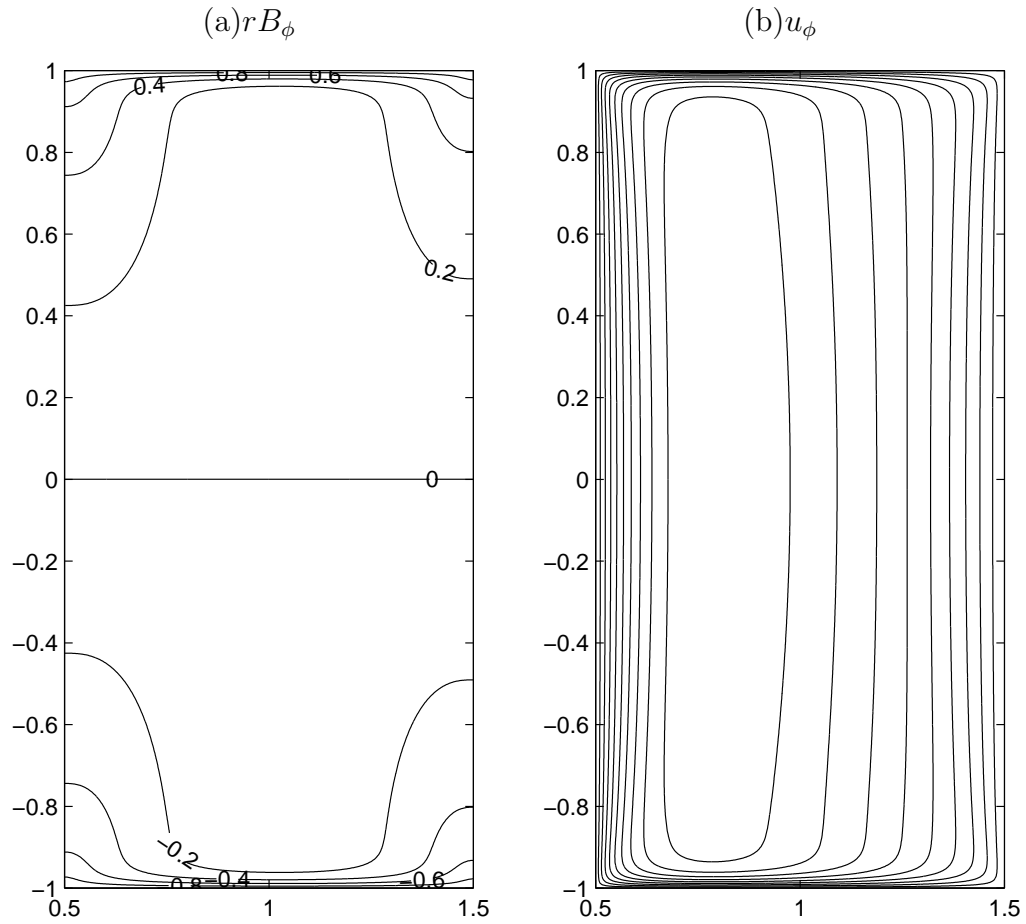


Figure A.5: The solution for $H_a = 50$. Panel (a) shows contours of rB_ϕ , which are also current paths. Panel (b) shows contours of u_ϕ . The contours (from the outside to the inside) correspond to 0.1, 0.2, ..., 0.9 of the peak value of u_ϕ , which is 1.12.

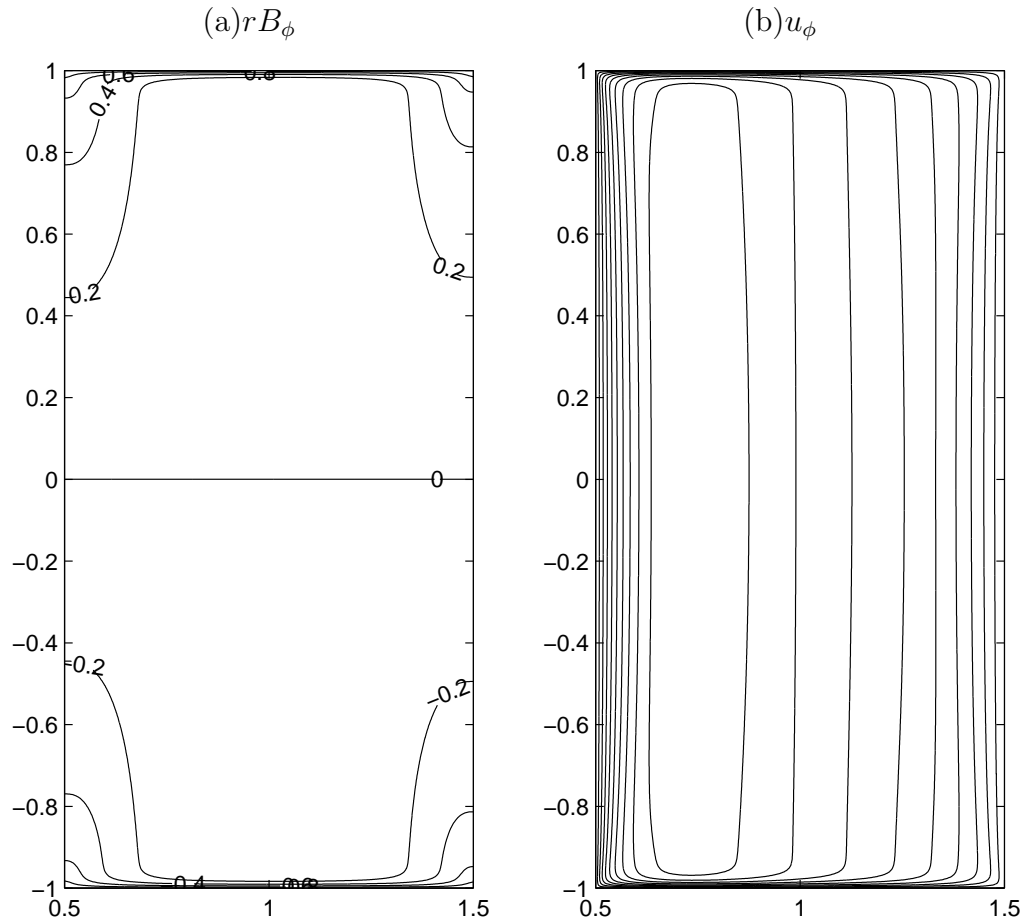


Figure A.6: The solution for $H_a = 100$. Panel (a) shows contours of rB_ϕ , which are also current paths. Panel (b) shows contours of u_ϕ . The contours (from the outside to the inside) correspond to 0.1, 0.2, ..., 0.9 of the peak value of u_ϕ , which is 1.26.

A.3 Remark on Secondary Flow

As a final remark, it should be mentioned that we have neglected the effect of the secondary flow in Eqs. (A.8) and (A.9). The presence of the secondary flow can be seen from the poloidal component of the momentum equation (A.1). Suppose there is no secondary flow, i.e., $\mathbf{u}_\perp = 0$ (the \perp denotes the poloidal component of a vector), and $\mathbf{B} = B_0\hat{z} + B_\phi\hat{\phi}$, then we have:

$$-\rho\frac{u_\phi^2}{r}\hat{r} = -\nabla_\perp\left(p + \frac{B_\phi^2}{8\pi}\right) - \frac{B_\phi^2}{4\pi r}\hat{r}. \quad (\text{A.19})$$

Taking the curl of Eq. (A.19) gives

$$\frac{\partial}{\partial z}\left(\rho\frac{u_\phi^2}{r} - \frac{B_\phi^2}{4\pi r}\right) = 0, \quad (\text{A.20})$$

which is in general not satisfied by the solution of Eqs. (A.8) and (A.9). Therefore, the unbalanced force in the primary flow drives a poloidal secondary flow \mathbf{u}_\perp , which, in conjunction with the external magnetic field, drives a toroidal current J_ϕ . Neglecting the secondary flow needs further justification. For most liquid metals, the magnetic Prandtl number, $P_m = \eta c^2/4\pi\nu \ll 1$. Assuming that, one can estimate that

$$\frac{u_\perp}{u_\phi} \sim \sqrt{\rho\nu\eta}\frac{I}{B_0^2 r^2}\frac{\eta c^2}{\nu} \sim \frac{1}{H_a P_m}\frac{B_\phi L}{B_0 r}. \quad (\text{A.21})$$

The secondary flow is negligible when $u_\phi \gg u_\perp$.

Appendix B

Linearization of Eqs. (4.50)–(4.53)

First we set up a convenient coordinate system for this problem and derive some useful identities. Since \mathbf{B} is the external field which satisfies $\nabla \times \mathbf{B} = 0$, we can express \mathbf{B} in terms of a potential λ as:

$$\mathbf{B} = -\frac{1}{r}\hat{\zeta} \times \nabla\psi = \nabla\lambda. \quad (\text{B.1})$$

Therefore, (ψ, ζ, λ) forms a right-handed orthogonal coordinate system. In this coordinate system,

$$\partial_\psi = \frac{1}{|\nabla\psi|^2} \nabla\psi \cdot \nabla = \frac{1}{r^2 B^2} \nabla\psi \cdot \nabla, \quad (\text{B.2})$$

$$\partial_\lambda = \frac{1}{|\nabla\lambda|^2} \nabla\lambda \cdot \nabla = \frac{1}{B^2} \nabla\lambda \cdot \nabla, \quad (\text{B.3})$$

and line element ds is expressed as

$$ds^2 = \frac{1}{r^2 B^2} d\psi^2 + r^2 d\zeta^2 + \frac{1}{B^2} d\lambda^2. \quad (\text{B.4})$$

From Eq. (B.4), it follows from standard vector analysis [26] that for any scalar f and vector \mathbf{A} ,

$$\nabla f = rB\partial_\psi f \hat{\psi} + \frac{\partial_\zeta f}{r} \hat{\zeta} + B\partial_\lambda f \hat{\lambda}, \quad (\text{B.5})$$

$$\nabla \cdot \mathbf{A} = B^2 \partial_\psi \left(\frac{r}{B} A_\psi \right) + \frac{1}{r} \partial_\zeta A_\zeta + B^2 \partial_\lambda \left(\frac{A_\lambda}{B} \right), \quad (\text{B.6})$$

$$\begin{aligned}\nabla \times \mathbf{A} &= \frac{B}{r} \left(\partial_\zeta \left(\frac{A_\lambda}{B} \right) - \partial_\lambda (rA_\zeta) \right) \hat{\psi} + rB^2 \left(\partial_\lambda \left(\frac{A_\psi}{rB} \right) - \partial_\psi \left(\frac{A_\lambda}{B} \right) \right) \hat{\zeta} \\ &\quad + B \left(\partial_\psi (rA_\zeta) - \partial_\zeta \left(\frac{A_\psi}{rB} \right) \right) \hat{\lambda},\end{aligned}\tag{B.7}$$

$$\nabla^2 f = B^2 \partial_\psi (r^2 \partial_\psi f) + \frac{\partial_\zeta^2 f}{r^2} + B^2 \partial_\lambda^2 f\tag{B.8}$$

where the hat $\hat{\cdot}$ denotes the unit vector along each coordinate. Notice that $\hat{\lambda} = \hat{b}$. From (B.6), we have

$$\langle \nabla \cdot \mathbf{A} \rangle = \int \frac{d\lambda}{B^2} \nabla \cdot \mathbf{A} = \partial_\psi \langle rBA_\psi \rangle + \partial_\zeta \langle A_\zeta/r \rangle,\tag{B.9}$$

provided that $\hat{b} \cdot \mathbf{A}$ vanishes at both ends of a field line. A useful identity of the curvature vector $\boldsymbol{\kappa} = \hat{b} \cdot \nabla \hat{b}$ is

$$\begin{aligned}\boldsymbol{\kappa} \cdot \nabla \psi &= (\hat{b} \cdot \nabla \hat{b}) \cdot \nabla \psi = (-\hat{b} \times \nabla \times \hat{b}) \cdot \nabla \psi = \left(-\hat{b} \times \nabla \times \left(\frac{\mathbf{B}}{B} \right) \right) \cdot \nabla \psi \\ &= \left(\frac{\hat{b}}{B} \times (\nabla B \times \hat{b}) \right) \cdot \nabla \psi = \frac{\nabla \psi \cdot \nabla B}{B} = r^2 B \partial_\psi B,\end{aligned}\tag{B.10}$$

where we have made use of $\nabla \times \mathbf{B} = 0$ at the fourth step. From (B.10) we can prove another useful identity:

$$\langle \partial_\psi f \rangle = \int \frac{d\lambda}{B^2} \partial_\psi f = \int d\lambda \left(\partial_\psi \left(\frac{f}{B^2} \right) + \frac{2f}{B^3} \partial_\psi B \right) = \partial_\psi \langle f \rangle + \left\langle \frac{2f \boldsymbol{\kappa} \cdot \nabla \psi}{r^2 B^2} \right\rangle.\tag{B.11}$$

Linearization of (4.50) yields

$$\partial_t \tilde{\rho} + \Omega \partial_\zeta \tilde{\rho} + \tilde{\mathbf{u}} \cdot \nabla \rho + \rho \nabla \cdot \tilde{\mathbf{u}} = 0,\tag{B.12}$$

where

$$\tilde{\mathbf{u}} = \tilde{u}_\parallel \hat{b} + (\hat{b}/B) \times \nabla \tilde{\phi}.\tag{B.13}$$

By using

$$\begin{aligned}
\nabla \cdot \tilde{\mathbf{u}} &= \hat{b} \cdot \nabla \tilde{u}_{\parallel} + \tilde{u}_{\parallel} \nabla \cdot \left(\frac{\mathbf{B}}{B} \right) + \nabla \tilde{\phi} \cdot \nabla \times \left(\frac{\mathbf{B}}{B^2} \right) \\
&= \hat{b} \cdot \nabla \tilde{u}_{\parallel} + \tilde{u}_{\parallel} \mathbf{B} \cdot \nabla \left(\frac{1}{B} \right) - \nabla \tilde{\phi} \cdot \left(\mathbf{B} \times \nabla \left(\frac{1}{B^2} \right) \right) \\
&= \hat{b} \cdot \nabla \tilde{u}_{\parallel} + \tilde{u}_{\parallel} \mathbf{B} \cdot \nabla \left(\frac{1}{B} \right) - \frac{2}{B^3} \nabla \tilde{\phi} \cdot \left(\left(\frac{1}{r} \hat{\zeta} \times \nabla \psi \right) \times \nabla B \right) \\
&= \hat{b} \cdot \nabla \tilde{u}_{\parallel} + \tilde{u}_{\parallel} \mathbf{B} \cdot \nabla \left(\frac{1}{B} \right) + \frac{2\boldsymbol{\kappa} \cdot \nabla \psi}{r^2 B^2} \frac{\partial \tilde{\phi}}{\partial \zeta}
\end{aligned} \tag{B.14}$$

and

$$\tilde{\mathbf{u}} \cdot \nabla \rho = \tilde{u}_{\parallel} \hat{b} \cdot \nabla \rho - \partial_{\psi} \rho \partial_{\zeta} \tilde{\phi} \tag{B.15}$$

in Eq. (B.12), after some algebra, we obtain Eq. (4.55). By similar calculation, linearization of (4.51) gives (4.56).

Linearization of Eq. (4.52) gives

$$\hat{b} \cdot \left(-\tilde{\rho} r \Omega^2 \hat{r} + \rho \partial_t \tilde{\mathbf{u}} + \rho \tilde{\mathbf{u}} \cdot \nabla \mathbf{u} + \rho \mathbf{u} \cdot \nabla \tilde{\mathbf{u}} + \nabla \tilde{p} \right) = 0. \tag{B.16}$$

By using

$$\begin{aligned}
\hat{b} \cdot (\mathbf{u} \cdot \nabla \tilde{\mathbf{u}}) &= \hat{b} \cdot \left(r \Omega \hat{\zeta} \cdot \nabla \left(\tilde{u}_{\parallel} \hat{b} + r \partial_{\psi} \tilde{\phi} \hat{\zeta} - \frac{\partial_{\zeta} \tilde{\phi}}{r B} \hat{\psi} \right) \right) \\
&= \Omega \partial_{\zeta} \tilde{u}_{\parallel} - r \Omega \partial_{\psi} \tilde{\phi} \left(\hat{b} \cdot \hat{r} \right)
\end{aligned} \tag{B.17}$$

and

$$\hat{b} \cdot (\tilde{\mathbf{u}} \cdot \nabla \mathbf{u}) = \hat{b} \cdot \left(\tilde{\mathbf{u}} \cdot \nabla (r \Omega \hat{\zeta}) \right) = r \Omega \tilde{u}_{\zeta} \hat{b} \cdot (\hat{\zeta} \cdot \nabla \hat{\zeta}) = -r \Omega \partial_{\psi} \tilde{\phi} \left(\hat{b} \cdot \hat{r} \right) \tag{B.18}$$

in (B.16), after some algebra, we obtain (4.57).

Finally, linearization of (4.53) gives

$$\begin{aligned}
\left\langle \nabla \cdot \left(\frac{\hat{b}}{B} \times \left(\rho \left(\partial_t \tilde{\mathbf{u}} + \widetilde{\mathbf{u} \cdot \nabla \mathbf{u}} \right) - \tilde{\rho} r \Omega^2 \hat{r} + \nabla \tilde{p} - \frac{1}{4\pi c^2} \widetilde{\nabla \phi \nabla^2 \phi} \right) \right) - \frac{1}{4\pi c^2} \partial_t \nabla^2 \tilde{\phi} \right\rangle \\
= 0. \tag{B.19}
\end{aligned}$$

We tackle it term by term. From (B.13), (B.5), (B.7), (B.8), (B.9), (B.11), and the identity $\mathbf{u} \cdot \nabla \mathbf{u} = \nabla(u^2/2) - \mathbf{u} \times \nabla \times \mathbf{u}$, we can show the following identities:

$$\left\langle \nabla \cdot \left(\frac{\hat{b}}{B} \times \rho \partial_t \tilde{\mathbf{u}} \right) \right\rangle = -\partial_t \left(\frac{\partial}{\partial \psi} \left(\langle \rho r^2 \rangle \frac{\partial \tilde{\phi}}{\partial \psi} \right) + \left\langle \frac{\rho}{r^2 B^2} \right\rangle \frac{\partial^2 \tilde{\phi}}{\partial \zeta^2} \right), \quad (\text{B.20})$$

$$\begin{aligned} \left\langle \nabla \cdot \left(\frac{\rho}{B} \hat{b} \times \left(\widetilde{\mathbf{u} \cdot \nabla \mathbf{u}} \right) \right) \right\rangle &= \left\langle \nabla \cdot \left(\frac{\rho}{B} \hat{b} \times \left(\nabla(\mathbf{u} \cdot \tilde{\mathbf{u}}) - \mathbf{u} \times \nabla \times \tilde{\mathbf{u}} - \tilde{\mathbf{u}} \times \nabla \times \mathbf{u} \right) \right) \right\rangle \\ &= \frac{\partial}{\partial \psi} \left(\left\langle \rho \frac{\partial(r^2 \Omega)}{\partial \psi} \right\rangle \frac{\partial \tilde{\phi}}{\partial \zeta} - \langle \rho r^2 \rangle \Omega \frac{\partial^2 \tilde{\phi}}{\partial \zeta \partial \psi} - \Omega \langle 2\rho r \hat{b} \cdot \hat{r} \tilde{u}_{\parallel} \rangle \right) \\ &\quad - \Omega \frac{\partial}{\partial \zeta} \left(\left\langle \frac{2\rho \hat{b} \cdot \hat{z}}{B} \right\rangle \frac{\partial \tilde{\phi}}{\partial \psi} + \left\langle \frac{\rho}{r^2 B^2} \right\rangle \frac{\partial^2 \tilde{\phi}}{\partial \zeta^2} \right) \\ &= \frac{\partial}{\partial \psi} \left\langle \rho \frac{\partial(r^2 \Omega)}{\partial \psi} \right\rangle \frac{\partial \tilde{\phi}}{\partial \zeta} - \frac{\partial}{\partial \psi} \left(\Omega \langle 2\rho r \hat{b} \cdot \hat{r} \tilde{u}_{\parallel} \rangle \right) \\ &\quad - \Omega \frac{\partial}{\partial \zeta} \left(\frac{\partial}{\partial \psi} \left(\langle \rho r^2 \rangle \frac{\partial \tilde{\phi}}{\partial \psi} \right) + \left\langle \frac{\rho}{r^2 B^2} \right\rangle \frac{\partial^2 \tilde{\phi}}{\partial \zeta^2} \right), \quad (\text{B.21}) \end{aligned}$$

$$\left\langle \nabla \cdot \left(\frac{\tilde{\rho} r \Omega^2 \hat{b} \times \hat{r}}{B} \right) \right\rangle = \left\langle \nabla \cdot \left(\frac{\tilde{\rho} r \Omega^2 (\hat{b} \cdot \hat{z}) \hat{\zeta}}{B} \right) \right\rangle = \left\langle \frac{\Omega^2 \hat{b} \cdot \hat{z}}{B} \frac{\partial \tilde{\rho}}{\partial \zeta} \right\rangle, \quad (\text{B.22})$$

$$\left\langle \nabla \cdot \left(\frac{\hat{b}}{B} \times \nabla \tilde{p} \right) \right\rangle = \left\langle \frac{2\boldsymbol{\kappa} \cdot \nabla \psi}{B^2 r^2} \frac{\partial \tilde{p}}{\partial \zeta} \right\rangle, \quad (\text{B.23})$$

$$\left\langle \nabla \cdot \left(\frac{\hat{b}}{B} \times \nabla \tilde{\phi} \nabla^2 \phi \right) \right\rangle = -\frac{\partial}{\partial \psi} \left\langle B^2 \frac{\partial(r^2 \Omega)}{\partial \psi} \right\rangle \frac{\partial \tilde{\phi}}{\partial \zeta}, \quad (\text{B.24})$$

$$\begin{aligned} \left\langle \nabla \cdot \left(\frac{\hat{b}}{B} \times \nabla \phi \nabla^2 \tilde{\phi} \right) \right\rangle &= \left\langle \nabla \cdot (r \Omega \nabla^2 \tilde{\phi} \hat{\zeta}) \right\rangle = \Omega \partial_{\zeta} \langle \nabla^2 \tilde{\phi} \rangle = \Omega \partial_{\zeta} \langle \nabla \cdot \nabla \tilde{\phi} \rangle \\ &= \Omega \partial_{\zeta} \left(\frac{\partial}{\partial \psi} \left(\langle r^2 B^2 \rangle \frac{\partial \tilde{\phi}}{\partial \zeta} \right) + \left\langle \frac{1}{r^2} \right\rangle \frac{\partial^2 \tilde{\phi}}{\partial \zeta^2} \right), \quad (\text{B.25}) \end{aligned}$$

$$\langle \partial_t \nabla^2 \tilde{\phi} \rangle = \partial_t \langle \nabla \cdot \nabla \tilde{\phi} \rangle = \partial_t \left(\frac{\partial}{\partial \psi} \left(\langle r^2 B^2 \rangle \frac{\partial \tilde{\phi}}{\partial \zeta} \right) + \left\langle \frac{1}{r^2} \right\rangle \frac{\partial^2 \tilde{\phi}}{\partial \zeta^2} \right). \quad (\text{B.26})$$

Using (B.20)-(B.26) in (B.19), after some algebra, we get (4.58).

Appendix C

Local Stability Criterion of Magnetorotational Instability

In this Appendix we briefly derive the local dispersion relation and stability criterion of the magnetorotational instability. We assume incompressibility. The rotating plasma with velocity $\mathbf{u} = r\Omega\hat{\phi}$ is threaded with a constant axial magnetic field $\mathbf{B} = B\hat{z}$, where we use $(\hat{r}, \hat{\phi}, \hat{z})$ to denote three cylindrical coordinate unit vectors. The linearized MHD equations for small perturbations are:

$$\nabla \cdot \tilde{\mathbf{u}} = 0, \quad (\text{C.1})$$

$$\rho\partial_t\tilde{\mathbf{u}} + \rho(\mathbf{u} \cdot \nabla\tilde{\mathbf{u}} + \tilde{\mathbf{u}} \cdot \nabla\mathbf{u}) = -\nabla(\tilde{p} + \mathbf{B} \cdot \tilde{\mathbf{B}}) + \mathbf{B} \cdot \nabla\tilde{\mathbf{B}}, \quad (\text{C.2})$$

$$\partial_t\tilde{\mathbf{B}} = \nabla \times (\mathbf{u} \times \tilde{\mathbf{B}} + \tilde{\mathbf{u}} \times \mathbf{B}), \quad (\text{C.3})$$

$$\nabla \cdot \tilde{\mathbf{B}} = 0. \quad (\text{C.4})$$

We limit our analysis to axisymmetric perturbations. Assuming all perturbed quantities to be proportional to $\exp(ik_r r + ik_z z - i\omega t)$, Eqs. (C.1)–(C.3) become (assuming $1/r \ll k_r$)

$$ik_r\tilde{u}_r + ik_z\tilde{u}_z = 0, \quad (\text{C.5})$$

$$-i\omega\rho\tilde{u}_r - 2\rho\Omega\tilde{u}_\phi = ik_z B\tilde{B}_r - ik_r\tilde{p} - ik_r B\tilde{B}_z, \quad (\text{C.6})$$

$$-i\omega\rho\tilde{u}_\phi + (2\Omega + r\partial_r\Omega)\rho\tilde{u}_r = ik_z B\tilde{B}_\phi, \quad (\text{C.7})$$

$$-i\omega\rho\tilde{u}_z = -ik_z\tilde{p}, \quad (\text{C.8})$$

$$-i\omega\tilde{B}_r = ik_z B\tilde{u}_r, \quad (\text{C.9})$$

$$-i\omega\tilde{B}_\phi = ik_z B\tilde{u}_\phi + r\partial_r\Omega\tilde{B}_r, \quad (\text{C.10})$$

$$-i\omega\tilde{B}_z = ik_z B\tilde{u}_z, \quad (\text{C.11})$$

and Eq. (C.4) is consistent with (C.5), (C.9), and (C.11). The local dispersion relation follows from (C.5)–(C.11):

$$k^2\omega^4 - k_z^2 \left(2k^2V_A^2 + \frac{\partial\Omega^2}{\partial\ln(r)} + 4\Omega^2 \right) \omega^2 + k_z^4V_A^2 \left(k^2V_A^2 + \frac{\partial\Omega^2}{\partial\ln(r)} \right) = 0, \quad (\text{C.12})$$

where $k^2 = k_r^2 + k_z^2$. We can easily prove that ω^2 is real. If $V_A = 0$, then

$$\omega^2 = \frac{k_z^2}{k^2} \left(\frac{\partial\Omega^2}{\partial\ln(r)} + 4\Omega^2 \right) = \frac{k_z^2}{k^2r^3} \frac{\partial(r^4\Omega^2)}{\partial r}, \quad (\text{C.13})$$

which leads to the Rayleigh's stability criterion for unmagnetized fluids:

$$\frac{\partial(r^4\Omega^2)}{\partial r} > 0 \Leftrightarrow \text{stability}. \quad (\text{C.14})$$

If $k_zV_A \neq 0$, then the stability criterion becomes

$$k^2V_A^2 + \frac{\partial\Omega^2}{\partial\ln(r)} > 0 \Leftrightarrow \text{stability}, \quad (\text{C.15})$$

which is the local criterion for magnetorotational instability. An intriguing feature of the magnetorotational instability is that the presence of a magnetic field changes the stability criterion drastically, no matter how weak the magnetic field is. Criterion (C.15) does not approach (C.14) in the limit $V_A \rightarrow 0$. It may be informative to see which of the three MHD modes (the shear Alfvén wave, the slow, and the fast magnetosonic waves) is destabilized by the differential rotation. However, we cannot tell from the incompressible description presented here. In the incompressible limit, the fast magnetosonic wave disappears, and the shear Alfvén wave and the slow magnetosonic wave become degenerate, with $\omega^2 = k_z^2V_A^2$ (this can be seen by letting $\Omega \rightarrow 0$ in Eq. (C.12)). By allowing compressibility to break the degeneracy, one can show that the slow mode is the one to be destabilized. The readers are referred to the review paper of Balbus and Hawley [4] for further discussion along this line.

Appendix D

Local Parker Instability Growth Rate

D.1 A Simple Derivation of the Parker Instability Growth Rate in the Cold Plasma Limit

In this Appendix, we present a simple derivation of the local Parker instability growth rate in the cold plasma limit. Suppose a cold plasma is supported against a constant gravity $\mathbf{g} = -g\hat{x}$ by a magnetic field $\mathbf{B} = B(x)\hat{z}$. The equilibrium satisfies the force balance equation:

$$\frac{d}{dx} \left(\frac{B^2}{2} \right) = -\rho g. \quad (\text{D.1})$$

For small perturbations about the equilibrium, the linearized ideal MHD equations are:

$$\partial_t \tilde{\rho} = -\nabla \cdot (\rho \tilde{\mathbf{u}}), \quad (\text{D.2})$$

$$\rho \partial_t \tilde{\mathbf{u}} = -\nabla(\mathbf{B} \cdot \tilde{\mathbf{B}}) + \mathbf{B} \cdot \nabla \tilde{\mathbf{B}} + \tilde{\mathbf{B}} \cdot \nabla \mathbf{B} + \tilde{\rho} \mathbf{g}, \quad (\text{D.3})$$

$$\partial_t \tilde{\mathbf{B}} = \nabla \times (\tilde{\mathbf{u}} \times \mathbf{B}). \quad (\text{D.4})$$

For simplicity, we only consider 2D perturbations (i.e. $\partial_y = 0$). Since the system has translational symmetry along the z direction, we can assume normal modes of the form $\tilde{\rho}(x) \exp(ik_z z - i\omega t)$, etc. As we did in Sec. 5.3.2, we assume the wavelength in the z direction to be much shorter than the length scale of any fluctuation in the x direction (i.e. $\partial_x \ll k_z$).

Suppose we compress mass along a field line. This causes local density clumping according to Eq. (D.2):

$$\omega \tilde{\rho} \simeq k_z \rho \tilde{u}_z, \quad (\text{D.5})$$

where $\partial_x(\rho \tilde{u}_x)$ is neglected in comparison with $k_z \rho \tilde{u}_z$, since we assume short wavelength in the z direction. As the density clumps, the extra weight causes the magnetic line to bend to balance the extra weight. This balance is Alfvénically quasi-static (i.e. $\omega \ll k_z V_A$) and the corresponding equation is given by the x component of (D.3):

$$ik_z B \tilde{B}_x \simeq \tilde{\rho} g, \quad (\text{D.6})$$

wherein the terms $i\omega \rho \tilde{u}_x$ and $\partial_x(B \tilde{B}_z)$ are neglected in view of the quasi-static and short wavelength assumptions, to be checked self-consistently later. In the presence of magnetic gradients, the field line bending results in constrictions and distensions along the flux tube. This makes matter squirt into the distended parts of the flux tube, according to the z component of (D.3):

$$-i\omega \rho \tilde{u}_z = \partial_x B \tilde{B}_x = -\frac{\rho g}{B} \tilde{B}_x, \quad (\text{D.7})$$

where in the last step Eq. (D.1) is used for $\partial_x B$. The new matter squirted into the distension makes $\tilde{\rho}$ go up even more, thus resulting in instability. The dispersion relation can be solved from Eqs. (D.5)-(D.7) as:

$$\omega^2 \simeq -\frac{g^2}{V_A^2}. \quad (\text{D.8})$$

Notice that if g is replaced by the centrifugal force $r\Omega^2$, the local dispersion relation (5.28) is recovered.

To check the self-consistency of the above-mentioned derivation, we have to verify the three assumptions we have made: $\partial_x(\rho \tilde{u}_x) \ll ik_z \rho \tilde{u}_z$, $\partial_x(B \tilde{B}_y) \ll k_z B \tilde{B}_x$, and $\omega^2 \ll k_z^2 V_A^2$. Now we check them in order. First of all, eliminating \tilde{B}_x in Eq. (D.7), using the x component of Eq. (D.4), yields

$$\tilde{u}_x = -\frac{ig}{k_z V_A^2} \tilde{u}_z, \quad (\text{D.9})$$

where we use the dispersion relation (D.8) for ω^2 . Hence, the assumption $\partial_x(\rho\tilde{u}_x) \ll ik_z\rho\tilde{u}_z$ requires $\partial_x(\rho\tilde{u}_x) \ll (k_z^2\rho V_A^2/g)\tilde{u}_x$, which implies

$$k_x \ll k_z^2 V_A^2 / g. \quad (\text{D.10})$$

This can be satisfied as long as k_z is large enough. To check the second assumption, notice that the constraint $\nabla \cdot \tilde{\mathbf{B}} = 0$ gives the relation between \tilde{B}_x and \tilde{B}_z :

$$\partial_x \tilde{B}_x + ik_z \tilde{B}_z = 0. \quad (\text{D.11})$$

Therefore, we require $\partial_x(B\partial_x\tilde{B}_x) \ll k_z^2 B\tilde{B}_x$, which implies

$$k_x^2 \ll k_z^2. \quad (\text{D.12})$$

Again, this is consistent with the local approximation. Finally, the Alfvénically quasi-static assumption requires [using (D.8)]

$$g \ll k_z V_A^2, \quad (\text{D.13})$$

which can be also satisfied in the short wavelength limit. Notice that conditions (D.12) and (D.13) imply condition (D.10); therefore, only (D.12) and (D.13) are necessary. The self-consistency conditions are satisfied in the short wavelength limit; in that limit, the growth rate is independent of the wavelength. However, the above derivation is good for $k_z a \gg 1$ [$a \sim V_A^2/g$ is the vertical length scale, from Eq.(D.1)], as a result of the quasi-static approximation. If $k_z a \lesssim 1$, the Alfvénic restoring forces become more efficient (or the gravity induced clumping becomes less efficient); this causes the growth rate to drop at long wavelengths. It should also be kept in mind that all the conclusions here are only valid in the cold plasma limit. If the plasma has a nonzero temperature, the pressure will stabilize short wavelength modes. The dependence of the dispersion relation on pressure and wavelengths is the topic of the next appendix (see also Sec. 5.3.4).

D.2 Local Parker Instability Growth Rate — the General Case

In this appendix we briefly outline the derivation of the Parker instability local dispersion relation for a plasma with non-zero temperature. For simplicity we assume $p = \text{const}$ and $\rho = \text{const}$ in the equilibrium. The governing Eqs. for a small perturbation from the equilibrium are still (D.2)-(D.4), except pressure has to be included in (D.3):

$$\rho \partial_t \tilde{\mathbf{u}} = -\nabla(\tilde{p} + \mathbf{B} \cdot \tilde{\mathbf{B}}) + \mathbf{B} \cdot \nabla \tilde{\mathbf{B}} + \tilde{\mathbf{B}} \cdot \nabla \mathbf{B} + \tilde{\rho} \mathbf{g}, \quad (\text{D.14})$$

where $\tilde{p} = C_S^2 \tilde{\rho}$. In the following derivation we only consider perturbations with wavelengths much shorter than the characteristic length scale of the background variation such that the WKB approximation is appropriate. Under this assumption, we can assume $\tilde{\rho} \rightarrow \tilde{\rho} \exp(ik_x x + ik_z z - i\omega t)$ etc. Taking the y component of the curl of Eq. (D.14) yields:

$$\omega \rho (k_x \tilde{u}_z - k_z \tilde{u}_x) = k^2 B \tilde{B}_x + ik_z \tilde{\rho} g, \quad (\text{D.15})$$

where $k^2 = k_x^2 + k_z^2$. In deriving (D.15) we use the constraint $\nabla \cdot \tilde{\mathbf{B}} = 0$ and neglect $\tilde{B}_x \partial_x^2 B$ (which is much smaller than $k^2 B \tilde{B}_x$ by assumption) in the RHS. The z component of (D.14) yields:

$$-i\omega \rho \tilde{u}_z = -ik_z C_S^2 \tilde{\rho} - \frac{\rho g}{B} \tilde{B}_x, \quad (\text{D.16})$$

where we use (D.1) for $\partial_x B$. Next, with the WKB approximation Eq. (D.2) becomes:

$$\omega \tilde{\rho} = \rho (k_x \tilde{u}_x + k_z \tilde{u}_z). \quad (\text{D.17})$$

Finally, the x component of Eq. (D.4) is:

$$-\omega \tilde{B}_x = k_z B \tilde{u}_x. \quad (\text{D.18})$$

Eqs. (D.15)-(D.18) form a closed set of variables \tilde{u}_x , \tilde{u}_z , $\tilde{\rho}$, and \tilde{B}_x . The local dispersion relation can therefore be obtained, after some algebra, as:

$$\omega^4 - k^2 (C_S^2 + V_A^2) \omega^2 + k_z^2 (k^2 V_A^2 C_S^2 - g^2) = 0. \quad (\text{D.19})$$

The two solutions of ω^2 represent the fast and slow magnetosonic modes, respectively, under the effect of the gravity. The fast mode is always stable whereas the slow mode could be destabilized by the gravity; the stability criterion is:

$$k^2 V_A^2 C_S^2 - g^2 > 0. \quad (\text{D.20})$$

The validity of the WKB approximation may be justified if $k_x, k_z \gg (1/B)dB/dx = g/V_A^2$. If we further assume that $C_S \ll V_A$, the dispersion relation for the slow mode can be expressed in a rather simple form:

$$\omega^2 \simeq \frac{k_z^2 (k^2 C_S^2 V_A^2 - g^2)}{k^2 (C_S^2 + V_A^2)}. \quad (\text{D.21})$$

Notice that in the $C_S \rightarrow 0$ and $k_x \ll k_z$ limit, the dispersion relation (D.8) is recovered. As we can see from (D.21), the non-zero pressure of a warm plasma stabilizes short wavelength modes. We can also apply Eq. (D.20) to obtain a rough stability criterion for the Dean flow model. Recall that the Dean flow has a finite radial size a , hence $k > \pi/a$, and gravity is replaced by the centrifugal force $R\Omega^2$; the schematic stability criterion so obtained is:

$$\pi^2 \frac{R^2}{a^2} > M_S^2 M_A^2, \quad (\text{D.22})$$

which is the same as what we obtained at the end of Sec. V. From Eq. (D.21), for a high M_S , high M_A system (i.e. $M_S M_A \gg \pi R/a$), the ‘‘cutoff’’ to unstable modes occurs at $k_z^c a \sim ga/C_S V_A \sim M_S \sqrt{a/R}$, and the maximum growth rate occurs at $k_z^m a \sim \sqrt{k_z^c a}$.

BIBLIOGRAPHY

- [1] G. F. Abdrashitov, A. V. Beloborodov, V. I. Volosov, V. V. Kubarev, Y. S. Popov, and Y. N. Yudin. Hot rotating plasma in the PSP-2 experiment. *Nucl. Fusion*, 31(7):1275–1290, 1991.
- [2] S. A. Balbus and J. F. Hawley. A powerful local shear instability in weakly magnetized disks .1. linear-analysis. *Astrophys. J.*, 376:214–222, 1991.
- [3] S. A. Balbus and J. F. Hawley. Is the Oort α -value a universal growth-rate limit for accretion disk shear instabilities. *Astrophys. J.*, 392:662–666, 1992.
- [4] S. A. Balbus and J. F. Hawley. Instability, turbulence, and enhanced transport in accretion disks. *Rev. Mod. Phys.*, 70:1–53, 1998.
- [5] A. A. Bekhtenev, V. I. Volosov, V. E. Pal’chikov, M. S. Pekker, and Y. N. Yudin. Problems of a thermonuclear reactor with a rotating plasma. *Nucl. Fusion*, 20(5):579–598, 1980.
- [6] E. S. Benilov, V. Naulin, and J. J. Rasmussen. Does a sheared flow stabilize inversely stratified fluid? *Phys. Fluids*, 14:1674–1680, 2002.
- [7] I. B. Bernstein, E. A. Frieman, M. D. Kruskal, and R. M. Kulsrud. An energy principle for hydromagnetic stability problems. *Proc R Soc London Ser A-Math*, 244:17–40, 1958.

- [8] H. Biglari, P. H. Diamond, and P. W. Terry. Influence of sheared poloidal rotation on edge turbulence. *Phys Fluids B-Plasma Phys*, 2:1–4, 1990.
- [9] V. N. Bocharov, S. G. Konstantinov, A. M. Kudryavtsev, O. K. Myskin, V. M. Panasyuk, A. F. Sorokin, and F. A. Tsel'nik. Equilibrium state of a rotating plasma in a mirror system. *Sov. J. Plasma Phys.*, 4(3):271–273, 1978.
- [10] J. P. Boyd. *Chebyshev and Fourier Spectral Methods*. Dover Publications, Inc., 2001.
- [11] S. I. Braginskii. Transport process in a plasma. *Rev. Plasma Physics*, 1:205, 1965.
- [12] B. N. Breizman and F. A. Tsel'nik. MHD stability of a rotating plasma. *Sov. J. Plasma Phys.*, 91(6):666–668, 1983.
- [13] B. N. Breizman and F. A. Tsel'nik. Centrifugal confinement system with particle-beam injection. *Sov. J. Plasma Phys.*, 11(7):451–455, 1985.
- [14] S. N. Brown and K. Stewartson. On the algebraic decay of disturbances in a stratified linear shear-flow. *J. Fluid Mech.*, 100:811–816, 1980.
- [15] F. W. Byron, Jr. and R. W. Fuller. *Mathematics of Classical and Quantum Physics*, volume 1. Addison-Wesley Publishing Company, 1969.
- [16] K. M. Case. Stability of an idealized atmosphere. I. discussion of results. *Phys. Fluids*, 3(2):149–154, 1960.
- [17] K. M. Case. Stability of inviscid plane Couette flow. *Phys. Fluids*, 3(2):143–148, 1960.
- [18] S. Chandrasekhar. The stability of non-dissipative Couette flow in hydromagnetics. *Proc. Natl. Acad. Sci. U. S. A.*, 46:253–257, 1960.

- [19] S. Chandrasekhar. *Hydrodynamic and Hydromagnetic Stability*. Oxford University Press, Oxford, England, 1961.
- [20] G. Chimonas. Algebraic disturbances in stratified shear flows. *J. Fluid Mech.*, 90:1–19, 1979.
- [21] S. DeSouza-Machado, A. B. Hassam, and R. Sina. Stabilization of Z pinch by velocity shear. *Phys. Plasmas*, 7:4632–4643, 2000.
- [22] P. G. Drazin and W. H. Reid. *Hydrodynamic Stability*. Cambridge University Press, 1981.
- [23] R. F. Ellis, A. B. Hassam, S. Messer, and B. R. Osborn. An experiment to test centrifugal confinement for fusion. *Phys. Plasmas*, 8:2057–2065, 2001.
- [24] R. J. Goldston and P. H. Rutherford. *Introduction to Plasma Physics*. Institute of Physics Publishing, Philadelphia, 1995.
- [25] J. Goodman and H. T. Ji. Magnetorotational instability of dissipative Couette flow. *J. Fluid Mech.*, 462:365–382, 2002.
- [26] D. J. Griffiths. *Introduction to Electrodynamics*. Prentice-Hall, Inc., 2nd edition, 1986.
- [27] R. J. Groebner. An emerging understanding of H-mode discharges in tokamaks. *Phys Fluids B-Plasma Phys*, 5:2343–2354, 1993.
- [28] P. N. Guzdar, J. F. Drake, D. McCarthy, A. B. Hassam, and C. S. Liu. Three-dimensional fluid simulations of the nonlinear driftresistive ballooning modes in tokamak edge plasmas. *Phys. Fluids B*, 5:3712–3727, 1993.
- [29] J. Hartmann. Det kgl. danske videnskabernes selskab. *Mathematisk-fysiske Meddelelser*, XV(6):1, 1937.

- [30] A. B. Hassam. Nonlinear stabilization of the Rayleigh-Taylor instability by external velocity shear. *Phys Fluids B-Plasma Phys*, 4:485–487, 1992.
- [31] A. B. Hassam. Steady state centrifugally confined plasmas for fusion. *Comments Plasma Phys. Controlled Fusion*, 18:263, 1997.
- [32] A. B. Hassam. Stability of magnetohydrodynamic Dean flow as applied to centrifugally confined plasmas. *Phys. Plasmas*, 6:3738–3743, 1999.
- [33] A. B. Hassam. Velocity shear stabilization of interchange modes in elongated plasma configurations. *Phys. Plasmas*, 6:3772–3777, 1999.
- [34] A. B. Hassam, R. M. Kulsrud, R. J. Goldston, H. Ji, and M. Yamada. Steady state thermoelectric field-reversed configurations. *Phys. Rev. Lett.*, 83(15):2969–2972, 1999.
- [35] J. F. Hawley and S. A. Balbus. A powerful local shear instability in weakly magnetized disks .2. nonlinear evolution. *Astrophys. J.*, 376:223–233, 1991.
- [36] Y.-M. Huang and A. B. Hassam. Velocity shear stabilization of centrifugally confined plasma. *Phys. Rev. Lett.*, 87:235002, 2001.
- [37] Y.-M. Huang and A. B. Hassam. Magnetorotational and parker instabilities in magnetized plasma Dean flow as applied to centrifugally confined plasmas. *Phys. Plasmas*, 10:204–213, 2003.
- [38] Y.-M. Huang and A. B. Hassam. Resistive magnetohydrodynamic equilibrium and stability of a rotating plasma with particle sources. *Phys. Plasmas*, 11(8):3738–3747, 2004.
- [39] J. D. Jackson. *Classical Electrodynamics*. John Wiley & Sons, Inc., 2nd edition, 1975.

- [40] H. T. Ji, J. Goodman, and A. Kageyama. Magnetorotational instability in a rotating liquid metal annulus. *Mon. Not. Roy. Astron. Soc.*, 325:L1–L5, 2001.
- [41] A. Kent. Instability of laminar flow of a perfect magnetofluid. *Phys. Fluids*, 9:1286–1289, 1966.
- [42] A. Kent. Stability of laminar magnetofluid flow along a parallel magnetic field. *J. Plasma Phys.*, 2:543–556, 1968.
- [43] J. Kim, S. S. Hong, D. Ryu, and T. W. Jones. Three-dimensional evolution of the Parker instability under a uniform gravity. *Astrophys. J.*, 506:L139–L142, 1998.
- [44] J. Kim, D. S. Ryu, and T. W. Jones. Three-dimensional simulations of the Parker instability in a uniformly rotating disk. *Astrophys. J.*, 557:464–474, 2001.
- [45] W. T. Kim and E. C. Ostriker. Magnetohydrodynamic instabilities in shearing, rotating, stratified winds and disks. *Astrophys. J. Lett.*, 540:372–403, 2000.
- [46] E. Knobloch. On the stability of stratified plane Couette-flow. *Geophys. Astrophys. Fluid Dyn.*, 29:105–116, 1984.
- [47] M. D. Kruskal and R. M. Kulsrud. Equilibrium of a magnetically confined plasma in a toroid. *Phys. Fluids*, 1:265–274, 1958.
- [48] B. Lehnert. Rotating plasmas. *Nucl. Fusion*, 11:485–&, 1971.
- [49] R. Matsumoto, T. Tajima, K. Shibata, and M. Kaisig. Three-dimensional magnetohydrodynamics of the emerging magnetic flux in the solar atmosphere. *Astrophys. J.*, 414:357–371, 1993.
- [50] M. Mitchner and C. H. Kruger, Jr. *Partially Ionized Gases*. John Wiley & Sons, 1973.

- [51] T. C. Mouschovias. Static equilibria of interstellar gas in presence of magnetic and gravitational-fields - large-scale condensations. *Astrophys. J.*, 192:37–49, 1974.
- [52] U. Müller and L. Bühler. *Magnetofluidynamics in Channels and Containers*. Springer-Verlag Berlin Heidelberg, 2001.
- [53] K. Noguchi, V. I. Pariev, S. A. Colgate, H. F. Beckley, and J. Nordhaus. Magnetorotational instability in liquid metal Couette flow. *Astrophys. J.*, 575:1151–1162, 2002.
- [54] E. N. Parker. Dynamical state of interstellar gas and field. *Astrophys. J.*, 145:811–833, 1966.
- [55] V. P. Pastukhov. Collisional losses of electrons from an adiabatic trap in a plasma with a positive potential. *Nucl. Fusion*, 14:3–6, 1974.
- [56] V. P. Pastukhov. Classical longitudinal plasma losses from open adiabatic traps. *Rev. Plasma Physics*, 13:203–259, 1987.
- [57] W. H. Press, S. A. Teukolsky, W. T. Vetterling, and B. P. Flannery. *Numerical Recipes in C++: The Art of Scientific Computing*. Cambridge University Press, 2nd edition, 2002.
- [58] A. M. Rey and A. B. Hassam. Convection in an asymmetrically sourced Z pinch. *Phys. Plasmas*, 8:5151–5157, 2001.
- [59] L. Spitzer, Jr. *Physics of Fully Ionized Gases*. John Wiley & Sons, Inc., 2nd edition, 1962.
- [60] H. R. Strauss. Nonlinear, three-dimensional magnetohydrodynamics of noncircular tokamaks. *Phys. Fluids*, 19(1):134–140, 1976.

- [61] G. W. Sutton and A. Sherman. *Engineering Magnetohydrodynamics*. McGraw-Hill, 1965.
- [62] P. W. Terry. Suppression of turbulence and transport by sheared flow. *Rev. Mod. Phys.*, 72(1):109–165, 2000.
- [63] L. N. Trefethen. *Spectral Methods in Matlab*. SIAM Philadelphia, 2000.
- [64] L. N. Trefethen, A. E. Trefethen, S. C. Reddy, and T. A. Driscoll. Hydrodynamic stability without eigenvalues. *Science*, 261:578–584, 1993.
- [65] E. P. Velikhov. Stability of an ideally conducting liquid flowing between cylinders rotating in a magnetic field. *Sov Phys-Jetp Engl Trans*, 9:995–998, 1959.
- [66] V. I. Volosov and M. S. Pekker. Longitudinal plasma confinement in a centrifugal trap. *Nucl. Fusion*, 21(10):1275–1281, 1981.